Magnetic Field Study for a New Generation High Resolution Mass Separator

by

Marco Marchetto

Laurea in Fisica, Università Degli Studi di Padova, 2003

A THESIS SUBMITTED IN PARTIAL FULFILLMENT OF
THE REQUIREMENTS FOR THE DEGREE OF

DOCTOR OF PHILOSOPHY

in

The Faculty of Graduate and Postdoctoral Studies

(Physics)

THE UNIVERSITY OF BRITISH COLUMBIA

(Vancouver)

December 2017

Abstract

The work presented in this thesis is part of the design of the high resolution mass separator for the ARIEL facility under construction at TRIUMF, located in the UBC campus. This new facility, together with the existing ISAC facility, will produce rare isotope beams for nuclear physics experiments and nuclear medicine.

The delivery of such beams requires a stage of separation after production to select the isotope of interest. The required separation is expressed in terms of resolving power defined as the inverse of the relative mass difference between two isotopes that need to be separated. The higher the mass the greater the resolving power required. The challenge is the separation of two isobars rather than two isotopes that by definition require a much lower resolving power. A resolving power of twenty thousand is the minimum required to achieve isobaric separation up to the uranium mass.

The state of the art for existing heavy ion mass separators is a resolving power in the order of ten thousand for a transmitted emittance of less than three micrometers. The more typical long term operational value is well below ten thousand for larger emittances. The main goal of this project is to develop a mass separator that maintains an operational resolving power of twenty thousand.

Different aspects influence the performance of the mass separator; the two main ones are the optics design and the field quality of the magnetic dipole(s) that provides the core functionality of the mass separator.

In this thesis we worked from the hypothesis that minimizing the magnetic field integral variation with respect to the design mass resolution is equivalent to minimizing the aberration of the optical system.

During this work we investigated how certain geometric parameters in-

Abstract

fluence the field quality, as for example the dependency of the field flatness on the magnet pole gap. We also developed a new technique to control the mesh in the finite element analysis to facilitate particle tracking calculations.

Beyond demonstrating our hypothesis, we ultimately produced a final magnet design where the field integral variation is less than one part in one hundred thousand.

Lay Summary

Rare isotopes are the new frontier for fundamental studies in nuclear physics but also for medical application for the diagnosis and treatment of tumors. Rare isotopes have been produced at TRIUMF since the late nineties. A new facility, ARIEL, will increase such production three fold. One critical step in the delivery of such rare isotopes is the separation and selection. The production includes isobars with mass difference smaller than one part in many thousands. In order to select a desired isotope produced in the new facility, a new generation mass separator system has been developed capable of discriminating a mass difference of one part in twenty thousand. The thesis work consists in the design of a high performance magnetic dipole that is the core component of the separator system. One key achievement is a magnetic field variation of few parts per million.

Preface

The work done in this thesis is a main contribution to the High Resolution Separator (HRS) project funded by Canada Foundation for Innovation (CFI). The project is divided into two components: beam dynamics study and magnet design.

Dr. James Maloney was in charge to the beam dynamics calculation while I was in charge of the magnet design, the main hardware components of the HRS system. The work presented in this thesis is related only to the magnet design.

A paper was published on the beam dynamics study: "New design studies for TRIUMF's ARIEL High Resolution Separator"[1]. My contribution to this paper as co-author is related to magnetic field study and the magnet design details.

A paper dedicated to the design of the magnet will be written based on chapters 2 to 5 of this thesis. I will be the main author with Prof. Richard Baartman and Dr. Maloney as co-author.

Chapter 1 contains results from work I did at Canada's national laboratory for particle and nuclear physics and accelerator-based science (TRIUMF) in the field of Rare Isotope Beams (RIBs) since 2004. In particular on the issue of separation and delivery of high mass beams as reported in "Progress and plans for high mass beam delivery at TRIUMF"[2] (first author paper and invited oral at the 2012 Heavy Ion Accelerator Technology Conference). On the subject I contributed in developing a technique for mass separation in flight using existing TRIUMF infrastructure as reported in "In flight ion separation using a Linac chain"[3] (first author paper and invited oral at the 2012 Linear Accelerator Conference). I have been working for many years on TRIUMF post-accelerators, that are designed to deliver RIBs; I contributed

in many aspects including beam dynamics as reported in "Beam Dynamics Studies on the ISAC-II Superconducting Linac"[4] (first author paper) and hardware upgrade.

In general I have been working in the field of particle accelerators since my university study in Italy, including my physics "laurea" thesis: "Study of a high-current 176 MHz RFQ as a deuteron injector for the SPES project"[5].

All these preliminary works have been instrumental to properly develop the work of this thesis.

Table of Contents

Table of Contents

List of Tables

List of Figures

List of Acronyms

ANL Argonne National Laboratory (laboratory)

ARIEL Advanced Rare IsotopE Laboratory (facility)

CANREB CANadian Rare isotope facility with Electron Beam (project)

CARIBU CAlifornium Rare Ion Breeder Upgrade (project)

CERN Conseil Europeen pour la Recherche Nucleaire (laboratory)

CFI Canada Foundation for Innovation (funding)

CGS Centimetre-Gram-Second system of units (units)

CW Continuous Wave (operational mode)

DTL Drift Tube Linac (accelerator)

ECR Electron Cyclotron Resonance (ion source)

ECRIS Electron Cyclotron Resonance Ion Source (ion source)

FEBIAD Forced Electron Beam Induced Arc Discharge (ion source)

FRIB Facility for Rare Isotope Beam (facility)

HRS High Resolution Separator (separator)

ISAC Isotope Separation and ACceleration (facility)

ISOL Isotope Separation On-Line (production method)

ISOLDE Isotope Separation On Line DEvice (facility)

List of Acronyms

LIS Laser Ion Source (ion source)

MSU Mitchigan State University

RIB Radioactive Ion Beam (sometimes also Rare Isotope Beam)

RF Radio Frequency (operational mode)

RFQ Radio Frequency Quadrupole (accelerator)

TRIUMF Canada's national laboratory for particle and nuclear physics and accelerator-based science (laboratory[1])

SC SuperConducting (operational mode)

SI International System of units (units)

UBC University of British Columbia

---

[1]historically TRIUMF stands for TRI University Meson Facility.

List of Units

This section includes definition of units that are used in the particle accelerator community and not part of the International System of units (SI)[6].

e-A electrical-Ampere: this current definition takes into account the charge state of the ions that contributes to the electrical current. A submultiple of this unit is the e-nA (10^{-9} e-A).

p-A particle-Ampere: this current definition doesn't consider the charge state of the ions that contributes to the electrical current. Alternatively it can be seen as the current in electrical Amperes divided by the charge state of the ion; complications may arise though when the electrical current is composed of ions with different charge states. This unit is preferred to the electrical Ampere definition by the experimenters since it's straightforward to infer the number of particles per second by simply dividing by the elementary charge ($1.6 \cdot 10^{-19}$ C).

pps particle per second: this is the preferred beam intensity unit for an experiment since they are looking at the number of reactions.

Acknowledgements

I am always reluctant to make a list of people to thank because inevitably someone is left out, nevertheless I will try and risk to upset a few.

First and foremost I have to thank Prof. Lia Merminga, my former TRIUMF accelerator division head and one of my committee members. It is not an overstatement saying that my PhD would have not happen if it wasn't for Lia. Lia gave me this once in a life time opportunity to pursue this degree while maintaining my responsibilities and the possibility of advancing my career at TRIUMF. I own her more than I will ever be able to give back.

Another big thank you goes to Prof. Richard Baartman, research co-supervisor and TRIUMF supervisor. I always think of Rick as a colleague rather than the boss.

Thank you to Prof. Andrea Damascelli, research supervisor, and Prof. Vesna Sossi, committee member, for their trust in me.

Thanks to Dr. James Maloney for the collaboration in designing the high resolution separator; I hope our effort will not be in vain.

Thanks to P.Eng. George S. Clark, former TRIUMF magnets engineer, for his critical approach based on his decades long experience during our discussions about the magnet design.

Thanks to Buckley Systems for making my design a realty.

Thanks to my colleague Dr. Thomas Planche for his feedback and to my former supervisor Prof. Robert Laxdal for supporting my PhD.

Thanks to the CANREB management to assign me the task of designing the HRS magnet.

Dedication

I dedicate this work to Francesca, Orlando, Oliver, Arthur and Tristan. It was always a fine balance working and writing the thesis while home was invaded by four little Huns. Luckily Francesca was there.

Chapter 1

Introduction

This thesis is a development in the field of particle accelerator physics that studies the behavior of an ion beam as an ensemble of charged particles transported from a starting point (source) to a final destination (experiment) through electric and magnetic fields contained in a system of beam transport lines.

Beams are typically classified in two main categories depending if they are composed of light or heavy particles. Light particles like electrons or positrons are practically always relativistic in accelerator systems. Heavier particles like protons or ions require more accelerating voltage to become relativistic. For the purpose of this thesis we will consider only non-relativistic heavy ions; as a reference ^{4}He (on the light side of the heavy ions) becomes relativistic (β greater than 0.5) around 600 MeV. This is considered a very high energy for heavy ions.

Ion sources produce particles with an initial energy that ranges from tens to hundreds of keV. For heavy ions with energies above a few hundreds of keV, the unit used is the electronvolts per unified atomic mass unit, in symbol eV/u; in our previous example the ^{4}He energy would be circa $150\,\mathrm{keV/u}$. Sometimes the latter are also quoted in eV/A, in this document we will use the former unit.

The initial energy can be increased, or decreased, using accelerating

structures along the beam lines. Two metal plates at different electrostatic potential separated by a gap constitute a simple accelerating structure. More complex accelerating structures are called particle accelerators that utilize either electrostatic or electromagnetic (radio-frequency or RF) fields in order to provide acceleration. Particles are guided along a defined beam trajectory by means of electrostatic or magnetostatic fields.

A Radioactive Ion Beam (RIB) is an ensemble of radioactive charged particles. These beams are used in astrophysics, nuclear and atomic physics, material and medical science experiments. The required final energies for these experiments range from a few eV for atomic physics to hundreds of MeV for the nuclear physics.

The radioactive elements that compose the beam have half-lives that can range typically from ms to hours. Due to their short half-lives, they are not readily available in nature and therefore they have to be produced in a laboratory. In general the production techniques produce multiple radioactive species. A radioactive ion beam composed of different elements is sometimes referred as a cocktail beam. Moreover the ionization stage can introduce stable ions into the cocktail.

Mass selection techniques are necessary to isolate the isotope of interest. Nevertheless it is not always possible to completely separate two different isotopes. In general only one element in these cocktails is required for the experiment while the other components are considered contaminants. The contaminants can render an experiment unfeasible.

1.1 Radioactive ion beam production methods

There are two commonly used methods for RIB production [7] that we are going to introduce in the following sections. Both production methods have in common an accelerator called the driver for the primary beam, a production target and a separation facility for the selection of the secondary radioactive beam; post-acceleration is an option to boost the energy of the selected beam.

1.1.1   In-flight method

The first production method is called the in-flight or fragmentation method. In this case the primary beam is a heavy ion, like ^{238}U, that is accelerated at high energies in the order of hundreds of MeV/u. The driver is complex and fairly expensive accelerator system like in the case of the Mitchigan State University (MSU) new Facility for Rare Isotope Beam (FRIB)[8]. A relatively thin target intercepts the primary beam to produce the secondary radioactive particles. The secondary beam retains 90% or more of the primary beam energy[9]. Right downstream of the target the secondary beam goes through the selection stage consisting of a fairly complex mass separator system. Once selected the beam is sent to the experimental station. Since the secondary beam is already produced at high energy, post-acceleration is usually not considered in this case.

The production process for the in-flight method occurs via projectile fragmentation, nucleon transfer, fission and Coulomb excitation[9]. Different target materials can be used such as beryllium, tungsten, nickel or tantalum as a few examples; the radioactive ion beam production is material dependent. The thicker the target the higher the probability of multiple scattering, and therefore higher production, but also the higher the energy straggling leading to higher energy spread. This means a reduced beam quality.

Beam quality is quantified in terms of transverse and longitudinal emittances. The emittance is related to the area the beam occupies in phase space (see chapter 2): position versus divergence in the transverse case and energy versus time in the longitudinal case. This area is included inside an ellipse of area $\pi\epsilon$ where ϵ is the emittance of the beam [10] [11]. The transverse emittance unit is mm·mrad or μm while the longitudinal emittance is expressed in keV/u·ns (or alternatively keV/u·deg). The lower the emittance the higher the beam quality.

The typical transverse emittance for the in-flight method is on the order of 10^2 μm [12][13][14]; this is considered a large or poor emittance compared to what an ion source can typically produce. Also the typical energy spread

is large, in the order of few per cent: that translates into a few MeV/u.

The in-flight on the other hand is a fast production method that allows the delivery of isotopes with very short half-lives, few μs, where the limitation is due to selection rather than production process. The in-flight method produces also high intensity beams up to a few 10^{10} pps or 10^{-9} pA.

1.1.2 ISOL method

The second production method is the Isotope Separation On-Line (ISOL). In this case the driver accelerates light projectiles toward a thick target. These light projectiles are usually protons, but studies have been conducted to develop deuteron or tritium[5] drivers for ISOL production. The projectiles interact with the target heavy nuclei producing neutral radioactive isotopes via spallation, fragmentation or induced fission[15]. The target material may vary from silicon to uranium; the material choice is based on the production requirements[16] .

The neutral atoms produced in the target migrate into an ion source via diffusion and effusion processes[15]. Here they are ionized and extracted at source potential up to a few tens of kV. Different types of sources can be used[17], the simplest being the surface source[18]; the latter works efficiently for elements with low ionization potential (less than 6 eV) by transferring energy through a heated surface. Other sources include: plasma ion sources like the Forced Electron Beam Induced Arc Discharge (FEBIAD)[19], Electron Cyclotron Resonance (ECR)[20] and Laser Ion Source (LIS)[21].

The transverse emittance produced is an order of magnitude smaller (higher quality) with respect to the in-flight method. An upper limit expected from a FEBIAD ion source is about 20μm, while values of less than 10μm are typical of a surface ion source. The energy spread out of the source is in the order of few eV. This energy spread translates into less than one part in ten thousand, at least two orders of magnitude lower than the energy spread produced with the alternative method.

The radioactive ions extracted from the source are separated using a dipole magnet (mass separator) and selected to be transported to the down-

stream experimental stations. Thanks to the production process the beam can be delivered at energies as low as 10 keV. In order to deliver energies higher than the extraction voltage, the beam must be post-accelerated. In this case energies up to 20 MeV/u have been reached at the isotope separation and acceleration facility (see section 1.2).

The ISOL method is limited though in terms of half-lives and beam intensity with respect to the in-flight. The relatively slow extraction process limits the possibility of extracting isotopes with few ms while beam intensities are in the order of few 10^3 pps or 10^{-16} pA.

1.2 The ISAC facility at TRIUMF

Rare Isotope Beams (RIBs) are produced at TRIUMF in the Isotope Separation and ACceleration (ISAC) facility using the ISOL method. A plan
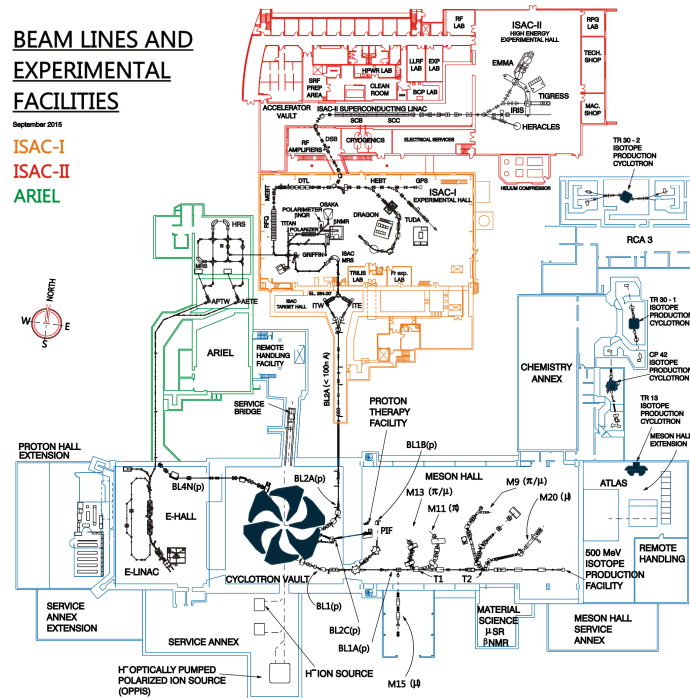
Figure 1.1: The TRIUMF site. Highlighted are the ISAC-I (red), ISAC-II (orange) and ARIEL (green) facilities.

view of the TRIUMF facilities is represented in figure 1.1.

The ISAC facility counts fifteen experimental stations [22] distributed in three experimental areas characterized by different energy ranges: low, medium and high. The overview of the ISAC facility is represented in figure 1.2 where the three experimental areas are highlighted. Presently only a single RIB is available and can be sent to one of the fifteen stations at a time.
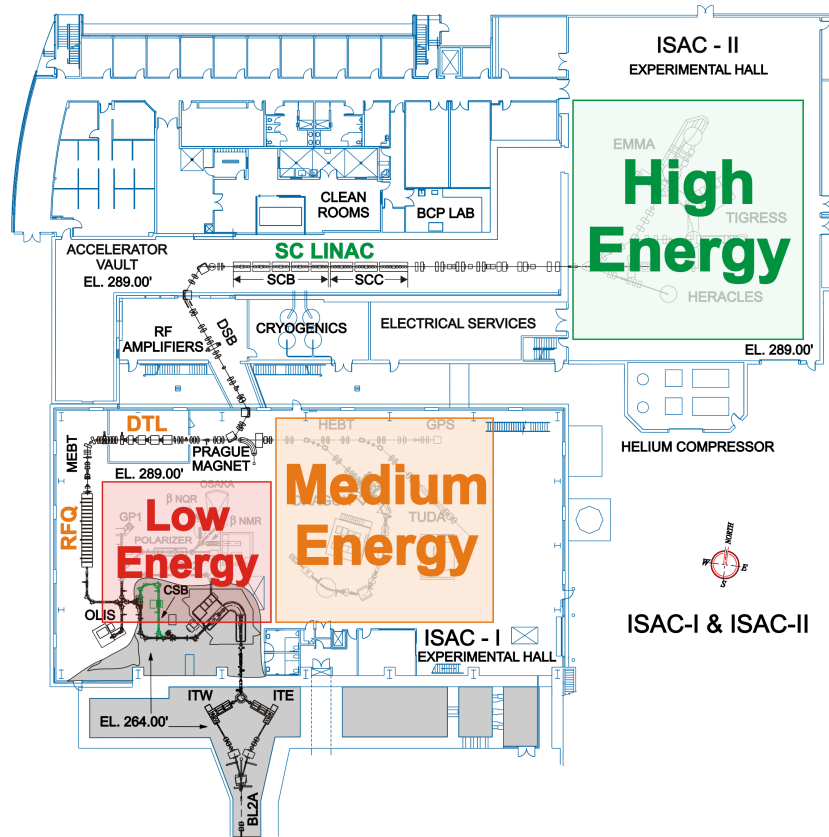
Figure 1.2: ISAC facility at TRIUMF. The three experimental areas (low, medium and high) are highlighted. The grey shaded area is located two stories underground while the remaining is at ground level.

The future Advanced Rare IsotopE Laboratory (ARIEL) facility (high-lighted green in figure 1.1) is going to increment the RIB production to three ion beams that can be sent simultaneously to three different experimental

stations. The object of this thesis, the High Resolution Separator (HRS) system magnetic dipole, is going to be part of the ARIEL facility.

The main components of the ISAC facility are briefly described in the following sections.

1.2.1 Driver

The TRIUMF cyclotron is the driver that accelerates H^- ions up to an intensity of $300\,\mu A$ to a maximum energy of $500\,\text{MeV}$ [23][24]. A layout of the cyclotron is represented in figure 1.3. The H^- ions move in a counterclockwise spiral trajectory inside the cyclotron from the center outwards.
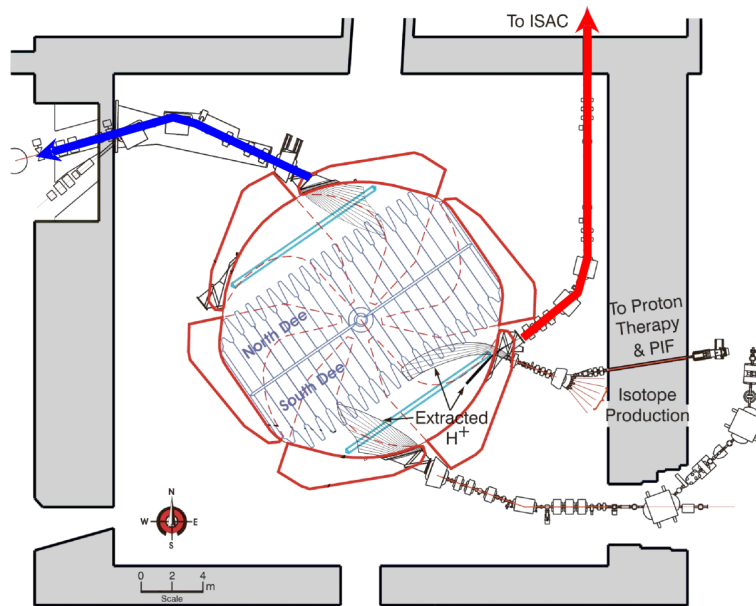
Figure 1.3: TRIUMF H^- cyclotron. Multiple beams can be extracted simultaneously at different energies. Proton beams are extracted at energies up to $500\,\text{MeV}$ and up to $100\,\mu A$ for RIB production in ISAC (red line) and in ARIEL (blue line - future).

In order to extract protons, the H^- ions are intercepted with a carbon foil resulting in the stripping of the electrons; the protons then turn clockwise exiting the cyclotron at specific locations. Since the foil can intercept the

H^- ions at different radial positions inside the cyclotron, protons can be extracted at different energies. Moreover multiple foils can intercept the beam leading to multiple simultaneous extractions. Presently three out of four existing extraction ports are in operation, one of which is dedicated to ISAC (red arrow figure 1.3) for radioactive beam production.

At ISAC the protons are delivered at $500\,\text{MeV}$ up to $100\,\mu\text{A}$ of current. This corresponds to a beam power of up to $50\,\text{kW}$ that allows, for example, the production of the most intense ^{11}Li beam in the world; a production yield of $2.2 \cdot 10^4$ pps has been measured [25] for this beam.

The production capability is going to be expanded by refurbishing the non-operational port and installing a new extraction beam line (blue arrow in figure 1.3) giving two simultaneous proton beams for RIB production [26]. This new beam line, together with a current intensity upgrade [27], is necessary to support the future ARIEL facility.

1.2.2 Target station and mass separator

The proton beam can be directed to two independent target stations [28], west and east, as represented in figure 1.4. Only one station can receive beam at any given time.

Each target station is composed of five modules. The entrance module houses the diagnostic and protect monitors for the proton beam. The target module contains the target and the ion source that produces singly charged ionized species. Target materials include silicon carbide, tantalum and uranium carbide. Two target configurations are available: low and high power respectively for proton beam powers up to $20\,\text{kW}$ and $50\,\text{kW}$. The target module is routinely removed to change both target and ion source. The beam dump module is located downstream of the target module along the direction of the proton beam. The remaining two modules are the extraction ones oriented perpendicular to the proton beam direction; they house the optics elements to transport the beam downstream to the pre-separator.

The two target stations have a pre-separator in common located inside the target hall (see red object in figure 1.4); this is a dipole magnet capable
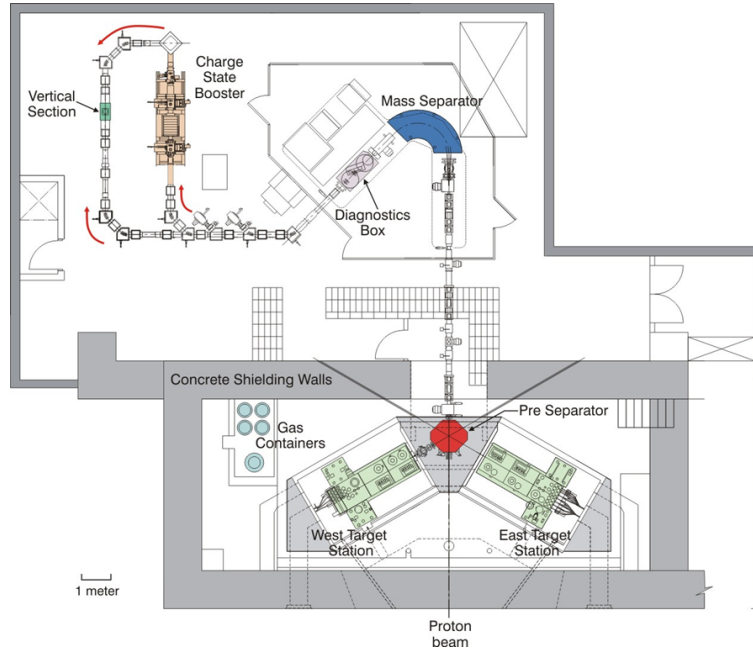
Figure 1.4: ISAC target stations and following separation stages.

of bending the beam from either of two different directions (east and west) to a common (north) beam line leading to the main mass separator. The pre-separator is designed to achieve just isotopic separation in order to contain most of the produced radioactivity inside the shielded target hall. The pre-separator has a low resolving power $(m/\Delta m)$, in the order of few hundred.

An isobaric separation is performed downstream by a second dipole magnet, the mass separator [28], typically operating at a resolving power of a few thousands. This device is installed on a 60 kV biased platform to enhance beam purity in particular from cross contamination [29] generated by residual gas collisions. It is possible in fact that even slow but massive ionized molecules arrive at the mass separator entrance with the same momentum of the radioactive ions to be selected; the platform bias is going to change the momentum such that only the radioactive ions bend around the correct trajectory.

After selection it is possible to boost the single charge state of the ra-

dioactive ions by diverting them through an Electron Cyclotron Resonance Ion Source (ECRIS) [30] [31]. This source known as a charge breeder allows for the post acceleration of masses greater than 30 [2] by reducing the mass to charge ratio to a value compatible with the first stage of post acceleration (see section 1.2.3).

1.2.3   Post accelerators

The selected radioactive ion beams can be delivered to three experimental areas as represented in figure 1.2: a low energy area where the ions are accelerated at source potential (up to $60\,\mathrm{kV}$), a medium energy area ($\beta = 1.8\% \to 6\%$) or a high energy area ($\beta = 6\% \to 18\%$) where the ions are post accelerated with linacs [32] (see figure 1.5) .

The first stage of acceleration uses an Radio Frequency Quadrupole (RFQ) as injector [33]; this is a linear accelerator that can accelerate and focus the beam transversely at the same time. The RFQ accelerator concept, developed in 1969 by Kapchinskii and Teplyakov [34], consists of the idea that by modulating longitudinally the electrodes of an electrostatic quadrupole in a sinusoidal like profile, a longitudinal accelerating component of the electric field is created. A quadrupole is a transverse focusing optical element with four electrodes arranged $90\,$degree apart in a clover leaf like configuration; two electrodes facing each other have the same polarity, opposite to the other two. A quadrupole[2] has the property that while it focuses a beam in one transverse direction (e.g. horizontal), it defocuses in the other (e.g. vertical); in order to have an overall focusing transport system, it is necessary to arrange at least two quadrupoles longitudinally, separated by an opportune distance, with alternate polarity. In the RFQ case, where the base structure is a single long quadrupole, the alternate focusing is achieved by feeding the electrodes with a Radio Frequency (RF) electric field so the beam sees alternating focusing as it travels along the structure. This makes the longitudinal component alternate as well, being accelerating half of the period and decelerating the other half. This implies

---

[2]Quadrupoles can be either electrostatic or magnetic; they both generate a transverse (electric or magnetic) field to focus (or defocus) the beam.
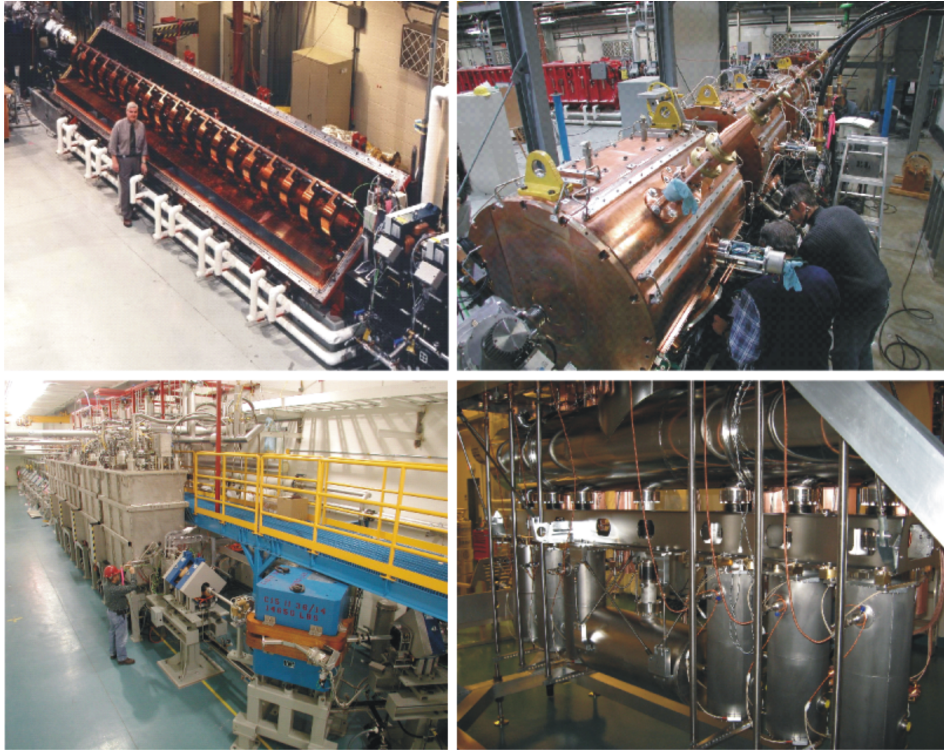
Figure 1.5: ISAC linear accelerators: Radio Frequency Quadrupole (RFQ) (top left), Drift Tube Linac (DTL) (top right), superconducting linac SCB (bottom left, crymodules) and SCC (bottom right, cold mass) sections.

that the ions, in order to be accelerated, have to be bunched in time within one accelerating period, called the RF accelerating bucket. In an RFQ the modulation of the electrodes is usually done gradually so a continuous (in time) beam can be injected while the output beam is bunched. The output velocity, and hence output energy per mass unit of an RFQ is fixed and it depends on the modulation geometry of the electrodes.

The ISAC RFQ (figure 1.5 top-left) boosts the beam energy from $2\,\mathrm{keV/u}$ to $150\,\mathrm{keV/u}$. It can accelerate mass to charge ratio (A/Q) in the range from 3 to 30. It is a room temperature machine operating in Continuous Wave (CW) mode at $35.36\,\mathrm{MHz}$ with an eight meter long resonant structure composed of nineteen split rings supporting the modulated electrodes. The

ISAC RFQ doesn't have a typical bunching section; the beam is pre-bunched at injection by a three harmonic electric buncher, the fundamental harmonic is 11.78 MHz. Because the bunching is performed on a continuous beam, the bunched beam at the entrance of the RFQ presents extended longitudinal distribution, with about 20% falling outside the accelerating bucket; this portion of beam exits with incorrect energy and it is stopped into a fixed collimator downstream of the RFQ [35]. This configuration produces a high quality longitudinal emittance after the RFQ calculated to be 0.22 keV/u·ns.

The following acceleration is accomplished by means of a Drift Tube Linac (DTL). A DTL is composed of a series of hollow tubes separated by gaps. The tubes carry an RF voltage; at any given time two adjacent tubes have opposite voltage that create a longitudinal electric field. As for the RFQ, this electric field is accelerating half of the period and decelerating the other half. Because of the tube voltage configuration, two adjacent gaps have opposite field. A particle crossing the first gap with an accelerating field is going to drift through the following hollow tube (hence the name of the accelerator) while the field in the second gap changes from decelerating to accelerating. A particle synchronized with the RF is going to see just accelerating field in all the gaps it crosses.

In order to increase the acceleration efficiency the ISAC DTL [36] (top-right in figure 1.5) accelerates higher charge state and therefore lower mass to charge ratio. The maximum A/Q is 7 so for mass to charge ratio greater than this value, the charge state must be increased. The ion charge state is increased by means of stripping through an $18\,\mu$m ($4\,\mu$g/cm^2) thin carbon foil downstream of the RFQ. Typically the most populated charge state is selected using a magnetic dipole as long as the mass to charge ratio is within the design limits of the DTL. The efficiency of the stripping foil depends on the mass of the stripped ions, ranging between 30% to 50%. Figure 1.6 shows the charge state distribution of ^{16}O downstream of the RFQ after stripping; the percentages in the graph indicate the relative abundance of particles in a charge state with respect to the total number of particles before stripping. Also, the width of each peak is not related to the charge state (that is integer) but to the fact that the beam has a certain transverse
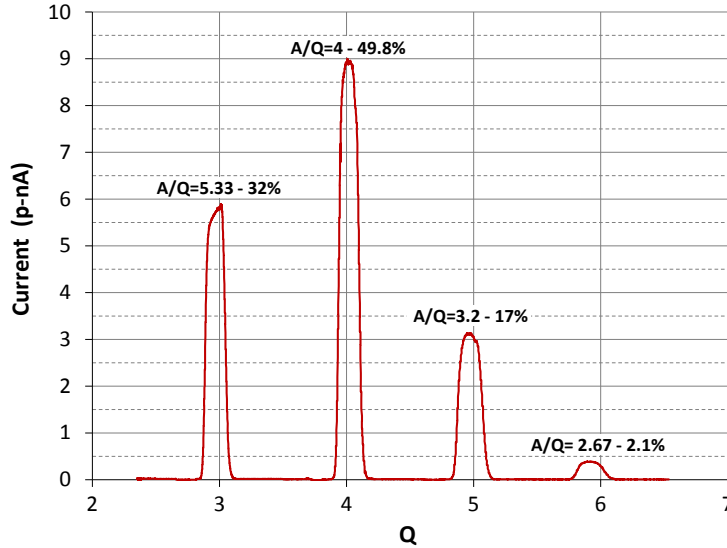
Figure 1.6: Charge state distribution of ^{16}O downstream of the RFQ after stripping with a $18\,\mu$m carbon foil.

distribution (as we are going to explain in chapter 2). When the field of the magnetic dipole is set to the correct value for a desired charge state, the distribution peaks.

The DTL is a variable energy machine covering the entire range of energies between $150\,$keV/u and $1.8\,$MeV/u. It is also a separated function (accelerating and bunching) machine composed of five accelerating cavities and three energy bunchers located between the first four cavities as represented in figure 1.7.

This layout maintains good beam quality at every energy; this translates in a typical energy spread of less than $0.4\,\%$ and a time spread at the experiment in the order of a few nanoseconds. The resonance frequency of the cavities and bunchers is $106.08\,$MHz; they operate at room temperature in CW mode. Transverse focus through the linac is provided by magnetic quadrupole triplets between cavities. The transmission through the linac is greater than 95%. The DTL delivers beam to the medium energy area but it is also used as injector for the ISAC-II SuperConducting (SC) linac.
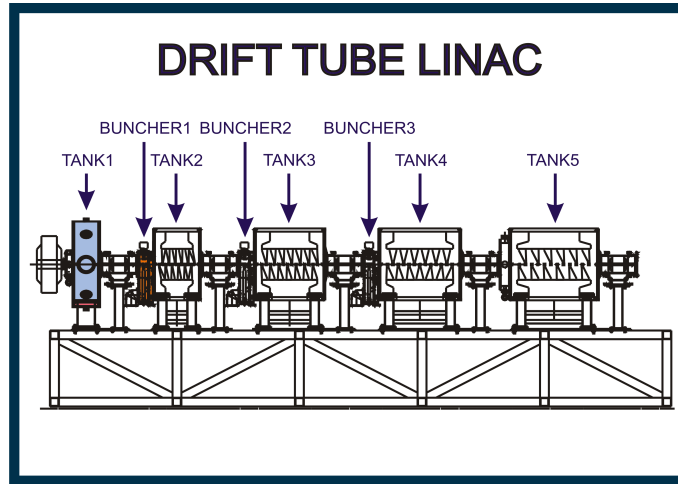
Figure 1.7: ISAC Drift Tube Linac (DTL)

The SC linac [4][37] is the final stage of acceleration before delivering the beam to the high energy area. It is composed of eight cryomodules.
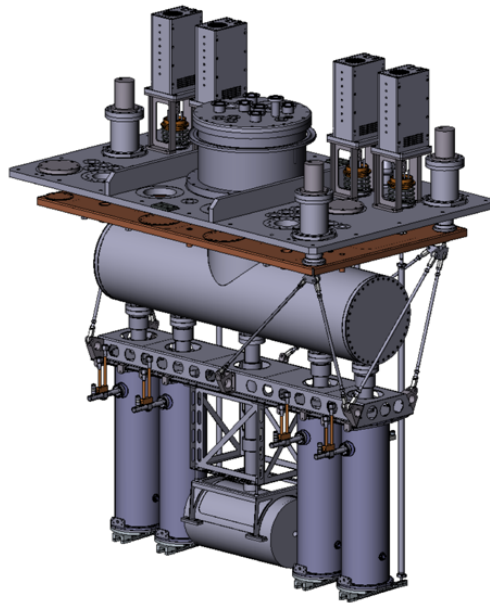
Figure 1.8: ISAC-II SuperConducting (SC) linac: SCB section cold mass.

14

Each of the first five cryomodules (identified as SCB, see figure 1.2) houses a cold mass consisting of four superconducting RF cavities and one superconducting magnetic solenoid in the central position between cavity two and three as illustrated in figure 1.8. A solenoid, similarly to a quadrupole, is a transverse focusing optical element but with a longitudinal magnetic field.

The last three cryomodules (identified as SCC) have cold masses with six (first two cryomodules) and eight (last cryomodule) cavities. Each of them has a superconducting solenoid in the central position as well.

The superconducting cavities are bulk niobium quarter wave resonators operating at 4 K. Each cavity has two accelerating gaps separated by a drift tube. The SCB and SCC cavities, represented in figure 1.9, resonate respectively at a frequency of 106.08 MHz and 141.36 MHz. The ISAC SC linac is capable of accelerating the beam to energy up to 20 MeV/u.

SCB low β (5.7%)   SCB medium β (7.1%)   SCC high β (11%)
  106.08 MHz   106.08 MHz   141.44 MHz
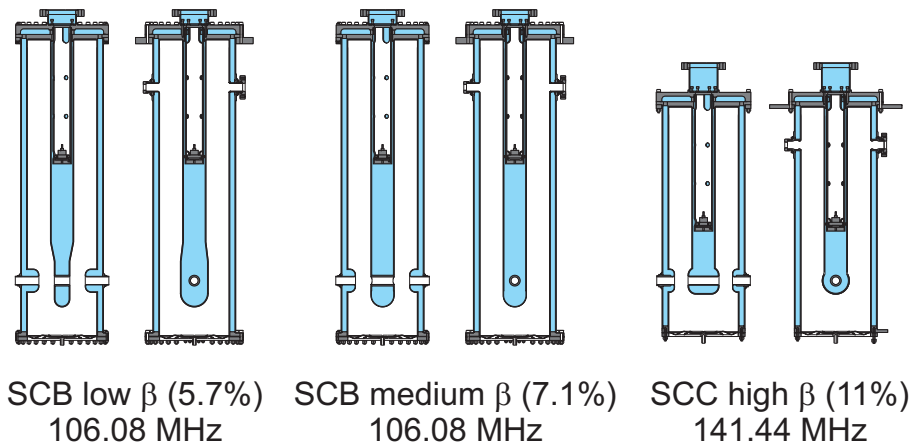
Figure 1.9: ISAC-II SC linac quarter wave resonators.

1.3 Challenges of ISOL production and delivery

Radioactive ion beam production is challenging from several points of view. From a technology point of view, the production chain is composed of many systems (driver, target, separator, charge breeder and post accelerators) that have to operate reliably at the same time. The target itself operates at circa

$2000\,^\circ$C; multiple experiments are expected to run on a single target for a period of four to five weeks. A single experiment may run for a two week period when beam is expected to be delivered uninterrupted. Moreover yield production typically peaks at the beginning of the target life cycle and then degrades, in some cases significantly.

From a production point of view, the ISOL method yields low intensity; as an example, the production yield for ^{11}Li is typically in the $10^4\,\mathrm{s}^{-1}$ range. The number of significant events an experiment can collect are directly proportional to the amount of beam on target. Some experiments may also be constrained by an intensity threshold below which they cannot run. It becomes then critical to minimize the amount of beam loss during transport from the source to the experiment. This is true in particular at the selection stage where a trade-off between resolution and transmission happens.

A second limiting factor for an RIB experiment is the presence of contaminants defined as any other isotope different from the requested. It is expected that the heavier the isotope (stable or radioactive) to be delivered the greater the amount of contamination.

A further complication at ISAC arises when the ECRIS is used to increase the charge state of masses greater than 30. This type of breeder produces a background of stable species by ionizing residual gasses, vacuum chamber materials and immediate surroundings. The background intensities are orders of magnitude higher than the radioactive species, making the identification and selection of the desired RIB isotope extremely challenging. This issue has been partially addressed by using the linac chain to filter RIB beams from the stable background [3].

The first stage of selection occurs by exploiting the time of flight separation between the pre-buncher and the RFQ. Since all the radioactive isotopes are extracted at a fixed voltage, the velocity of any given isotope depends on its mass. This implies that different masses cover the distance between the pre-buncher and the RFQ with different times of flight. Once the desired mass is synchronized with the RF, any other mass that falls off the RFQ acceptance, $\sim 6\,\mathrm{ns}$, is lost during acceleration. Measurements show that it is possible to achieve a longitudinal selection with a resolving power
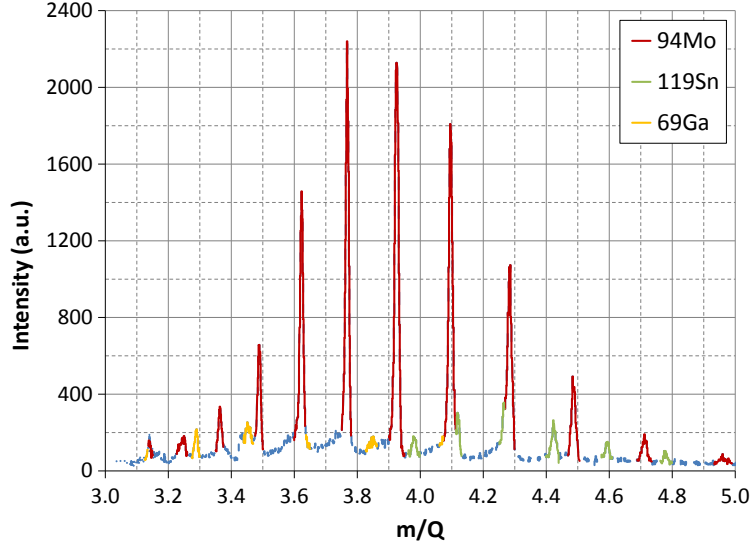
Figure 1.10: Charge state distributions of three isotopes identified as: ^{69}Ga, ^{94}Mo, ^{119}Sn.

of circa 1000.

A second stage of selection is achieved by sending the beam through a carbon stripping foil placed downstream of the DTL. This produces a variety of charge states that further enable particle identification and selection after an m/Q magnet scan is performed. The goal is to shift the m/Q of the contaminant outside the acceptance of the downstream SC linac that is tuned to the m/Q of the RIB. Various foil thicknesses can be selected, the standard is $195\,\mu$m $(44\,\mu$g/cm$^2)$ thick in order to reach charge state equilibrium.

An example of such scans is represented in figure 1.10. In this case the desired radioactive beam is ^{94}Rb^{15+} $(m/Q = 6.262)$ from the charge breeder. A cocktail beam of ^{94}Rb^{15+} plus three main contaminants survives the first stage of selection: ^{69}Ga^{11+} $(m/Q = 6.266)$, ^{94}Mo^{15+} $(m/Q = 6.260)$ and ^{119}Sn^{19+} $(m/Q = 6.258)$.

By selecting $m/Q = 4.268$, mass 94, charge 22, two contaminants, ^{69}Ga and ^{119}Sn, can be removed from the cocktail using a downstream bending

section with a calculated resolving power (this time in terms of mass to charge ratio, $(m/Q)/\Delta(m/Q)$) of circa 320.

The two remaining isotopes ^{94}Rb^{22+} and ^{94}Mo^{22+} ($m/\Delta m = 4405$) can not be separated, but their ratio can be optimized by a proper selection of the charge state out of the stripping foil. As shown in figure 1.11, the stripping efficiency ratios between ^{94}Rb and ^{94}Mo at charge state 23+ and 22+ are respectively 2.5 and 4.5. The charge state choice is in fact a compromise between purity and efficiency of the RIB.

Clear evidence of filtration is seen at the $\Delta E - E$ gas ionization chamber (Bragg detector) installed upstream of the experimental station. Figure 1.12 shows the result of applying the second stage of selection. The cocktail has been filtered and optimized to deliver ^{94}Rb^{22+} radioactive beam, and yet the final distribution is still dominated by the ^{94}Mo^{22+} contaminant due to its higher yield.

Even though nuclides like ^{107}Ag, ^{113}In or ^{132}Xe are theoretically cut out by the pre-buncher and RFQ filtration, it is still possible that these ions have
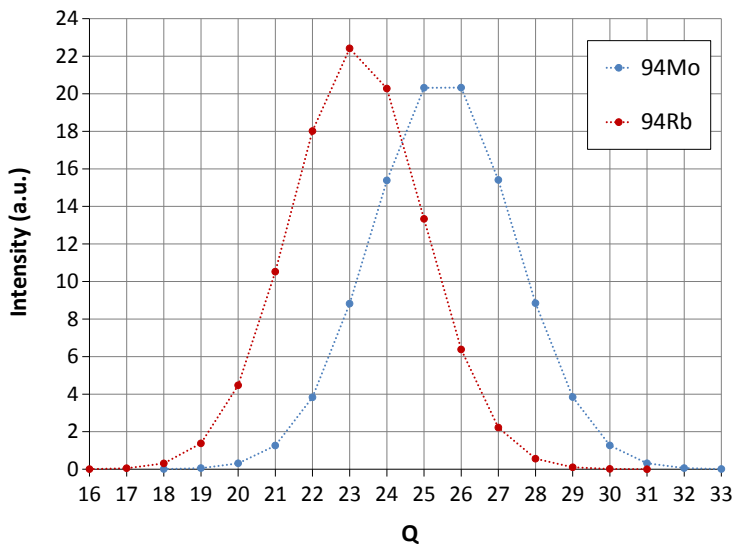
Figure 1.11: Theoretical charge state distribution of ^{94}Rb and ^{94}Mo. The two isobars are separated by a relative mass difference of $\Delta m/m = 1/4405$.

Figure 1.12: Effect of the carbon foil filtration as measured at the Bragg detector: the left picture correspond to the unfiltered cocktail beam from the DTL.

extended longitudinal distribution tails that are eventually accelerated.

In most of the cases the contaminants to RIB ratio can be improved in favor of radioactive species but the contaminants can not be completely suppressed. Also the necessary purification of the beam from contaminants has the side effect of losing part of the produced RIB.

1.4   The quest for resolving power

In general, the heavier the isotope the higher the resolving power needed to produce a pure beam. Figure 1.13 shows the minimum and maximum resolving power needed to achieve isobaric[3] separation as a function of the isotope mass number. The graph is produced considering all the known masses[4] and calculating the resolving power necessary to separate any two isotopes for a given mass number. As an example for A=12 we have Li, Be, B, C, N, and O; there are fifteen possible combinations of two isobars at a

---

[3]Isotopic and Isotonic separation only required a maximum resolving power of 300

[4]AME2012 available at http://www.nndc.bnl.gov/masses/

Figure 1.13: Resolving power range required to separate isobaric isotopes for any given mass.

time. In this case the minimum resolving power is 229 while the maximum is 2820. If the former was the resolving power of the mass separator, then only one out of fifteen occurrences could be resolved. If the latter was the resolving power of the mass separator then all fifteen occurrences are resolvable.

What is then the resolving power required to separate masses up to ^{238}U? It is clear from figure 1.13 that it is unrealistic to think of a mass separator that can resolve all cases. For this it would be necessary to have a resolving power in the 10^7 range. The state of the art is the high resolution mass separator of the CAlifornium Rare Ion Breeder Upgrade (CARIBU)[38] project at Argonne National Laboratory (ANL) where they routinely operate with resolving power of around ten thousand. But a more typical value for this type of mass separator is less than five thousand. A good compromise, and

yet a challenging goal, is to design a mass separator with a resolving power of twenty thousands.

In order to understand what can be separated by such system, we need to look at the relative amount of occurrences that can be resolved as a function of mass for different cases of resolving power, as represented in figure 1.14.

The resolving power of three hundred corresponds to the performance of the ISAC pre-separator, which is meant to resolve only isotopes; it is clearly inadequate to resolve isobars with mass number greater than 20. The three thousand resolving power corresponds to the operational performance of the ISAC mass separator. In this case the available resolving power can separate most of the occurrences ($> 75\%$) for light masses ($A < 30$) but it is a limiting factor ($< 20\%$) for heavy ions ($A > 100$).

An available resolving power of twenty thousand would be enough to re-
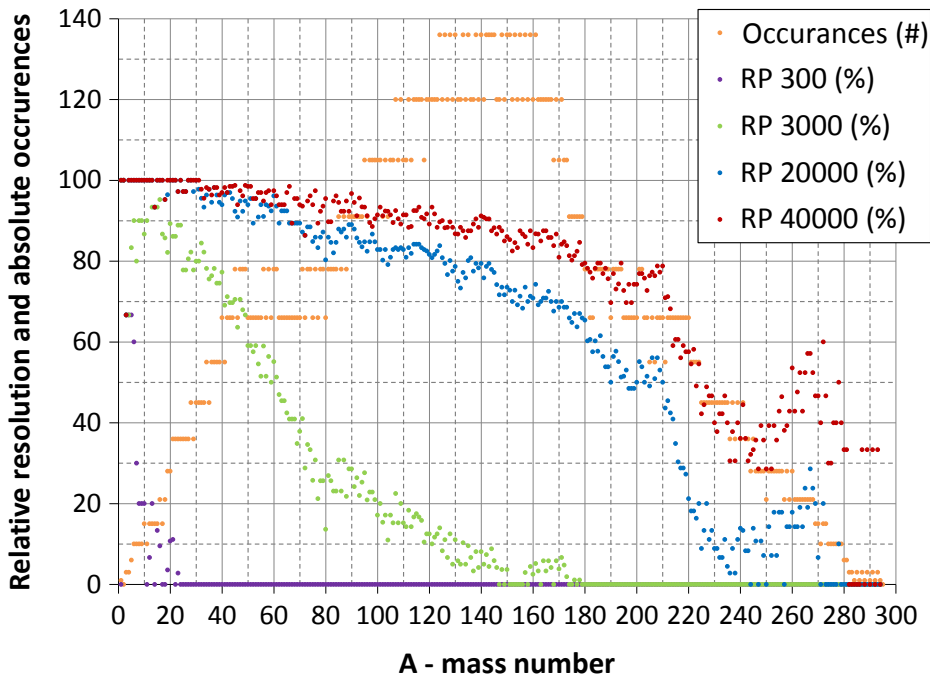
Figure 1.14: Occurrences resolved for a given resolving power as a function of the isotope mass number.

solve more than 50% of the occurrences for masses up to $A = 210$. Increasing the resolving power to forty thousand will yield a higher percentage ($> 70\%$ for $A \leq 210$) but the cost would be at least a factor of four higher since the resolving power is, in first approximation, proportional to the bending radius of the separator dipole magnet, and the surface goes with the square of the radius.

1.5 The physics case of ^{132}Sn

In order to validate the choice of twenty thousand resolving power we consider the physics case of ^{132}Sn. Figure1.15 shows the isobar of mass 132, including tin (red mark), as a function of the neutron number.

The ^{132}Sn isotope falls in the typical range of operation foreseen for the High Resolution Separator (HRS), that is around mass 150.
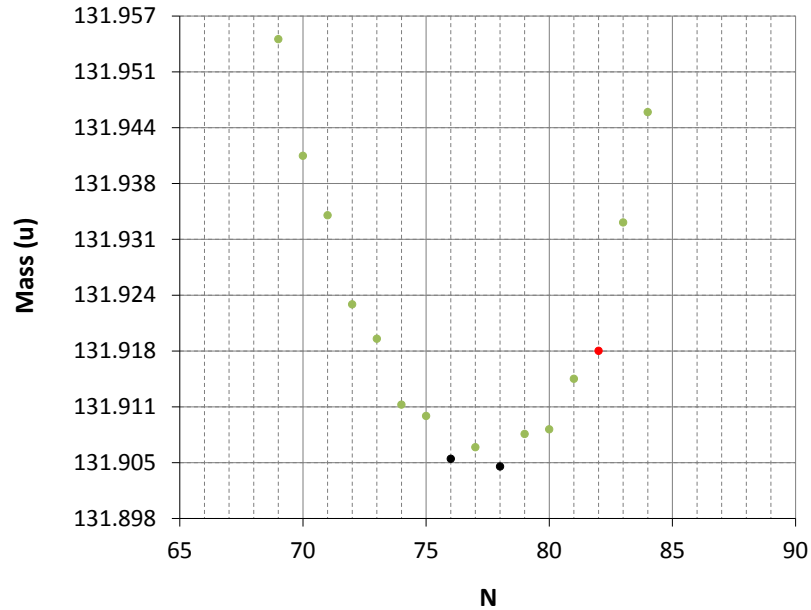
Figure 1.15: Mass 132 isobars as a function of the neutron number: black mark correspond to the stable nuclei, red mark correspond to ^{132}Sn. Each division in the vertical scale corresponds to a resolving power of 20000.

The nucleus of ^{132}Sn is particularly important for nuclear structure, as well as for r-process nucleosynthesis because of its doubly magic ($Z = 50$, $N = 82$) nature[5]. Direct measurements of the binding energy of ^{132}Sn [39] revealed its particularly enhanced stability. Reaction measurements involving ^{132}Sn and the the neighboring ^{133}Sn [40] have brought complementary information on single-particle states confirming the doubly magic nature. It is interesting to point out that the mass measurements required using molecular sideband beams at mass 166 (^{132}Sn+^{34}S) because of insufficient resolving power at mass 132. But the use of molecular post-accelerated beams is not desirable since it is difficult to control where the molecules break up. Therefore a pure ^{132}Sn beam at mass 132 is more desirable to further the study of this key nuclide at future facilities (such as ARIEL).

Figure1.16 shows the resolving power necessary to separate ^{132}Sn from
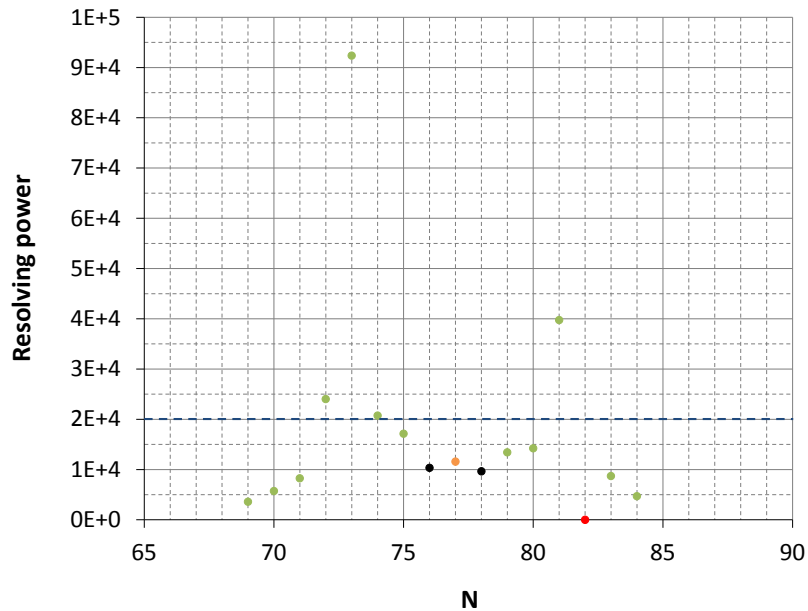
Figure 1.16: Resolving power necessary to separate ^{132}Sn from its isobars. Highlighted are: ^{132}Sn (red mark), ^{132}Cs (orange mark), 20000 resolving power (dashed blue line).

---

[5]Private communication with Dr. David Lunney.

its isobars (the resolving power for tin is intentionally set to zero to indicate no need for separation). While some of these isobars may not be produced (depending on the type of source), it is expected that ^{132}Cs will be produced in great quantity.

Based on the resolving powers represented in figure1.16, a twenty thousand resolving power is adequate to separate the ^{132}Sn beam from 80% of its isobars.

At TRIUMF an experimental proposal[6] to study one and two neutron transfer reactions with neutron-rich Sn beams $132 - 136$ is in the queue since 2008 waiting for the HRS capable of delivering a pure beam. The science goals[7] for this experiment are to investigate neutron orbitals beyond the $N = 82$ shell closure in the r-process nucleosynthesis region.

Presently there is no facility worldwide capable of delivering such a beam, therefore the HRS of the new ARIEL facility makes possible type of investigation for the first time worldwide.

---

[6]Letter of Intent LOI-S1187 evaluated high priority by TRIUMF Experiment Evaluation Committee (EEC).
[7]Private communication with Prof. Ritu Kanungo.

Chapter 2

Magnetic Dipole Mass Separator

The principle of mass separation is based on the fact that particles with different masses have different trajectories when crossing a magnetic field.

A particle with charge q traveling through a magnetic field $\vec{B}$ with velocity $\vec{v}$ experiences the Lorentz force $\vec{F}$ perpendicular to both the velocity and the magnetic field. In a Cartesian coordinate system (x, y, z), the Lorentz force components are:

$$
\begin{pmatrix} F_x \\ F_y \\ F_z \end{pmatrix} = \begin{pmatrix} qv_y B_z - qv_z B_y \\ qv_z B_x - qv_x B_z \\ qv_x B_y - qv_y B_x \end{pmatrix}
\tag{2.1}
$$

If we assume for example that $\vec{v} = (v_x, 0, 0)$ and $\vec{B} = (0, 0, B_z)$, then the particle is going to perform a circular motion in the (x, y) plane with a bending radius of ρ. The bending radius is related to the mass m of the particle according to the following:

$$
B\rho = \frac{m\, v}{q}
\tag{2.2}
$$

where $B = B_z$ and $v = v_x$ in our example. The product $B\rho$ is referred to as the magnetic rigidity of the particle.

When particles are extracted with the same charge state at a fixed voltage V from a production target, like for the ISOL targets in ISAC (see section 1.2.2), the velocity v of the particles depends on the mass m:

$$v = \sqrt{\frac{2\,q\,V}{m}} \tag{2.3}$$

Combining equation 2.2 and 2.3 to eliminate v gives:

$$\rho = \frac{1}{B}\sqrt{\frac{2\,V}{q}\,m} \tag{2.4}$$

Particles with different masses travel inside the magnetic field with different radii and, as stated at the beginning of this chapter, this is the principle on which mass separation is based. If these particles enter the magnetic field at the same location and direction, as sketched in figure 2.1, they exit the field with a transverse separation δ equal to:

$$\delta = D\,\frac{dm}{m} \tag{2.5}$$

where D is called the dispersion of the magnetic dipole and $\frac{m}{dm}$ is the definition of resolving power.
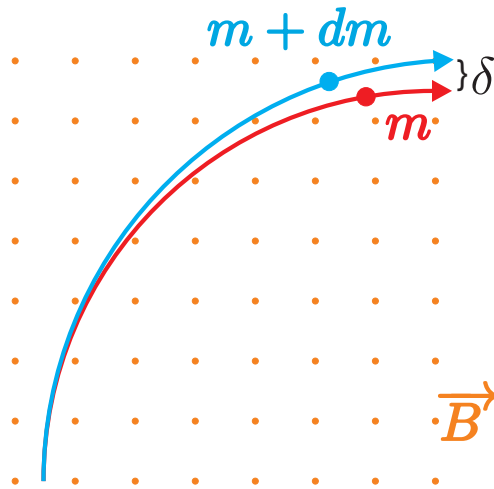
Figure 2.1: Artistic representation of particle trajectories (blue and red) inside a magnetic field (orange).

A magnetic dipole is a mechanical construction that produces a magnetic field as represented in figure 2.1. The general construction has two steel magnetic poles facing each other with opposite polarity separated by an air gap known as the pole gap. The steel is used to increase the field in the gap thanks to its high magnetic permeability. The poles are surrounded by current loops (coils) that generate the magnetic field. Particles travel within the pole gap and experience a field perpendicular to their velocity.

The dispersion is directly proportional to the radius of curvature of the trajectory:

$$D = \rho \left(1 - \cos \theta \right) \tag{2.6}$$

where θ is the bending angle. Notice that for a 90 degree dipole the dispersion of the magnet is equal to the radius of curvature.

Equation 2.5 shows that for a desired resolution and a known dispersion, the maximum transverse size of the beam is δ if we want to separate mass m from mass $m + dm$.

A real beam is an ensemble of particles whose distribution can be represented in the transverse (or longitudinal) phase space as artistically illustrated in figure 2.2. A reference particle is defined within a beam: this is an ideal particle, not necessarily real, that has the momentum which a transport system is designed for. Similarly we define the reference trajectory as the path followed by the reference particle in a transport system.

A characteristic quantity of the beam is the emittance; when there are no dissipative forces and no particles are lost or created, then Liouville's theorem states that the emittance of the beam is conserved[8].

In the first order (linear) approximation, the emittance is conveniently described in phase space by an ellipse (see Appendix A) as represented in figure 2.2.

---

[8]see chapter 9 section 1 of [10], or chapter 5 section 3 of [11]
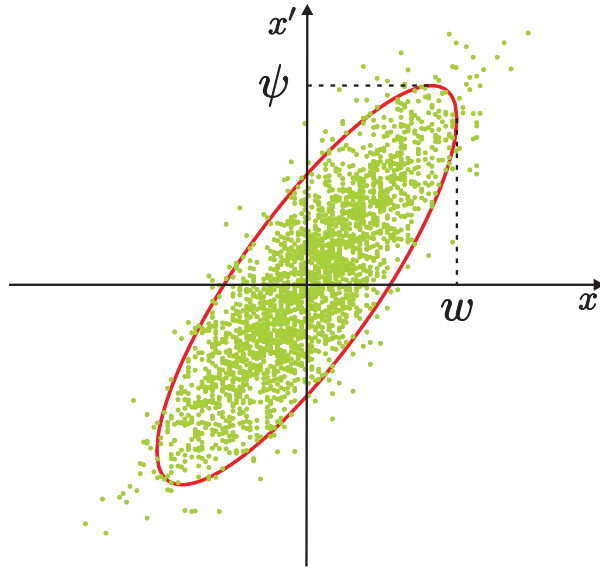
Figure 2.2: Artistic representation of particle distribution in the transverse phase space: w and φ are respectively the half width and the divergence of the beam.

In this case the emittance is defined as:

$$\varepsilon = \frac{A}{\pi} \tag{2.7}$$

where A is the area of the ellipse.

The beam is locally a minimum size if the ellipse is upright, in which case $\varepsilon = w\varphi$. The separator optics is tuned to create an upright ellipse at a beam-defining slit. Because the emittance is conserved, the smaller the beam width w the larger the angle ψ and vice versa.

The amount of particles inside an emittance ellipse depends on the particle distribution in phase space. A Gaussian distribution can be considered for beam dynamics calculations even though a real beam is not Gaussian since it doesn't extend to infinity. If the particle distribution is assumed to be Gaussian in both x and x' then circa 86% of the particles will be contained within 2σ (of the Gaussian distribution) in both axes (see Ap-

pendix B). Conventionally the emittance used to quantify a beam is the one containing 90% of the particles regardless of the distribution.

The separator resolving power is strictly related to the emittance of the beam. In order to have separation it has to be that:

$$2w \leq D \frac{dm}{m} \tag{2.8}$$

as illustrated in figure 2.3.

For an upright ellipse, where $\varepsilon = w\varphi$, equation 2.8 can be written as:

$$\frac{m}{dm} \leq \frac{D\psi}{2\,\varepsilon} \tag{2.9}$$

The resolving power is inversely proportional to the emittance.

More important, for an upright ellipse, the divergence of the beam is known given the emittance and the maximum beam size, defined by the resolution and the dispersion (see equation 2.8). The divergence determines the size of the beam inside the dipole and therefore a lower limit for the size of the magnet. As we are going to see in section 2.3, the beam drifts for a certain distance before entering the magnetic dipole; the optics design is such that the drift is proportional to the radius of curvature ρ. The product of the drift length times the beam divergence gives the width of the beam at the entrance of the dipole. We have that $\rho\psi = \rho \frac{\varepsilon}{w} = 2\frac{\rho}{D}\varepsilon\frac{m}{dm}$, so the width of the beam inside the magnetic dipole (in the pole gap) is proportional to the product of the emittance and the resolving power $(\varepsilon \frac{m}{dm})$. This width defines the area occupied by the beam, referred in jargon as the good field region (see section 2.2), inside the magnet.

The selection process of a particular mass is achieved by intercepting the beam exiting the separator with a mechanical slit; such beam includes the mass to be selected as well as all the other masses to be removed. An example of such process is artistically represented in figure 2.3 with the ideal case of three beams, having the same intensity, being selected by a transverse slit $2w$ wide centered on the origin. The selection result is that
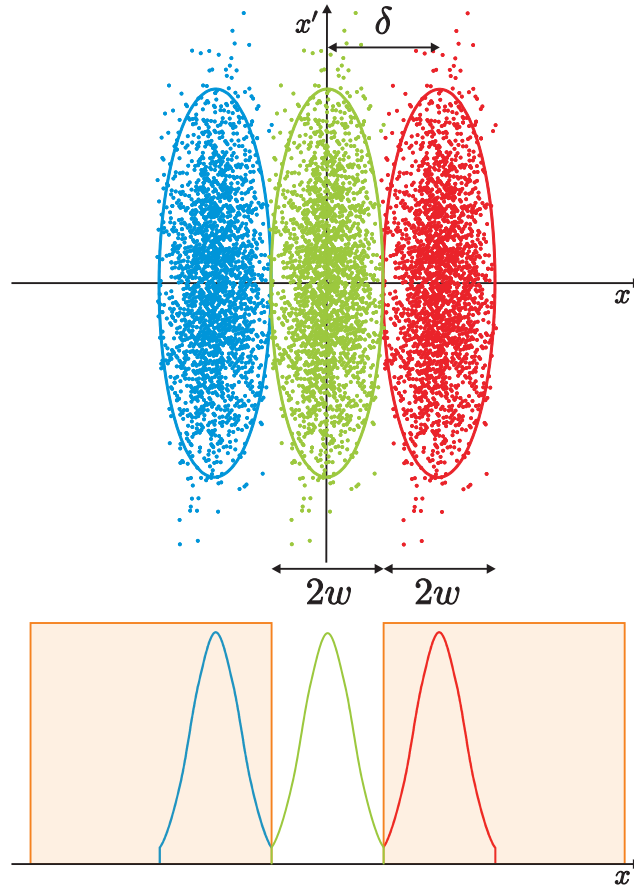
Figure 2.3: Artistic representation of beam separation ($\delta = D \frac{dm}{m}$) and selection: ideal case of three beams, having the same intensity, being selected by a transverse slit (transparent orange squares) $2w$ wide. The Gaussian tails, that overlap with the selected beam (green), are truncated at the entrance of the separator system with a slit.

only the central (green) beam is transported beyond the selection location. In order to avoid contamination the Gaussian tails, that overlap with the selected beam, are truncated at the entrance of the separator system with a slit.

The size of the beam $2w$ going through the selection slit is changed according to the emittance while maintaining the same beam divergence through the separator.

According to equation 2.9, the larger the dispersion D the higher the resolving power achievable. From equation 2.6 we know that the dispersion is proportional to the radius of curvature ρ of the trajectory; in our case the radius of curvature can be at most $1200\,\text{mm}$ based on space constraints. If our separator was a simple 90 degree ($D = \rho$) then, based on equation 2.8, the beam width $2w$ would be $60\,\mu\text{m}$ for a 20000 resolving power.

Equation 2.9 shows also that the smaller the emittance the higher the resolving power. Notice also that if the beam emittance was zero, and so the width of the beam, then the resolving power would be infinite. A reasonably small emittance to consider is $3\,\mu\text{m}$; in this case with $w = 30\,\mu\text{m}$ the maximum angle is $\psi = 100\,\text{mrad}$. The separator still works for emittances larger than $3\,\mu\text{m}$ but at a reduced transmission.

2.1 Working hypothesis

In the previous section we introduced the concept of how a magnetic dipole generates dispersion in order to transversely separate particles of different masses at a selection slit.

The optics of a separator system is designed to focus the beam at the selection slit so the desired particles of mass m are transported downstream while the contaminant masses $m + dm$ are intercepted by the slit plates. Figure 2.4 is an artistic representation of a 180 degree separator with $D = 2\rho$; this is just a convenient example that gives the focusing properties needed. The design assumes a constant field (perfectly flat) within degree dipole magnet; a magnetic dipole with a constant field value B_0 between the poles and zero outside is called a hard-edge dipole. Any distortion (aberration) of the intended focus means that particles of mass m are intercepted by the slit plate while contaminant particles are transported downstream. This reduction in performance is a loss of resolving power. The magnetic field is one possible contributor to aberration, in particular because a real magnet does not have a perfectly flat field.

Based on equation 2.4 we know that, for a 20000 resolving power, a variation of B of $\frac{1}{40000}$ produces the same displacement at the selection slit
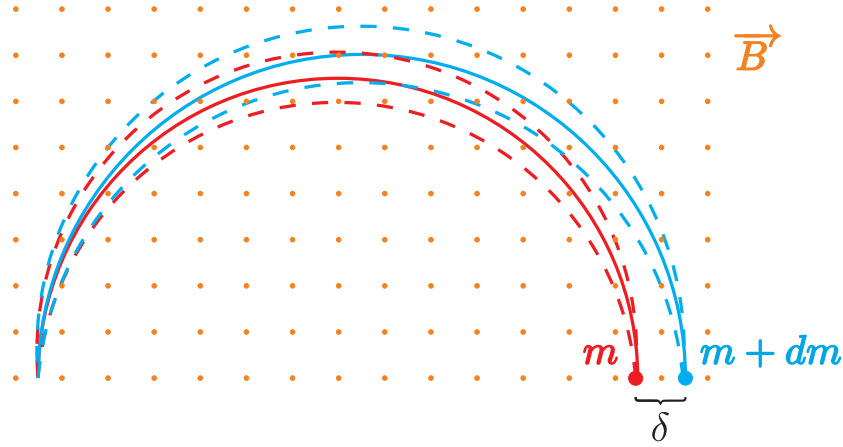
Figure 2.4: Artistic representation of particle separation for a 180 degree separator: the dashed lines represent the particles entering the separator with the largest angle ψ defining the width of the good field region.

as a variation in mass of $\frac{1}{20000}$. So a variation of this magnitude in the field shifts transversely a particle of mass m by the same amount necessary to separate it from a particle of mass $m + dm$. Because the curvature is an integral effect, we are ultimately interested in the field integral variation.

From the previous section we also know that the beam occupies a wide area (good field region) within the dipole so we are interested in the integral variation over the whole area in order to maintain the correct beam focus at the selection slit.

In this thesis we work under the hypothesis that minimizing the field integral variation with respect to the system resolution $(\frac{dm}{m})$ within the good field region is equivalent to reducing the magnetic field contribution to the system aberration. This means that the system corrections required to compensate for magnetic field imperfection are minimized.

The objective of the thesis is supporting this hypothesis through the magnetic field study. This study ultimately results in the design of the magnetic dipole for the High Resolution Separator (HRS)[9] of the ARIEL facility.

---

[9]Part of CANadian Rare isotope facility with Electron Beam (CANREB) project funded by Canada Foundation for Innovation (CFI)

2.2   Design requirements

The final HRS system design has to satisfy specific requirements[10]; the principal one is the achievement of a resolving power for the separator system of 20000 for a $3\,\mu$m (or mm·mrad) transmitted transverse emittance.

The magnetic dipole is the most critical hardware component of the HRS system. Our choice is to design a magnet that minimizes aberration in order to reduce the corrections necessary to achieve the desire resolving power; this is expected to produce a system easy to operate. The goal is to design a magnet that behave like a hard-edge dipole from an integral point of view within the good field region.

Our unique strategy, adopted to optimize the magnet, needs the formulation of the following definitions.

We define the reference geometric trajectory, already defined in general
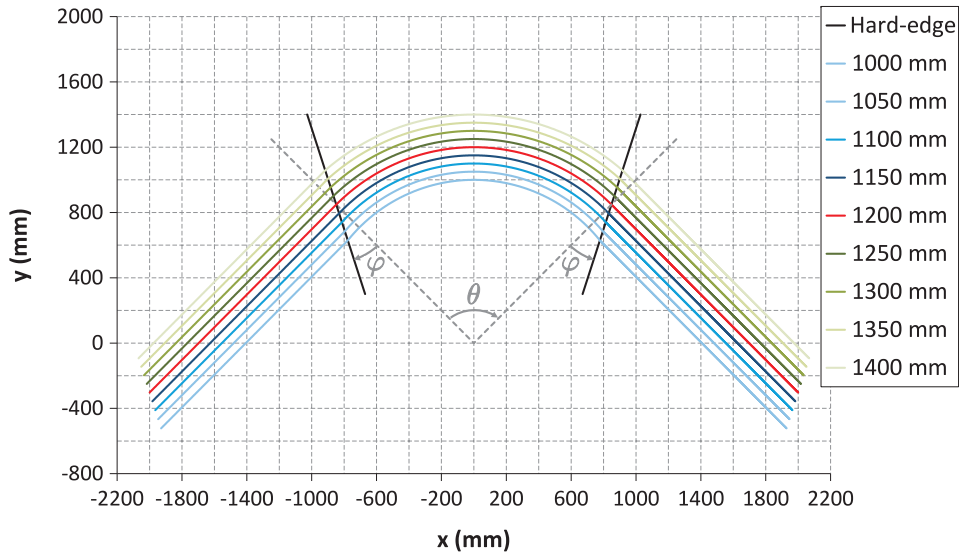
Figure 2.5: Geometric trajectories. The reference trajectory represented in red has a radius of curvature of 1200 mm. The black solid lines represent the field boundaries of the hard-edge magnet: φ is the edge angle. The bend angle $\theta = 90$ degree.

---

[10]ARIEL high resolution spectrometer requirements TRIUMF internal document-74319.

early in this chapter, as the path followed by the reference particle traveling through a hard-edge dipole magnet.

The reference geometric trajectory is the red path represented in figure 2.5; this is composed of an arc[11] inside the hard-edge boundaries connected on the outside to two straight paths tangential to the arc. Figure 2.5 shows also that the entrance and exit edges (hard-edge boundaries) have an angle φ with respect to a basic magnet where the faces are normal to the incoming and outgoing beam; later in section 2.4 we are going to discuss the entrance and exit edge angle of the reference geometry.

We consider also other geometric trajectories composed by an arc concentric to the reference one that ends at the hard edge boundaries and two straights parallel to the reference straight paths; these additional geometric trajectories are not meant to represent particle trajectories, but we choose them to gauge field quality through the integral calculated along them.

We define the field flatness (FF) as follows:

$$FF = \frac{B_z}{B_0} - 1 \tag{2.10}$$

where B_0 is the vertical component (z direction) of the magnetic field at the center of the realistic magnet (from OPERA); this center has coordinates (0,1200), see figure 2.7.

It is useful to think about the field flatness, and flatness in general, as an error, the smaller the better.

We define the integral ratio IR_ρ for any given geometric trajectory relative to a curvature ρ as follows:

$$IR_\rho = \frac{\int_\ell B_z(s)ds}{\int_{\text{arc}} B_0 ds} \tag{2.11}$$

where $B_z(s)$ is the magnetic field vertical component of the OPERA magnet

---

[11]The radius of the arc is related to the B_0, the mass and the velocity of the reference particle assumed to be single charged, as per equation 2.2: $\rho = \frac{mv}{eB_0}$

2.2. Design requirements

along the considered geometric trajectory of path ℓ. At the denominator the integral of the hard-edge case is computed only over the *arc* component of the geometric trajectory since the field integrals along the straights are zero by definition.

We lastly define the integral flatness IF_ρ as follows:

$$IF_\rho = \frac{IR_\rho}{IR_{1200}} - 1 \qquad (2.12)$$

where again the index ρ represents a geometric trajectory ($\rho = 1200\,\mathrm{mm}$ being the reference one).

The optimized design is achieved by studying the field flatness as a function of selected design parameters and by comparing the field integrals of the OPERA model with respect to the equivalent hard-edge case. Equivalent means that the hard-edge case has the same B_0 of the OPERA model.

The flatness requirements follow from equation 2.4, by calculating the differential in B and m we obtain the relationship between the field flatness and the resolving power:

$$\frac{dB}{B} = \frac{1}{2}\frac{dm}{m} \qquad (2.13)$$

The first optimization goal is a field flatness in the radial direction at the center of the pole of less than $2.5 \cdot 10^{-5}$ inside a region that extends $\pm 160\,\mathrm{mm}$ around the reference geometric trajectory in the middle plane. This region is defined by optics calculation and it is the area occupied by the beam (for a $3\,\mu\mathrm{m}$ emittance); this is referred as the good field region as mentioned in the opening section.

The second optimization goal derive from our working hypothesis and it required the integral flatness IF_ρ to be less than $2.5 \cdot 10^{-5}$ within the good field region. The integral flatness is a more stringent requirement than the field flatness because the overall curvature of the beam is an integral effect of the magnetic field.

The third optimization goal is related to the position of the effective

field edge with respect to the hard-edge case. In a real dipole the magnetic field has a soft transition from B_0 to zero (as opposed to the hard-edge); the effective edge is then defined as the integral of the field along some defined paths divided by B_0. In our case the defined paths are the geometric trajectories.

Because we want to design a magnet that reduces the amount of corrections necessary to match the beam dynamics designed optics, we request that the effective field edge location matches the hard-edge. This guarantees that the entrance and exit edge angles are correct. Based on practical considerations, we specify an upper limit for the $|IR_\rho - 1|$ being less than $1 \cdot 10^{-3}$. This specific requirement translates into an effective field edge position within 1 mm with respect to the hard edge case for a 2 m path length. It is possible to have the correct integral flatness and edge angle only if the effective edge match the hard-edge.

A final requirement is that the steel of the magnet doesn't reach saturation. This is a soft requirement and mostly driven by experience. A reasonable figure for field saturation is not to exceed 1.5 T. A better requirement related to field saturation is in fact to specify that the magnet behaves sufficiently linearly within the range of operation. The magnet must be able to bend beam rigidities (see equation 2.2) between 0.117 T m and 0.544 T m, corresponding respectively to $^{11}\text{Li}^{1+}$ and $^{238}\text{U}^{1+}$ at 60 keV, and to 0.097 T and 0.453 T magnetic field for the hard edge case and the chosen ρ. The linearity requirement means that the magnet has to satisfy the three previous requirements at these two extreme cases of operation.

2.3 Magnetic dipole model

In the opening section of this chapter we briefly introduced the concept of mass separation considering the simplified case of a stand alone magnetic dipole. In practice, the simplest possible layout consists of drift (absence of optical elements) spaces upstream and downstream of a dipole. In this case the dispersion of the system, rather than the magnet, is a result of the overall optical layout. Such a system is usually mechanically defined by the
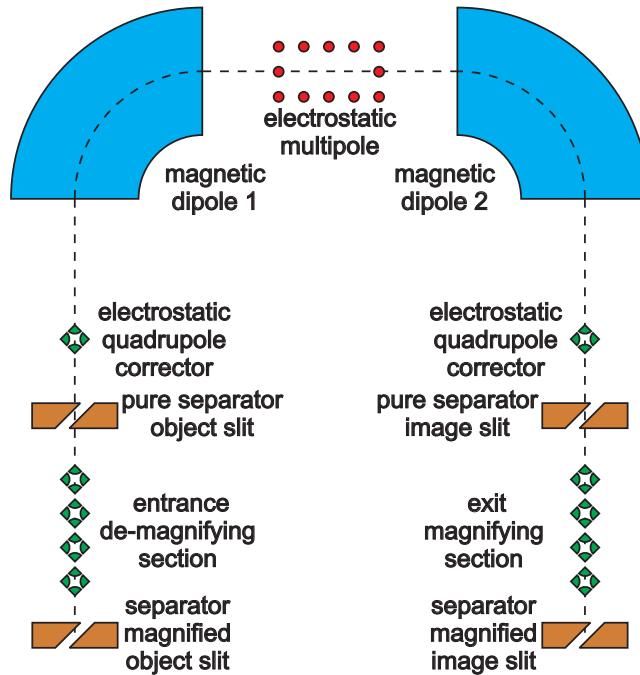
Figure 2.6: Schematic layout of the High Resolution Separator (HRS)

entrance (of the upstream drift) object slit and the exit (of the downstream drift) image, or selection, slit.

The final optical layout of the HRS system is represented in figure 2.6; it includes two identical 90 degree magnetic dipoles with a 1200 mm radius of curvature. Two magnets produced twice the dispersion of a single one. This layout is close to a single 180 degree dipole as seen in section 2.1, but it allows for the cancellation of some high order aberrations; a single 180 degree dipole would also be much more difficult to machine and handle.

Different layouts were initially evaluated based on first order beam dynamics calculations[12]. The final layout has been developed[1] accounting for higher order effects using the COSY INFINITY[41] (COSY-∞) code. The optical design occurred in parallel with the magnet design. Updates from the optics were incorporated in the magnet design as they were issued. The

---

[12]M. Marchetto, "ARIEL High Resolution Spectrometer First Order Calculations", TRIUMF internal design note TRI-DN-13-07, document-74265.

final realistic magnetic field is a result of this thesis work. This field was ultimately used in COSY-∞ to validate both the magnet and the optical design.

The magnetic dipole design has been developed with the 3D-modeller® of the OPERA-3D® software. The field calculation of the developed magnet has been calculated with the TOSCA® solver part of the same software.

The magnet steel, coils and surrounding air volume coordinates are parametrized as functions of the characteristic dimensions of the magnet: reference radius of curvature, angle of entrance and exit face, pole gap, etc. The parametrization reduces the design time and it allows for better tracking of the design parameters to be optimized.

Figure 2.7 shows an example of the steel coordinates. The parameterized coordinates are coded in a geometry generator file (OPERA COMI file). Figure 2.8 shows a rendering[13] of one of the basic dipole configurations; we refer to this as the reference geometry (HRS-120-12Cq2) generated with the COMI file.
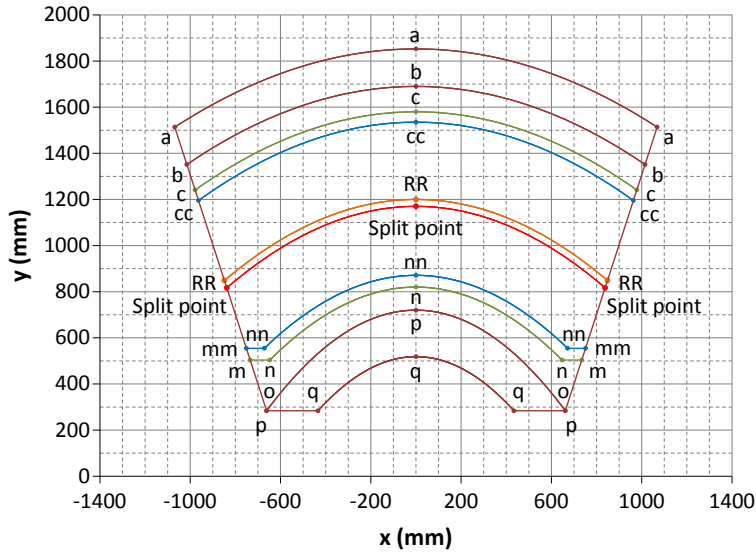
Figure 2.7: Example of parameterized coordinates of the HRS dipole

---

[13]All the magnet renderings presented in this thesis are an output of OPERA-3D® software. The OPERA logo and information frame will be removed from subsequent renderings only for presentation reasons.
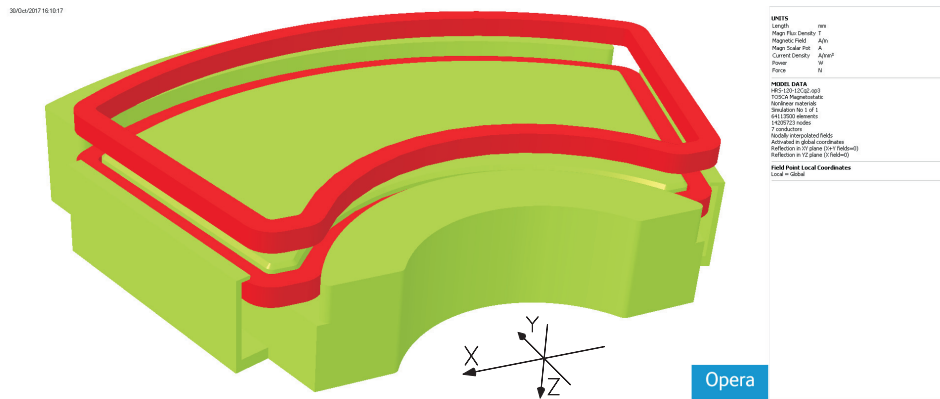
Figure 2.8: Rendering of the reference geometry (HRS-120-12Cq2): half magnet is represented but only one quarter is simulated.

The steel and coils geometry is immersed in an air background which dimension are at least a factor of five larger than the magnet geometrical dimensions. At the boundaries of this background (far-field boundaries) the field is null with respect to the field in and around the magnet.

By taking advantage of the magnet symmetries, we simulate only one quarter of the full magnet and air background. The xy ($z = 0$) symmetry plane has a normal magnetic boundary condition while the yz ($x = 0$) plane has a tangential magnetic boundary condition.

We impose total potential everywhere but in the dedicated air volume containing the coils where the reduced potential is required.

The standard HRS simulations use a tetrahedral element mesh limited in size, within the pole gap (the region of interest), to: $5\,\text{mm}^3$ for the volume, $5\,\text{mm}^2$ for the surface, $5\,\text{mm}$ for the edge and $1\,\text{mm}$ for the vertices. The steel tetrahedrons are limited to: $10\,\text{mm}^3$ for the volume, $10\,\text{mm}^2$ for the surface, $5\,\text{mm}$ for the edge and $1\,\text{mm}$ for the vertices. The air background is subdivided in various regions where the elements size is progressively increased from the steel to the outer boundaries to: $200\,\text{mm}^3$ for the volume, $200\,\text{mm}^2$ for the surface, $200\,\text{mm}$ for the edge and $200\,\text{mm}$ for the vertices. OPERA storage levels are set to prioritize the mesh size to be used at the boundaries between two geometrical elements (air gap and steel for example).

2.3. Magnetic dipole model

Table 2.1: Simulation statistics for coarse and fine mesh of an HRS geometry.

	Coarse mesh (simulation HRS23C56)	Fine mesh (simulation HRS23C57)
Number of:		
nodes	1.5 M	18.8 M
edges	1.9 M	83.7 M
mesh elements	1.5 M	70.4 M
Max element size:		
air gap	$6.25\,\text{mm}^3$	$5\,\text{mm}^3$
steel	$67\,\text{mm}^3$	$10\,\text{mm}^3$
background	$1333\,\text{mm}^3$	$200\,\text{mm}^3$
Iterations	8	12
Running time	15 min	10 h 45 min
Solution file size	460 MB	12,860 MB

A parameter coded in the COMI file allows for scaling the mesh dimensions. This feature is used to test the solution convergence; since the typical solution (fine mesh) is running at the limit of the available hardware, the convergence test is done by increasing the mesh size (coarse mesh) on the selected geometry. Some simulation statistics for a late geometry with fine and coarse mesh are listed in table 2.1; the solution for the two cases are within the same order of magnitude.

OPERA solve the Ampere's circuital law (Maxwell equation) using the non-linear Newton-Raphson iteration method; the maximum number of iterations is set to twenty-one.

The calculations use a typical steel C1006 BH curve, represented in figure 2.9, for the poles and return yokes. Steel C1006 is the typical soft magnetic steel with low carbon content, less than 0.08%, used in magnet production. A complete chemical analysis of the C1006 used to manufacture the HRS dipole magnet is reported in table 2.2.

In order to probe the final design, the relative geometry is simulated with a C1010 property steel (see figure 2.9) as well as with constant relative

permeability value of 500 and 2000. The final geometry is also simulated with a mix of steels, namely C1010 for the poles and C1006 for the rest of the magnet. Simulation results that used different permeability properties are consistent with the final geometry solution using C1006 steel.

Table 2.2: Chemical composition of the C1006 steel used to manufacture the HRS dipole magnets.

Element	Weight %	Element	Weight %	Element	Weight %
Fe	99.151	Cu	0.07	V	0.001
C	0.06	Si	0.07	Al	0.031
Mn	0.39	Ni	0.04	Cb (Nb)	0.001
P	0.04	Cr	0.04	N	0.007
S	0.02	Mo	0.02	O	0.004
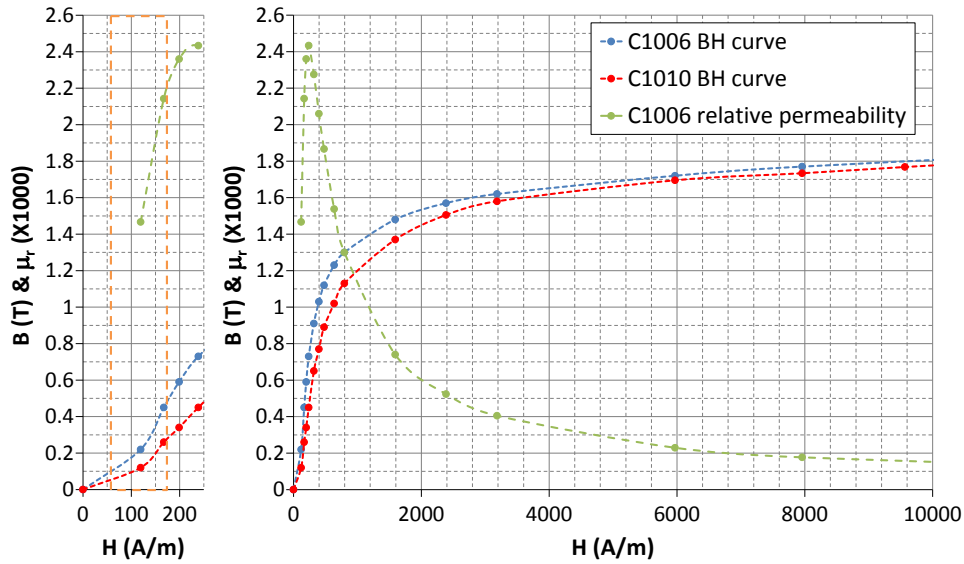
Figure 2.9: BH curves for C1006 and C1010 magnetic steel and relative permeability (see equation 2.15) for the C1006 steel. The narrow side graph is a magnification of the main one around the operational range (orange dotted box).

2.4   Reference geometry

The reference geometry (see figure 2.8) is the starting point of the opti-
mization; its dimensions are derived from main parameters like radius of
curvature (1200 mm), bending angle (90 degree), pole gap (70 mm) and edge
angle (27 degree) used in the beam dynamics calculations and by applying
some rules of thumb[14]. The initial coil section of 69×69 mm^2 has a current
density of around 2.6 A·mm^{-2} and it generates a field of about 0.45 T; the
field calculations are done for the maximum rigidity (0.544 T m).

   The vertical component of the magnetic field for the reference geometry
is represented in figure 2.10 as a function of the angle where zero corresponds
to symmetry axis of the magnet ($x = 0$ in figure 2.7). The field fall off is
significantly different from the hard edge case where the field goes to zero
with a discontinuity. Close views of the top and the fringe field profile are
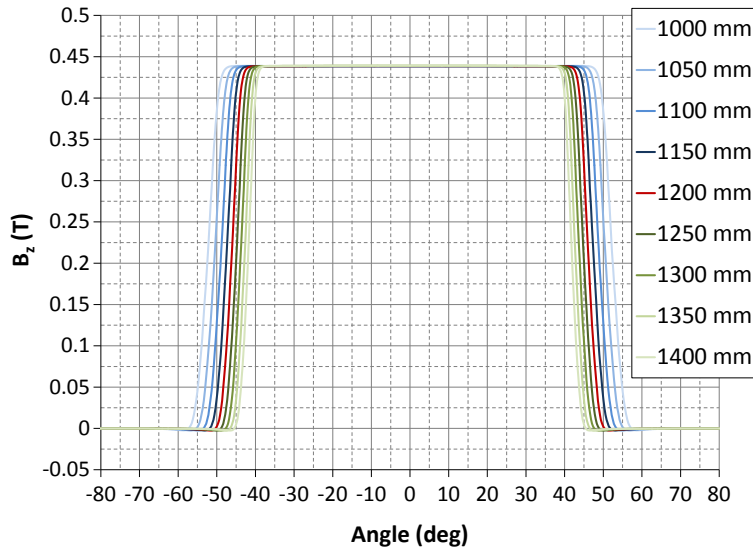
Figure 2.10: Reference design B_z vertical magnetic field component: the red
line represents the reference geometric trajectory. The hard edge case would
be a constant field at the maximum value, dropping to zero at 45 degree.

---

[14]private communication with P.Eng. George S. Clark, TRIUMF magnet engineer.

represented respectively in figure 2.11 and figure 2.12.
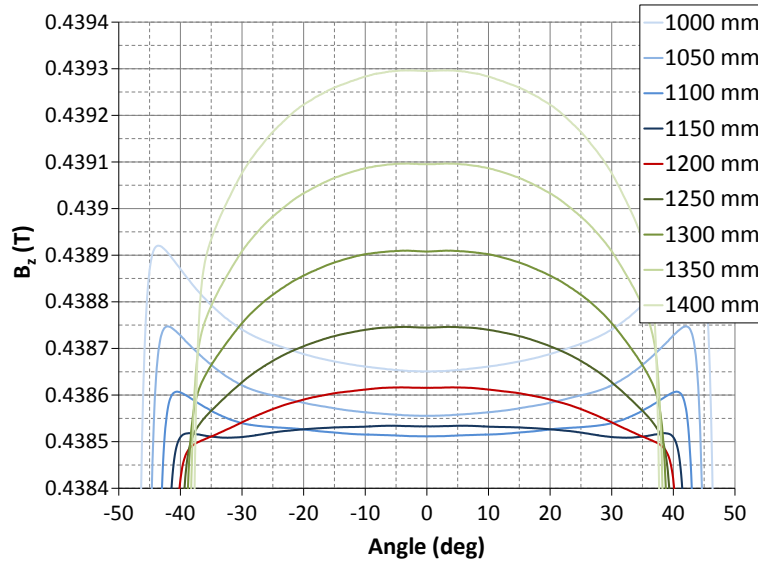
Figure 2.11: Reference design B_z vertical magnetic field component magnified near the peak. The field is symmetric with respect to 0 degree.
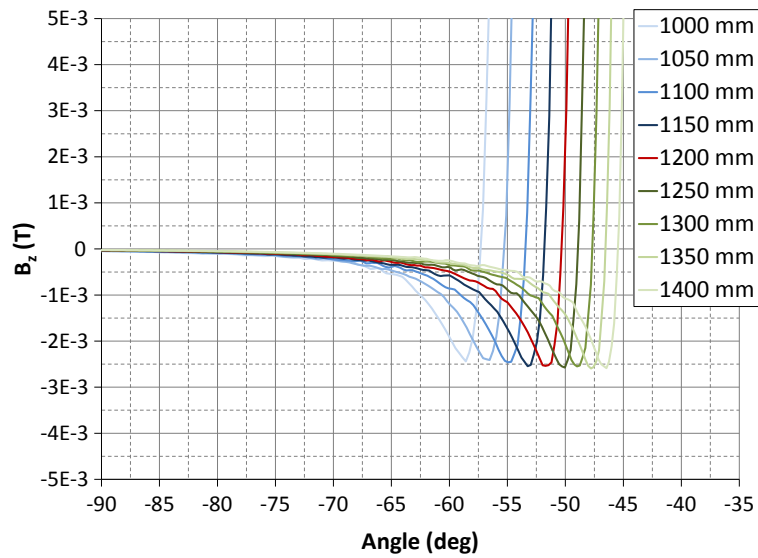
Figure 2.12: Reference design B_z vertical magnetic field component magnified around the fringe field (drop off).
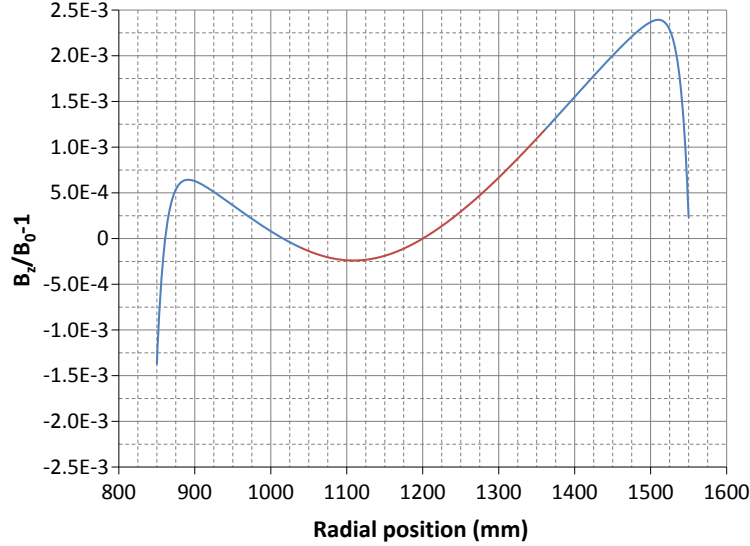
Figure 2.13: Reference design field flatness: the red portion of the curve represents the flatness within the good field region ($\pm 160\,\text{mm}$ around the reference geometric trajectory $\rho = 1200\,\text{mm}$).

The field flatness in the radial direction along the magnet symmetry axis is represented in figure 2.13. The red section of the curve corresponds to the portion within the intended good field region. In this case the field flatness presents a strong asymmetry, circa $2 \cdot 10^{-3}$; there is a larger magnetic field on the outer part of the pole. This field flatness doesn't meet the $2 \cdot 10^{-5}$ requirement.

The asymmetry can also be seen by looking at the magnetic field distribution of the steel, represented in figure 2.14, where the inner return yoke presents a higher level of saturation with respect to the outer one.

The return yoke refers to the part of the steel where the magnetic flux is forced to loop around going from the magnetic south to the magnetic north pole, where the orientation depends on the electric current direction flowing through the coils. The magnetic field strength follows the equation:

$$B = \mu H \tag{2.14}$$

44
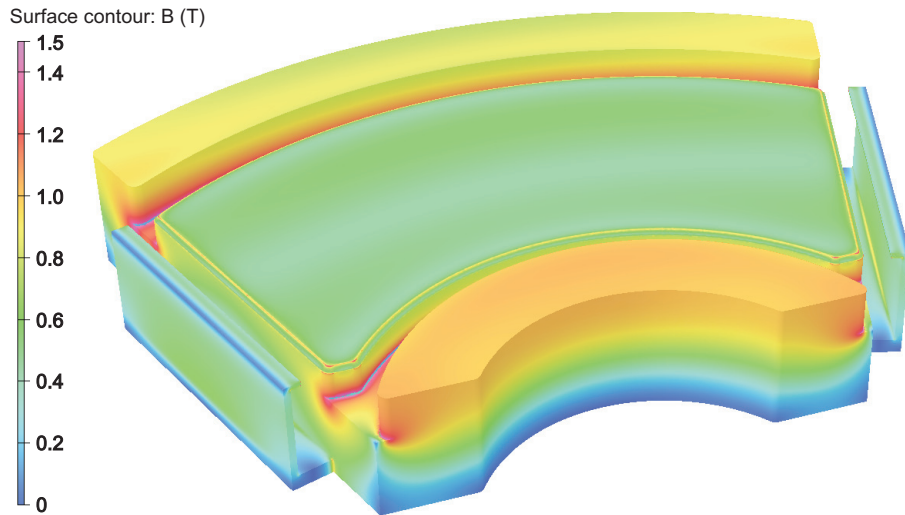
Figure 2.14: Reference design magnetic flux density in the steel (half magnet). The external return yoke surface (yellow) is larger than the internal (orange).

where μ is the permeability of the material (air, steel, etc.) and H is called the magnetizing field. In the SI system B is measured in T (teslas), μ in H·m^{-1} (henrys per inverse meter) and H in A·m^{-1}. The permeability of free space, air for our purpose, is indicated with μ_0 and it has a value of $4\pi \cdot 10^{-7}$ H·m^{-1}. More often the permeability is indicated relative to air; equation 2.14 becomes then:

$$B = \mu_r \mu_0 H \tag{2.15}$$

where $\mu_r = \frac{\mu}{\mu_0}$ is the relative permeability.

Incidentally, in the Centimetre-Gram-Second system of units (CGS), where B is measured in G and H in Oe ($1\,\text{Oe} = 1000/4\pi$ A·m^{-1}) equation 2.15 is simply:

$$B = \mu_r H \tag{2.16}$$

As seen in figure 2.9, the permeability is not a constant and it decreases for high magnetization field due to saturation.

Consider now the magnetic flux $\Phi_B = B \cdot S$ where S indicates the cross-sectional area where the flux is calculated. The reference design (see figure 2.14) has the outer yoke surface larger than the inner one. As the coil current is ramped up (increasing H) the magnetic flux will tend to flow equally through both return yokes, but since the inner one has a smaller surface, the magnetic field is going to be larger with respect to the outer one. Larger magnetic field corresponds to lower permeability.

The flux through a return yoke can be written as:

$$\Phi_B = \mu_r H S \tag{2.17}$$

The outer return yoke has at this point larger surface and higher permeability, therefore the magnetic field tends to move toward the outer return yoke.

This behavior has some analogy in Ohm's law for a conductor, where H is the voltage, Φ_B the current and μ_r^{-1} the resistance. If we have two resistors (μ_{r1}^{-1} and μ_{r2}^{-1}) connected in parallel to a common voltage (H), the current (Φ_B) is higher through the lower resistance (higher μ_r). The magnetic resistance is called reluctance; the reluctance of a uniform magnetic circuit is described by the following equation:

$$\mathcal{R} = \frac{l}{\mu_0 \mu_r S} \tag{2.18}$$

where l is the length of the magnetic circuit.

The integral ratios for the reference geometry are calculated along the geometric trajectories represented in figure 2.5. These nine trajectories are spaced $50\,\text{mm}$ apart from an inner bending radius of $1000\,\text{mm}$ to an outer of $1400\,\text{mm}$, $1200\,\text{mm}$ being the reference radius of curvature as per the beam dynamics. The straight paths extend $1628\,\text{mm}$ beyond the hard edge boundaries; this is to allow for the field to decay low enough so it doesn't

Table 2.3: Magnetic field integrals for the reference geometry.

Geometric trajectory ρ (mm)	Hard edge $\int_{arc} B_0 ds$ (T mm)	Reference geometry $\int_\ell B_z(s) ds$ (T mm)	IR_ρ
1000	781.00	800.92	1.0255
1050	791.83	811.56	1.0249
1100	803.13	822.81	1.0245
1150	814.10	834.53	1.0242
1200	826.77	846.44	1.0238
1250	838.99	858.92	1.0238
1300	851.40	871.64	1.0238
1350	863.98	884.34	1.0236
1400	876.70	897.70	1.0240

contribute significantly to the integral. The results on the magnetic field integrals for the reference geometry are listed in table 2.3. The calculated field integral along the reference trajectory is circa 0.846 T m for a field at the center of the pole, B_0, equal to 0.439 T m; for reference, $^{238}U^{1+}$ requires a integral field along the reference trajectory of 0.854 T m.

The integral ratios give an indication of how the effective edge compares with the hard edge case. This is easier to visualize if we calculate the amount of effective path length that extends beyond the hard edge case as follows:

$$\Delta\ell = (IR_\rho - 1)\frac{\text{arc}}{2} \qquad (2.19)$$

where the total amount has been divided by two because the effective length extend symmetrically on both side of the magnet. The result of such a calculation is shown in figure 2.15; the two extreme cases, 1000 and 1400 (light color on the graph) are outside the good field region.

The effective field edge is circa 22 mm beyond (outward) the location of the hard edge case and it presents curvature with respect to the hard edge case (no curvature). The effective edge has also the wrong angle with respect to the hard edge design. The latter has in fact by design a 27 degrees entrance and exit angle, defined earlier in section 2.2 and shown in figure 2.5;
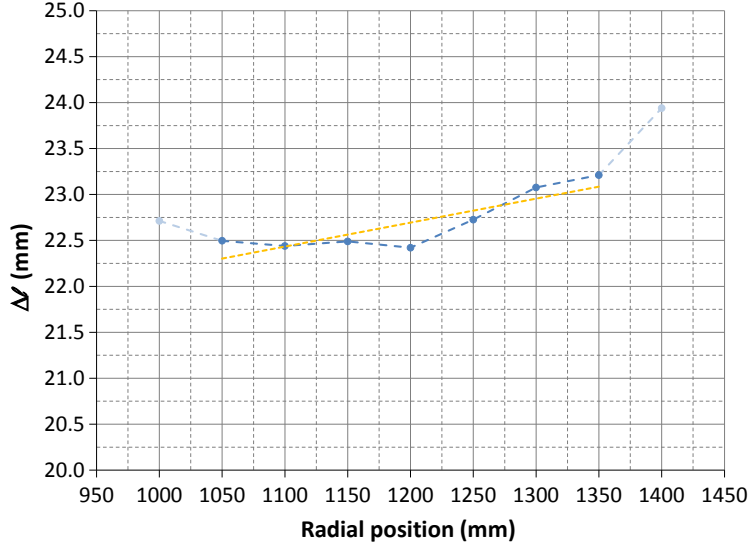
Figure 2.15: Reference design effective field edge location with respect to the relative hard edge case. The light blue points are outside the good field region. If the effective edge aligned with the hard edge case the yellow dotted line (linear interpolation of the dark blue data) would be the constant $y = 0$.

such angle is a beam dynamic feature that provides vertical focusing to the beam. If the effective angle was correct, the yellow dashed line in figure 2.15, a linear interpolation of the good field region points, would be parallel to the horizontal axis. In this case the angle error is 0.15 degree (or 2.7 mrad).

Lastly the integral flatness of the reference model is calculated for the same reference trajectories used for the integral ratios. The results are plotted in figure 2.16. The integral flatness confirms the initial outcome of the field flatness with the magnet not meeting the requirement represented by the green box ($2.5 \cdot 10^{-5}$ high) in figure 2.16; the requirement is violated by a factor of 52.

It is interesting to notice that the inner trajectory integrals are higher than the outer ones even though the opposite occurs when we look at the field flatness (figure 2.13). However the field flatness is just a local snapshot at the center of the magnet while the integral represents a more global view.

2.4. Reference geometry

In order to explain the apparent contradiction we have to look at the field of the edge of the magnet in figure 2.11; the magnetic field increases at the edges of the magnet for the inner trajectories rather than dropping off as for the outer ones. This is due to the unbalance of the field distribution over the whole pole surface and return yokes as can be seen in figure 2.14; this issue is going to be addressed later in section 3.4 and section 4.3.
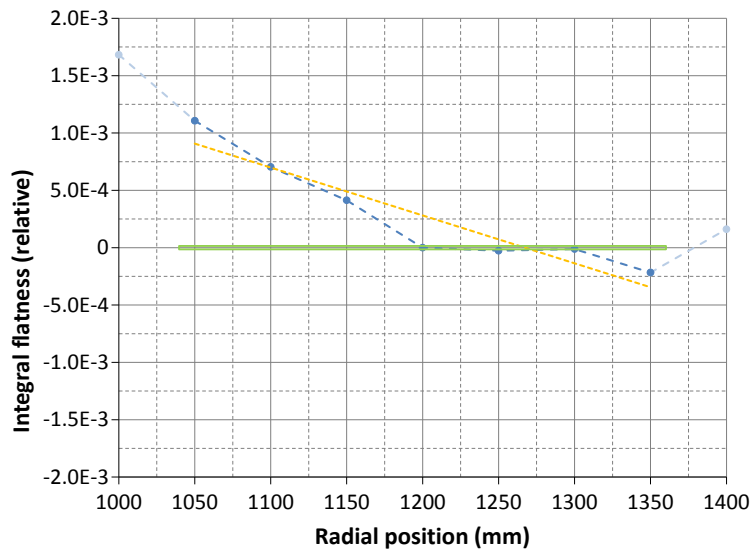
Figure 2.16: Reference design integral flatness with respect to the relative hard edge case. The light blue sections of the graph are outside the good field region. If the integral flatness matched exactly the hard edge case the points would lay on the x-axis (y=0). The green box $(2.5 \cdot 10^{-5}$ high) represents the flatness requirement in the good field region.

Chapter 3

Field Study on the Reference Geometry

Based on the reference geometry initial results presented of the previous chapter, it is important to understand how the steel geometry shapes the magnetic field. This is going to result in producing the optimum geometry that satisfies our requirements. In this chapter we are going to optimize the reference geometry with straight edges while the final curved edge geometry is going to be discussed in the next chapter.

3.1 Pole gap optimization

The first parameter of the magnet to be optimized is the separation between the two magnetic surfaces, the pole gap, where the beam goes through. The bending angle and the radius of curvature of the magnet are defined by the beam dynamics and they are considered given parameters for the magnet design. The beam dynamics doesn't specify the pole gap, but it does set a lower limit based on the vertical envelope of the beam; this envelope is circa $10\,\mathrm{mm}$ for a vertical emittance of $6\,\mu\mathrm{m}$ (design value[15]). A $40\,\mathrm{mm}$ vertical clearance for the beam would allow for a $100\,\mu\mathrm{m}$ emittance to be transported. The maximum emittance that can be transported is called acceptance. Another constraint to take in consideration for the pole gap is the wall thickness of the vacuum chamber.

 The initial gap dimension of $70\,\mathrm{mm}$ takes into account both the vertical beam envelope and the vacuum chamber dimension ($22\,\mathrm{mm}$, top and bottom

---

[15]Horizontal and vertical emitances can be different.

wall combined). This initial dimension also includes some engineering safety factor that allows some spatial contingency for machining error or beam misalignment.

There is a simple relationship between the gap, the magnetic field in the gap and the current that generates the magnetic field. This relationship can be derived using Maxwell's equation for magnetic field and static electric field (Ampere's circuital law - integral form):

$$\oint_{\partial\Sigma} \overrightarrow{H} \cdot d\overrightarrow{l} = \int_{\Sigma} \overrightarrow{j} \cdot d\overrightarrow{S} \tag{3.1}$$

By integrating along the circuit (red loop) represented in figure 3.1(top)

Figure 3.1: Cross section of the reference geometry in the middle of the magnet; the green contour represents the shape of the steel. Magnetic field B (top) and magnetizing field H (bottom) in the reference geometry. The red loop is the integration circuit $\partial\Sigma$ of equation 3.1.

3.1. Pole gap optimization

we have that the magnetizing field H can be split into the one inside the gap and the one inside the steel:

$$H_{gap}\, g + H_{steel}\, l = I \tag{3.2}$$

where I is the total current flowing trough the magnet coils and $g + l$ is the total length of the loop. Equation 3.2 can be written in terms of the magnetic field and the permeability of the material:

$$\frac{B_{gap}}{\mu_0} g + \frac{B_{gap}}{\mu} l = I \tag{3.3}$$

where we approximate B as the same magnitude in the gap as in the steel while $\mu \gg \mu_0$ for non saturated steel ($\mu_r = \frac{\mu}{\mu_0} \gg 1$ as seen in figure 2.9) and therefore the second term of equation 3.3 can be assumed zero; later in this section we will address the finite permeability case. We can arrive at the same conclusion by just looking at the H component in figure 3.1 (bottom). From equation 3.3 we then have that:

$$B_{gap}\, g = I \mu_0 \tag{3.4}$$

that means reducing the gap allows to run a lower current through the coils for the same magnetic field as well as to reduce the steel volume, without reaching saturation, leading to an overall less expensive design.

If the dipole had an infinite wide pole, and infinite permeability (as we will see later), the field would be constant everywhere similarly to an infinite parallel plate capacitor. In this non realistic case the field flatness would be zero (perfect field flatness) like for the hard-edge dipole. In a real dipole with finite pole width the magnetic field varies as we move from the center to the pole edges (as in a real capacitor).

For an H-frame dipole (like our case) it is expected that reducing the gap [42] increases the normalized pole overhang. The latter is defined as the

extension of the pole width a beyond the good field region normalized to the pole gap, necessary to reach a certain field flatness within the good field region itself.

The approximate dependency between the field flatness in the good field region and the normalized pole overhang $\frac{a}{g}$ for an unoptimized pole[16] is described by the following empirical equation:

$$\frac{\Delta B}{B} = \frac{1}{100}e^{-2.77(\frac{2a}{g}-0.75)} \tag{3.5}$$

where $\frac{\Delta B}{B}$ is the relative field error (field flatness). Figure 3.2 represents the dependency described in equation 3.5. As the gap g is reduced the normalized pole overhang $\frac{2a}{g}$ increases producing a better (smaller) flatness.
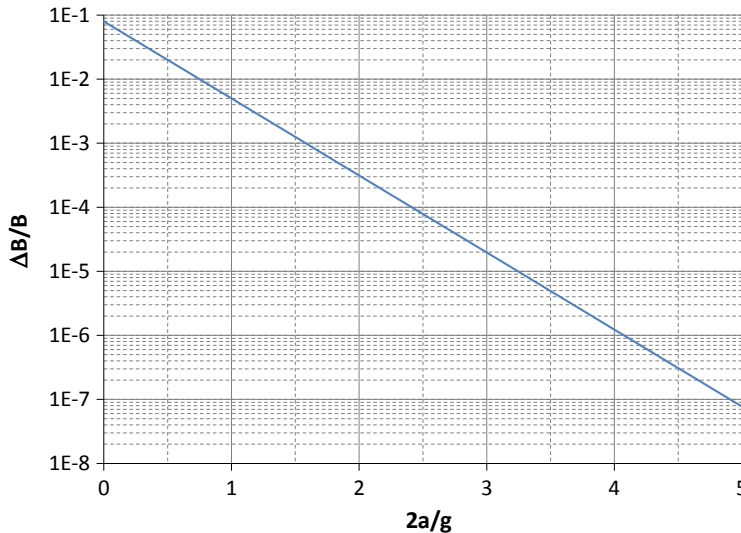
Figure 3.2: Field flatness as a function of pole overhang.

As represented in figure 3.3, our calculations show though that this is not the case for our magnet . A 50 mm gap required 26% less current but it produces a 40% worse (bigger) flatness. On the other end an 80 mm gap required 15% higher current but it results in a 12% better (smaller) flatness.

---

[16]see section "*The "H" Dipole Geometry*" chapter "Pole Tip Design" in "Iron Dominated Electromagnets Design, Fabrication, Assembly and Measurements" [42]
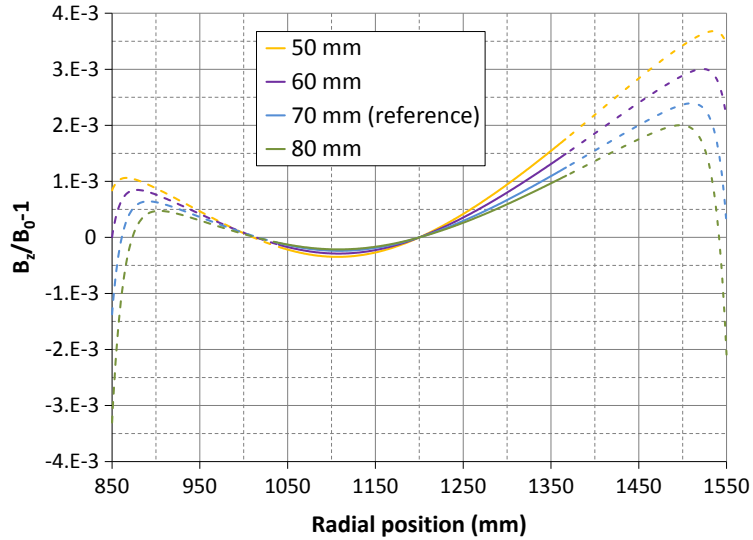
Figure 3.3: Field flatness dependency on the pole gap; the solid line represents the flatness within the limit of the geometric trajectories.

This result, in contrast with the normalized pole hangover approximation, is made evident by the magnet operating far away from saturation. As seen in section 2.2, this operational mode is necessary in order to have a linear behavior of the magnetic field for a large range of excitation. The field flatness dependency on the gap at different excitation levels has been studied for a simpler geometry: a "cube" magnet represented in figure 3.4.
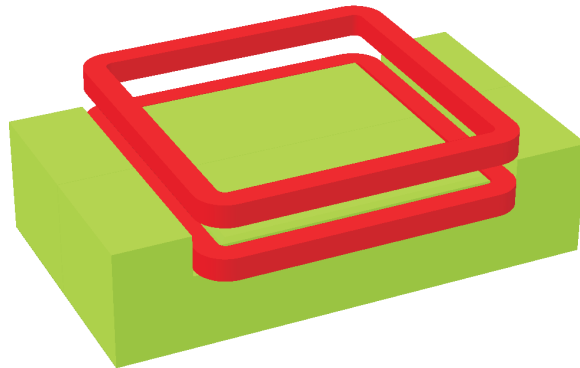
Figure 3.4: Rendering (half magnet) of the "cube" geometry.

3.1. Pole gap optimization

Figure 3.5 shows the magnetic field distribution of the cross section in the middle of the magnet (70 mm gap) for a low excitation mode, where the magnet doesn't reach saturation in the steel, and high excitation mode, where saturation occurs.
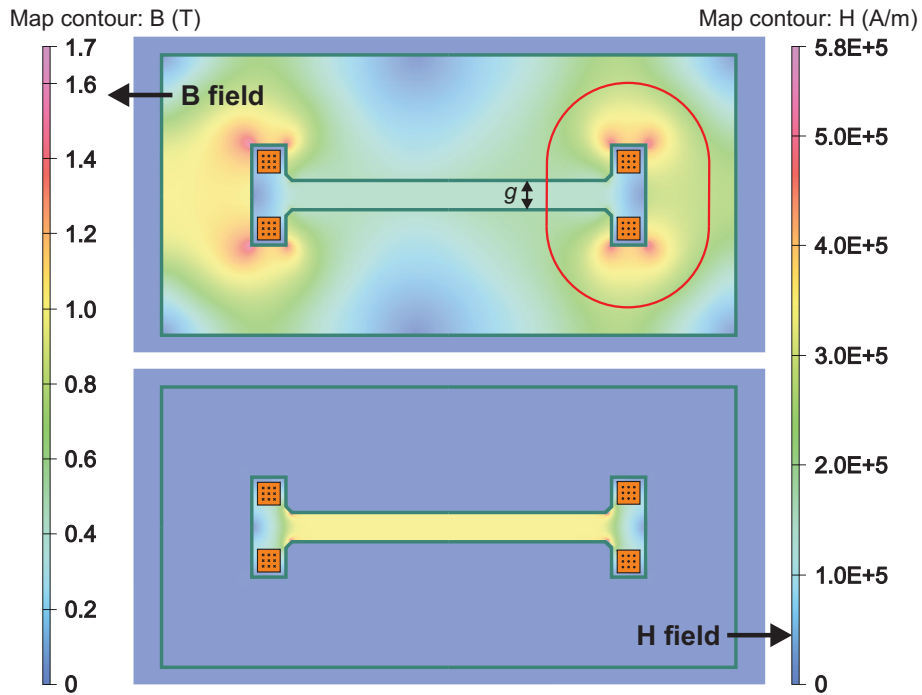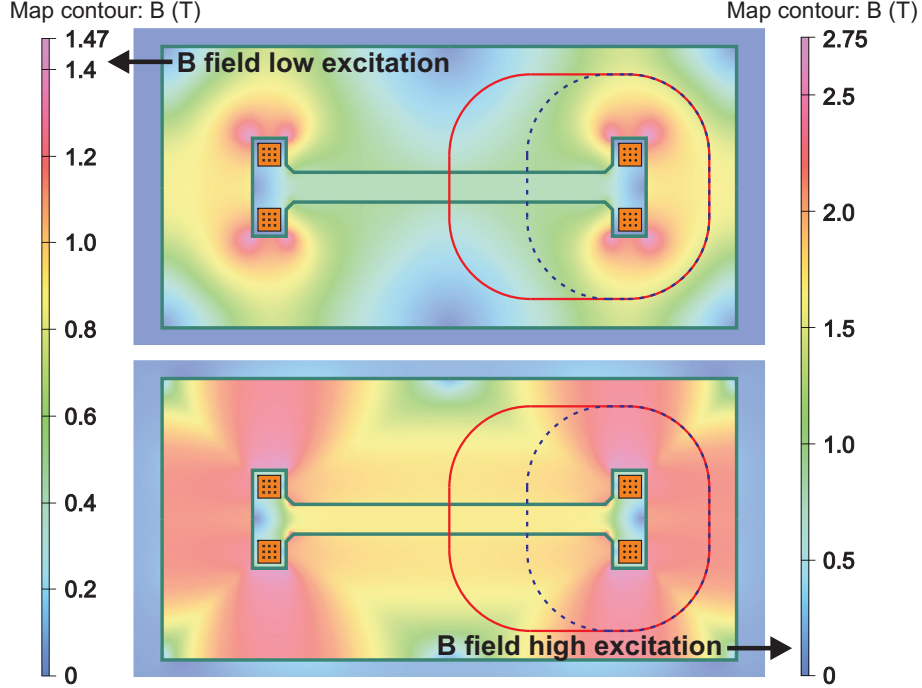

Figure 3.5: Cross section of the "cube" geometry in the middle of the magnet (70 mm gap); the green contour represents the shape of the steel. Field flatness of the "cube" geometry.

We apply equation 3.3 to two different loops as shown in figure 3.5: the large loop, loop-1 (red solid line), goes through the gap at the center of the magnet while the small one, loop-2 (blue dotted line), goes through the gap at 200 mm from the center of the magnet. For loop-1 we have:

$$\frac{B^1_{gap}}{\mu_0} g = I - \frac{B^1_{gap}}{\mu^1}(l + \Delta l) \tag{3.6}$$

where Δl is the path length difference with respect to loop-2 and μ^1 is the

average permeability of the steel along loop-1.

Similarly for loop-2 we have:

$$\frac{B_{gap}^2}{\mu_0}g = I - \frac{B_{gap}^1}{\mu^2}l \qquad (3.7)$$

where we made the approximation that the field in the steel is uniform and equal to B_{gap}^1.

Subtracting equation 3.7 from 3.6 we have:

$$\frac{\Delta B}{B} = \frac{B_{gap}^2 - B_{gap}^1}{B_{gap}^1} = \frac{1}{g}\left(\frac{\mu_r^2(l + \Delta l) - \mu_r^1 l}{\mu_r^1 \mu_r^2}\right) \qquad (3.8)$$

where we introduce the average relative permeability μ_r^1 and μ_r^2.
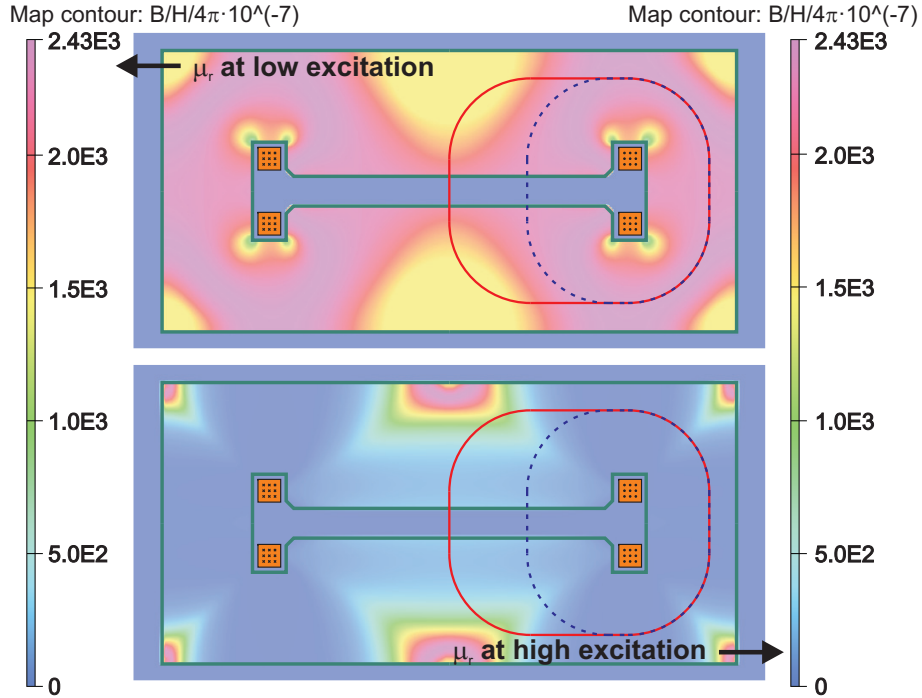
Figure 3.6: Relative permeability for the low (non-saturated - top) and the high (saturated - bottom) excitation case.

3.1. Pole gap optimization

The relative permeability in the steel for the low (non-saturated) and high (saturated) excitation mode is represented in figure 3.6.

If we assume the average relative permeability for the two loops to be the same, a good approximation for the low excitation (non-saturated) case, then the numerator of equation 3.6 is positive with:

$$\frac{\mu_r^1}{\mu_r^2} < \frac{l + \Delta l}{l} \tag{3.9}$$

$\frac{l + \Delta l}{l} \sim 1.2$ for the two loops we picked, and equation 3.8 simplifies into:

$$\frac{\Delta B}{B} = \frac{\Delta l}{g \mu_r^1} \tag{3.10}$$

for our case $\Delta l = 400\,\mathrm{mm}$, $g = 70\,\mathrm{mm}$ and $\mu_r^1 = 2200$ we have $\frac{\Delta B}{B} = 2.6 \cdot 10^{-3}$; the field at the $200\,\mathrm{mm}$ crossing is higher than the field at the
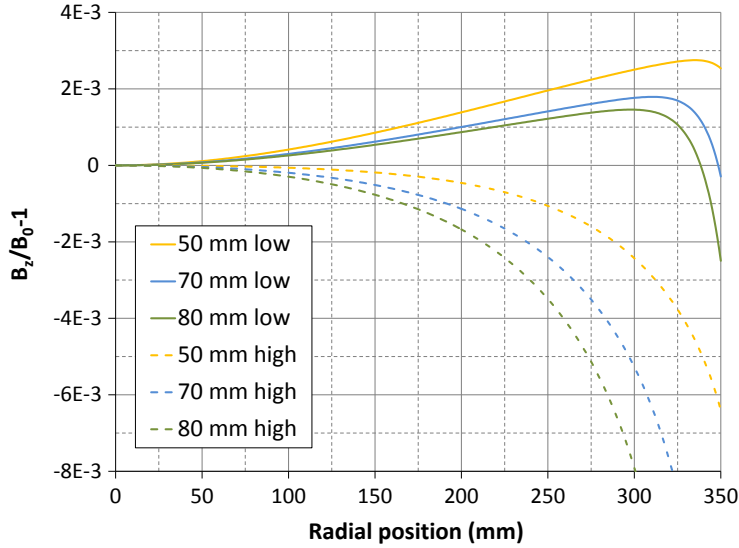
Figure 3.7: Field flatness of the "cube" geometry dependency on the pole gap and saturation level: solid and dashed lines represent respectively the low excitation (non-saturated) and high excitation (saturated) case.

center of the magnet.

This is in line with the field flatness results obtained for the cube geometry, represented in figure 3.7: here we see that for the 70 mm gap, the field at 200 mm is $1 \cdot 10^{-3}$ higher with respect to the center of the magnet; in fact if we picked a smaller loop that crosses the center and goes through a path with higher μ_r, as the magnetic flux does (lower reluctance), the two field flatness values would be closer.

If the relative permeability was infinite than we would have a perfectly flat field, but since it is finite, the flatness depends on how the permeability related to the gap aspect ratio $\frac{\Delta l}{g}$.

In the high excitation case, a much less uniform permeability leads to a field distribution in the steel that counteracts the effect described in the low excitation case. If we have that μ_r^1 is greater that μ_r^2, as for the high excitation (saturated) case (see figure 3.6), and that:

$$\frac{\mu_r^1}{\mu_r^2} > \frac{l + \Delta l}{l} \tag{3.11}$$

then the numerator of equation 3.6 is negative. In this case the field at the 200 mm crossing is lower with respect to the field at the center as shown in figure 3.7.

Magnets used to transport single species at a fixed energy like protons, electrons or heavy ions used as driver beam in the in-flight facility, don't need to behave linearly and therefore are often designed to operate closer to saturation with a minimum amount of steel (minimum cost). Beam lines designed to transport a variety of heavy ions have to employ magnets that behave linearly at the expense of under utilizing the available steel; in our case there are pockets of steel with almost no magnetic flux (see figure 3.1). Figure 3.8 shows the reference geometry (70 mm gap) field distribution in the steel levels for low (selected operational mode) and high excitation.

The initial gap dimension of 70 mm is the selected value providing a good compromise between current and flatness.
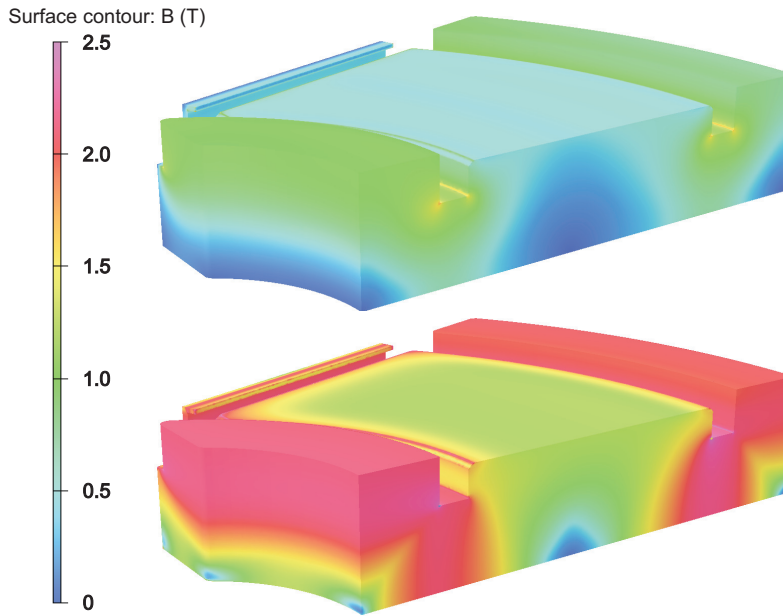
Figure 3.8: Reference geometry magnetic flux density in the steel for low (selected operational mode - top) and high excitation (bottom).

3.2 Flatness versus pole height

In order to study how the flatness changes with the pole height, we consider the pole composed of two sections as illustrated in figure 3.9: the pole and the pole base. The boundary of the two regions is the plane that contains the base of the coil channel.
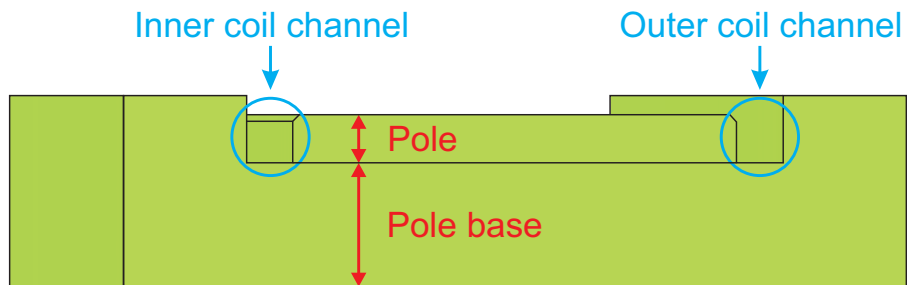
Figure 3.9: Reference geometry middle section.

3.2. Flatness versus pole height

A first set of simulations is done by fixing the pole base height at 229.5 mm, as for the reference geometry, and varying the pole height. The coil elevation with respect to the horizontal middle plane is also fixed. The pole height is changed from 90 mm (reference) to 180 mm in steps of 30 mm.

The results of this investigation are displayed in figure 3.10. The thicker the pole the better the value for the flatness. The flatness difference between the 90 mm and the 180 mm cases is $9 \cdot 10^{-4}$; this value drops to $3 \cdot 10^{-4}$ in the good field region.

The field distribution in the steel for the two extreme pole height cases is represented in figure 3.11. A thicker pole allows for a more uniform magnetic field distribution over the pole surface at interface with the air gap.

A second set of simulations is done by fixing both the pole height at 180 mm and the unchanged pole base, and varying the vertical position of the coil by moving it toward the base of the coil channel. The coil is moved down in two steps each of 30 mm. The result is shown in figure 3.12.
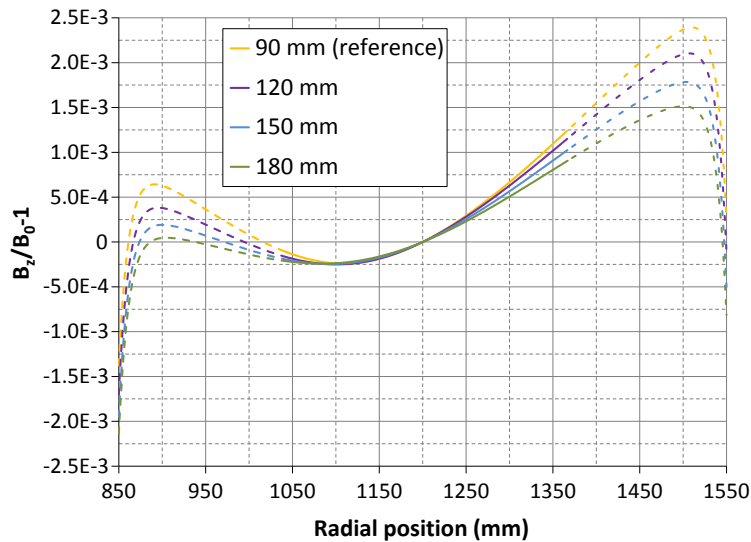
Figure 3.10: Flatness dependency on the pole height.
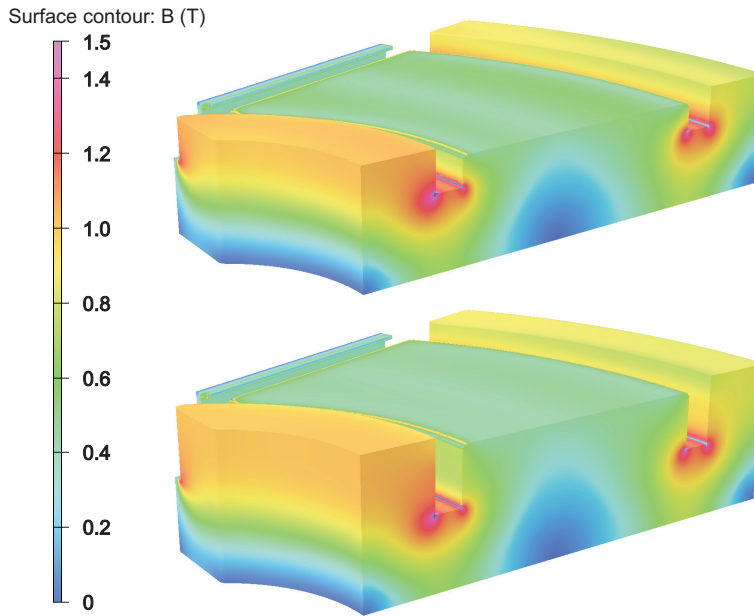
Figure 3.11: Magnetic flux density in the steel for the two extreme cases of pole height: 90 mm (reference design - top) and 180 mm (bottom).
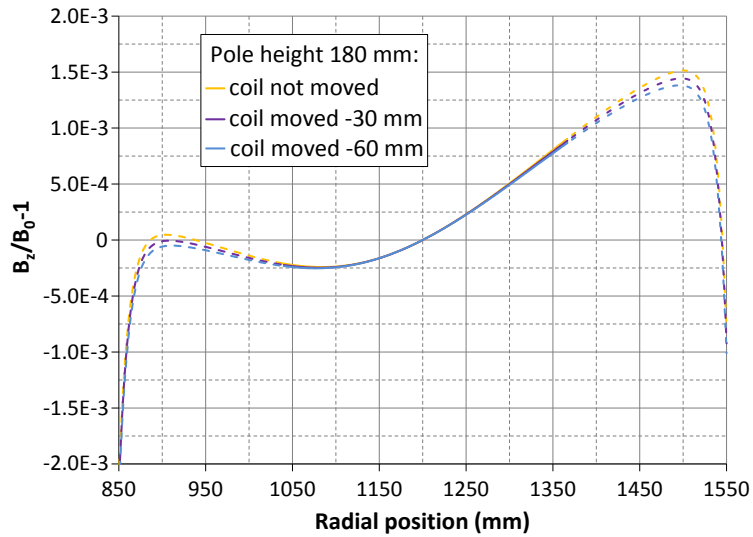
Figure 3.12: Flatness dependency on the coil vertical position. The case with pole height at 180 mm and coil not moved is the same as in figure3.10.

3.2. Flatness versus pole height

The flatness difference between the two extreme positions of the coil is almost one order of magnitude smaller with respect to the first set ($3 \cdot 10^{-5}$ within the good field region).

A third set of simulations is done with the pole height and the elevation of the coil fixed and varying the height of the pole base $\pm 60\,\text{mm}$ around the starting value of $229.5\,\text{mm}$. Increasing pole base thickness improves the flatness as shown in figure 3.13.

The field distribution in the steel for the two extreme pole base thicknesses is represented in figure 3.14. These can be compared with the field distribution in figure 3.11 (bottom picture).
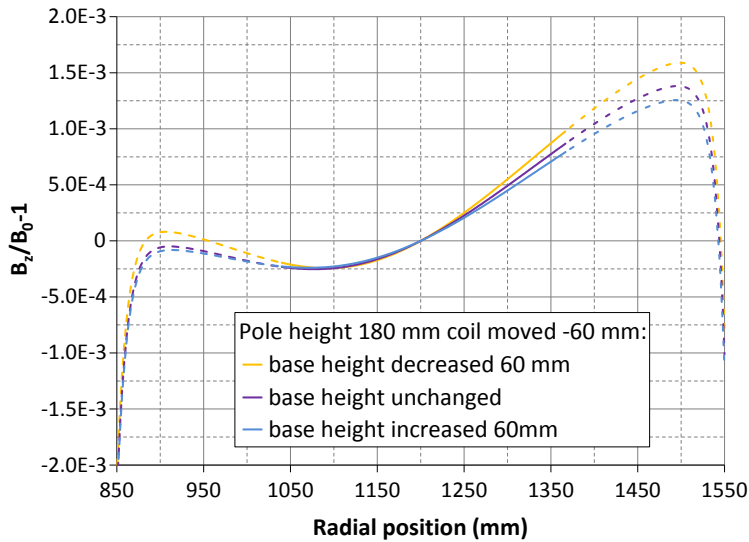
Figure 3.13: Flatness dependency on the pole base height. The case with pole height at $180\,\text{mm}$, coil moved $-60\,\text{mm}$ and base height unchanged is the same as in figure 3.12.

The design of a thicker pole improves the field flatness but it results in a heavier and more expensive magnet due to the increase in steel volume. The pole thickness is then going to be a compromise between field quality and magnet cost.

Even though the location of the coil gives marginal improvement of the

Surface contour: B (T)

Figure 3.14: Magnetic flux density in the steel for the two extreme cases of pole base height: 169.5 mm (top) and 289.5 mm (bottom).

flatness, it is mechanically practical to sit the coil at the base of its channel. Another consideration is that the coil section imposes a lower limit on the thickness of the pole since the coil channel (see figure 3.9) has to be deep enough to accommodate the coil itself and the latter can not interfere with the vacuum chamber located in the pole gap.

3.3 Flatness versus pole width

At the edges of the pole the magnetic field drops (edge effect); based on the results we have obtained so far, it is expected that a field drop at the edges improves the field flatness up to the point where the edge effect is so strong that the flatness starts to worsen (ΔB increases).

The dependency of the field flatness on the pole width is displayed in figure 3.15. Starting from a reference 826 mm, the pole width is increased up to 926 mm and down to 526 mm in steps of 100 mm. The edge effect starts

Figure 3.15: Flatness dependency on the pole width.

compromising the field flatness at the lowest width value simulated, where a local maximum can be seen at one extreme of the good field region.

The field distribution in the steel for the two extreme pole widths is represented in figure 3.16. The 526 mm pole width option has a more uniform saturation; this is due to the fact that the return yoke inner and outer surfaces combined are almost equal to the pole surface; this issue is discussed in detail in the section 3.4.

The best result in terms of flatness is the 526 mm case; this is consistent with the findings in section 3.1. Considering equation 3.10, we are reducing Δl by forcing the magnetic flux into a smaller region (or similarly constraining loop-1 and loop-2 to have closer paths).

In the 526 mm case though, the good field region is on the edge of the field fall off. A higher value of the pole width, like 626 mm, is preferable; this is also in line with the beam dynamics study[1] that looks at the correlation between pole width and high order aberration.

Figure 3.16: Magnetic flux density in the steel for the two extreme cases of pole width: 926 mm (top) and 526 mm (bottom).

3.4 Magnetic flux balance

The radial symmetry of the reference design (same width of the return yokes) results in a higher magnetic flux through the inner yoke (smaller surface) with respect to the outer one, as represented in figure 2.14 This asymmetry in the flux distribution causes the field for the outer trajectories (1250 to 1400) to be higher than for the inner ones (1150 to 1000), as seen in figure 2.11. The asymmetry reflects on the field flatness (see figure 2.13). The magnetic flux density through each of the return yokes has to be equalized in order to achieve a balanced field flatness. We propose two different methods of equalization: in the first method the balance is achieved by controlling the magnetic flux on the inner and outer return yokes alone, while in the second method the balance is achieved by adjusting the flux in the inner and outer return yokes in relation to the pole surface.

In the first method the equalization is studied by looking at both the

Figure 3.17: Rendering of the reference surface with the first equalization method applied; the blue circle indicates the air channel carved in the outer return yoke steel in order to achieve balanced flux.

horizontal and vertical surface areas of the return yoke as indicated in figure 3.17.

Three configurations are considered for the first method. The first configuration has the same horizontal surface area for both the inner and outer return yoke. The second configuration has the return yoke horizontal surface same as the vertical one but different between inner and outer return yoke. The third configuration has all the surfaces (horizontal and vertical) equal for both return yokes. This is accomplished by carving the steel creating an air channel along the return outer return yoke (see blue circle in figure 3.17). The height of the carved channel is introduced as a parameter so the various surface areas can be calculated using the parametrized model of the magnet (see section 2.3).

Comparison of the field flatness between the three configurations is shown in figure 3.18. The result seems to indicate that the equality of horizontal surface areas (inner and outer) is more relevant while the vertical is used to control the steel saturation for the respective return yoke.

The last configuration yields the best result; the top magnetic field profile for this case is shown in figure 3.19 to be compared with figure 2.11.
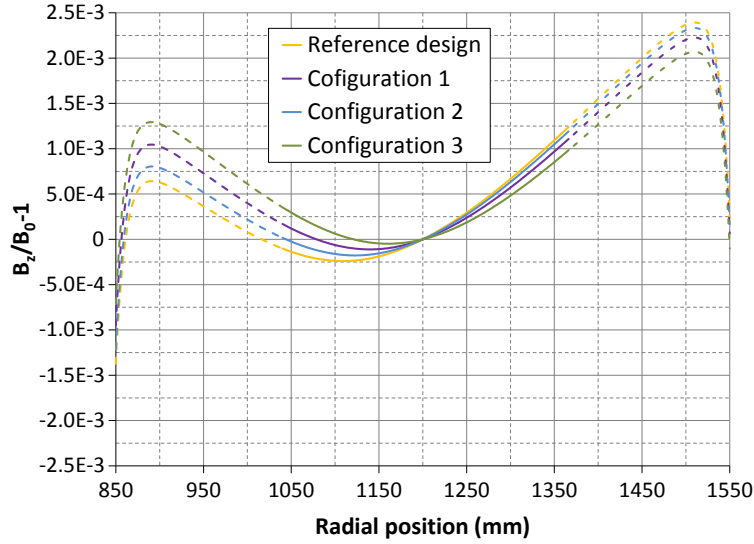
Figure 3.18: First equalization method configurations comparison.
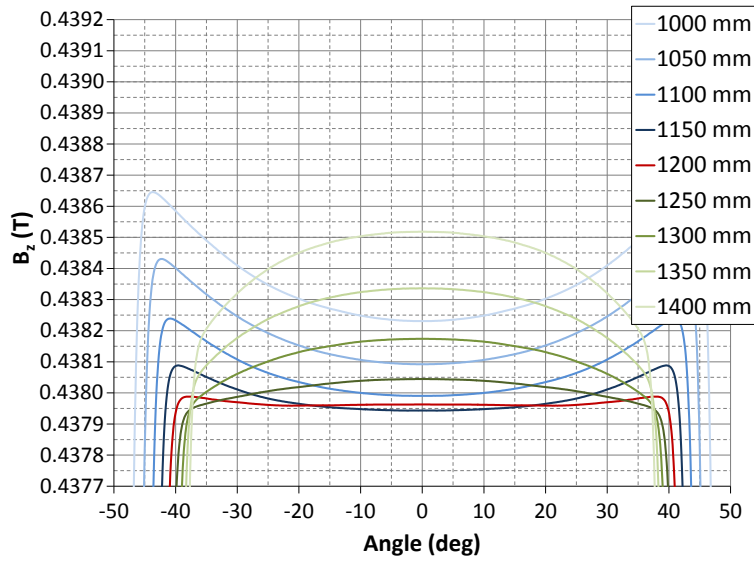
Figure 3.19: Equalized geometry (HRS-120-16C3: first method, configuration 3) B_z vertical magnetic field component magnified near the peak. The field is symmetric with respect to 0 degree. This figure to be compared with figure 2.11.

The field distribution in the steel before and after equalization with the first method (third configuration) is shown in figure 3.20.

In the second method, we consider only the horizontal surfaces of the return yokes but in relation to the pole face surface (no air channel for vertical compensation). On an historical note related to this project, this second method comes later in time and for this reason many of the geometries in chapter 4 still employ the first method (third configuration) of equalization.

The pole surface is considered to be of two portions with the divider being the radius of curvature where the magnetic flux is "naturally split" toward the inner and outer return yokes. This splitting radius lays on the tip of the blue cone (no magnetic flux) as represented in figure 3.21 in which case the splitting radius is 1140 mm. Our approach is unique to the extent that the split point is not just taken as the mid point of the pole, that in our case correspond to the 1200 mm radius.

The equalization is achieved by making the ratio of the inner return yoke horizontal surface to the pole inner surface equal to the ratio of the outer counterparts. For this particular geometry (figure 3.21) the ratio is
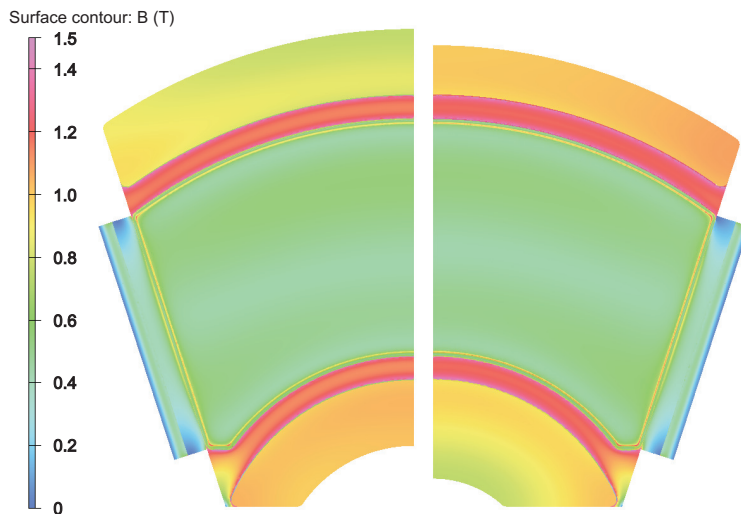
Figure 3.20: Magnetic flux density in the steel before (left) and after (right) equalization with the first method.
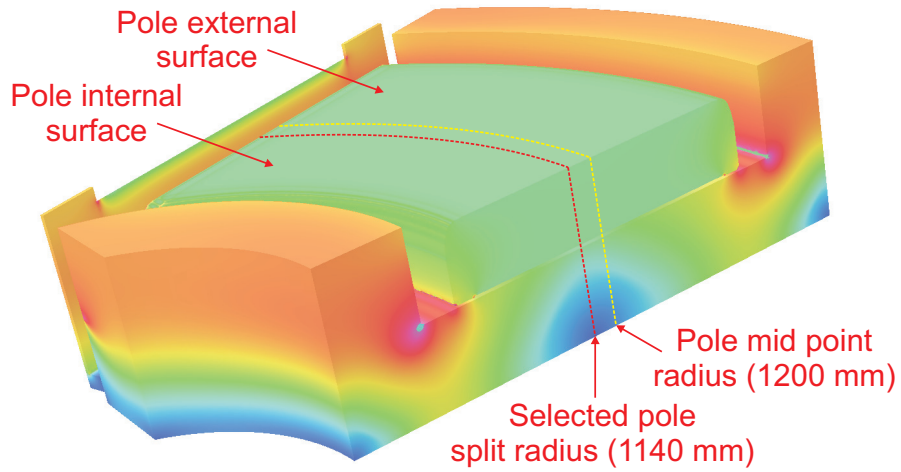
Figure 3.21: Second equalization method: the splitting radius (red) is 1140 mm while the symmetry one (yellow) is 1200 mm.

about 44%. A lower ratio would increase the saturation level of the return yokes while a higher one would make the magnet unnecessarily larger. A comparison of the saturation level before and after applying the second method is represented in figure 3.22.
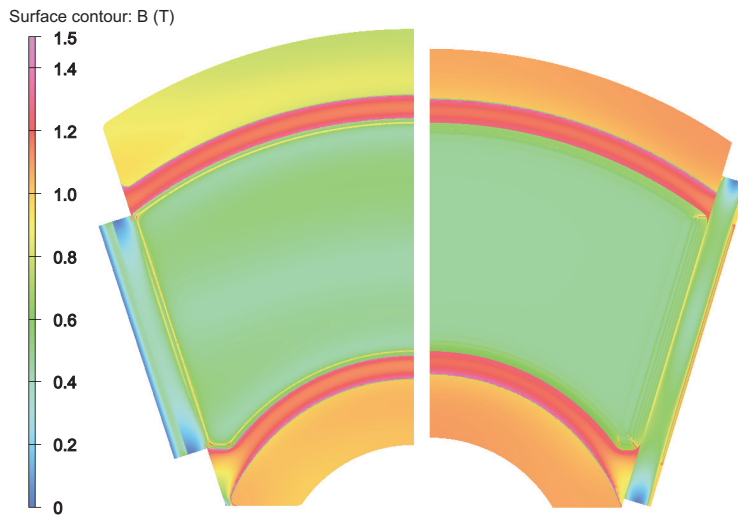
Figure 3.22: Magnetic flux density in the steel before (left) and after (right) equalization with the second method.

Our approach of using the split radius rather than the symmetry one produces also a better field flatness as represented in figure 3.23.

The second method returns a far better result and it is also easier to implement from a mechanical point of view.
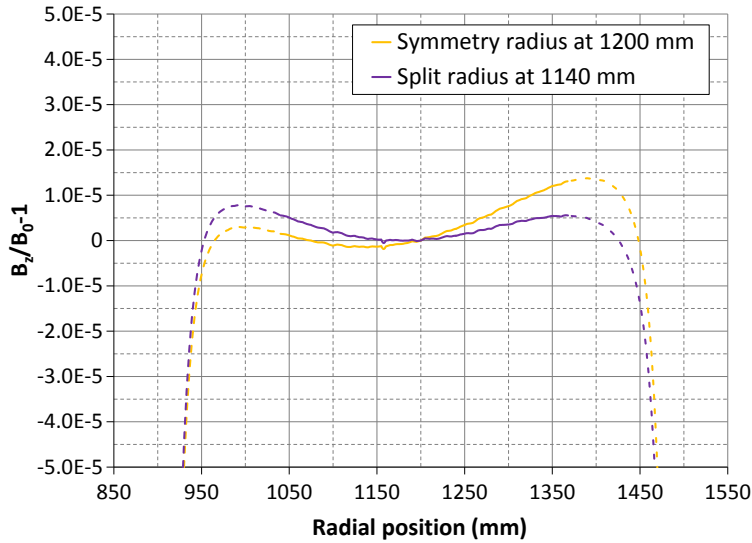
Figure 3.23: Field flatness comparison between the split and symmetry radius cases (second method). Note the apparently sudden improvement with respect to figure 3.18; as we wrote in the text, this second method was developed later in time on a geometry with a higher level of optimization.

Chapter 4

Optimization on the Straight Edge Model

All the results obtained in the previous chapter are combined into a new geometry that we identify as nominal (HRS-120-19C1). This geometry is not yet the final configuration since it still has straight entrance and exit edges; this feature is going to be added as the last step after reaching the optimization of the nominal.

4.1 Nominal geometry

The main dimensions of this new geometry are listed in table 4.1. The entrance and exit edge angles are relative to the hard edge case. A rendering of the nominal geometry is represented in figure 4.1.

Table 4.1: Nominal geometry main parameters.

Geometric parameter	Dimension
Bending radius	1200 mm
Bending angle	90 degrees
Entrance and exit hard edge angle	27 degrees
Pole gap	70 mm
Pole height	180 mm
Pole base height	229.5 mm
Pole width	676 mm
Equalizing channel height	44 mm
Coil	$69 \times 69 \, \text{mm}^2$
Coil to steel vertical separation	8.5 mm
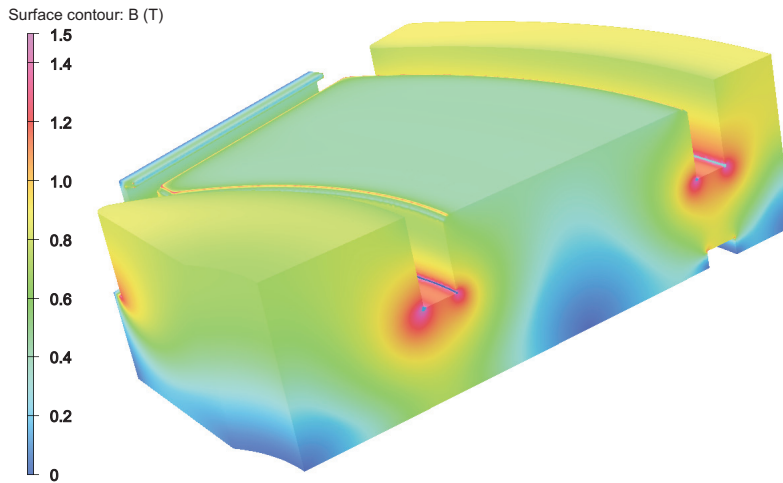
Figure 4.1: Nominal geometry rendering.

The parameter choice takes also into consideration the production cost of the magnet by limiting some specific dimensions; the pole base height is an example of such a dimension. The nominal geometry return yoke flux is balanced with the third configuration of the first equalization method (see equalizing channel height in table 4.1). The coil section is also unchanged but the vertical position above the coil channel is updated to reflect a more realistic mechanical layout.

The vertical field component (top) is represented in figure 4.2. Compared with the reference geometry (figure 2.11), the field drops off the edges for both the inner and outer geometric trajectories thanks to a more uniform field distribution over the pole surface (see figure 4.1). Still, the field drop is more pronounced in the outer trajectories; this reflects, as for the reference geometry, on the integral flatness represented in figure 4.5 despite the field flatness.

This field flatness profile of the nominal geometry is shown in figure 4.3. This is an improvement with respect to the reference geometry (see figure 2.13) but it is still one order of magnitude too high.

The effective fringe field, although still not aligned with the hard edge case, presents an angle correct to $1 \cdot 10^{-3}$ degrees.
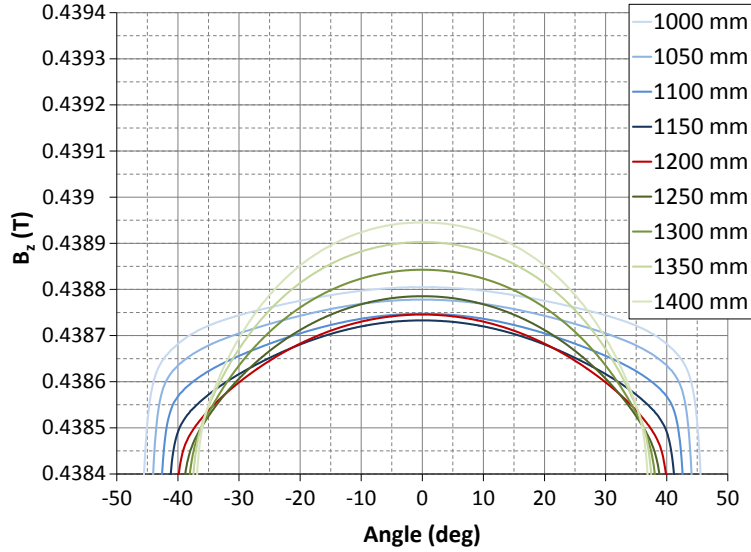
Figure 4.2: Nominal geometry B_z vertical magnetic field component, magnified near the peak, to show flatness. The field is symmetric with respect to 0 degree.
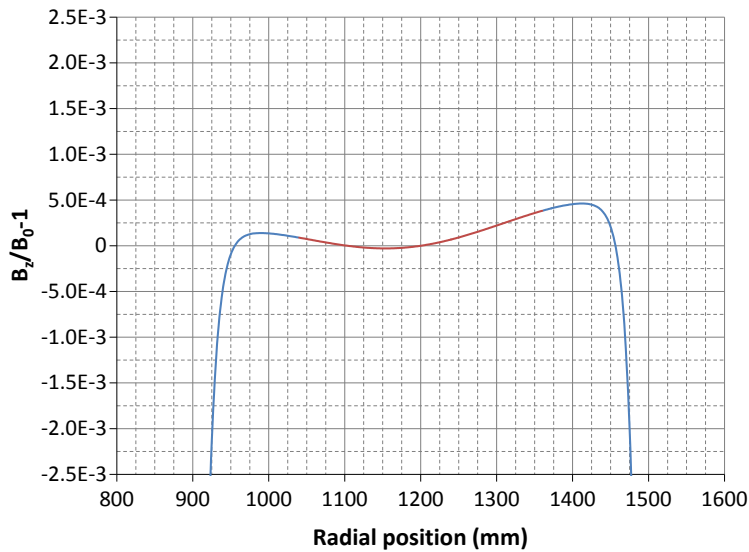
Figure 4.3: Nominal geometry field flatness: the red portion of the curve represents the flatness within the good field region (±160 mm around the reference geometric trajectory $\rho = 1200$ mm).
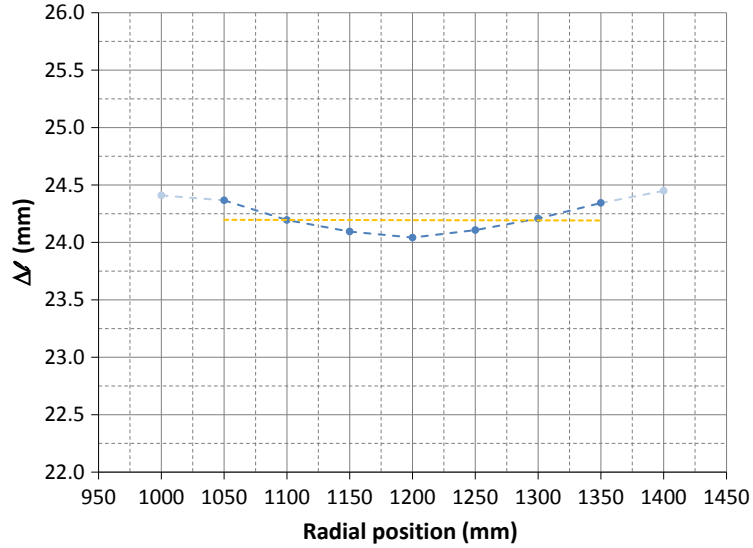
Figure 4.4: Nominal geometry effective field edge location with respect to the relative hard edge case: the linear interpolation (yellow dashed line) between 1050 mm and 1350 mm gives indications about position and angle.
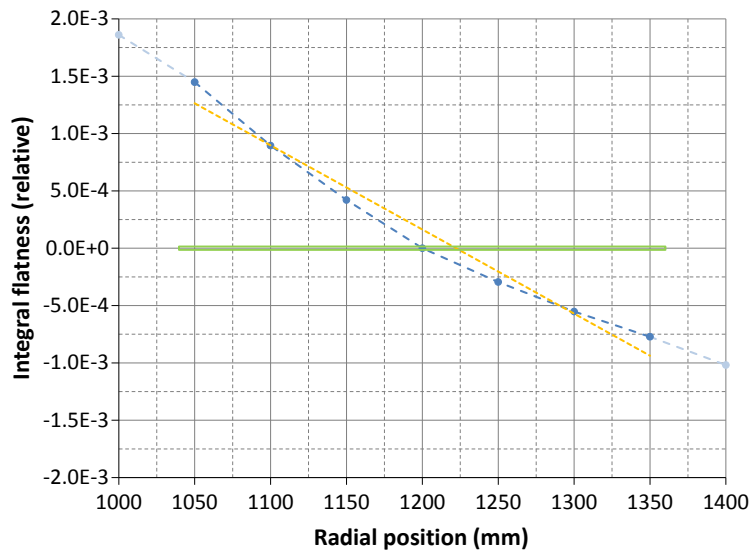
Figure 4.5: Nominal geometry integral flatness with respect to the relative hard edge case: the yellow dashed line is a linear interpolation between 1050 mm and 1350 mm. The green box ($2.5 \cdot 10^{-5}$ high) represents the flatness requirement in the good field region.

The integral flatness (figure 4.5) is an improvement from the one of the reference geometry (figure 2.16) if compared the linear interpolations (yellow dotted line) of the two cases, but it is again far from meeting the requirements (green box).

4.2 Sector Rogowski profile

In this section we are going to introduce the Rogowski profile [43]. The original work by Rogowski [44][17] was related to breakdown of the electrostatic field in gases for high voltage plates; the same idea can be applied to the magnetostatic field since it also satisfies Laplace equation for the magnetic potential. In the electrostatic case the goal is to avoid breakdown, while in the magnetic one it is to avoid saturation of the steel.

This Rogowski profile is a more complicated design of the profile of the edges of the magnet poles compared to what we used so far, a simple 45 degrees chamfer at the edge (see figure 3.9 for example). Both these options are used to reduce the saturation of the pole edges (rather than having a 90 degrees corner); the Rogowski profile though is more effective with respect to the chamfer option. Avoiding saturation is necessary in our case in order to satisfy the requirement of field reproducibility at different current excitation level (see section 2.2).

The Rogowski theoretical profile is a function of the gap g and it is represented by the following equation:

$$f(x) = g \left(\frac{1}{2} + \frac{e^{\frac{\pi x}{g} - 1}}{\pi} \right) \tag{4.1}$$

where, in our case, x is a transverse direction parallel to the pole surface plane and $f(x)$ perpendicular to the same.

Even though the theoretical Rogowski is a machinable profile, it is easier to model, simulate and specify a polygonal approximation[18]. A four straight

---

[17]The original paper by Rogownski [44] is in German.
[18]A polygonal approximation would be easier to machine only for a 5-axis CNC machine.
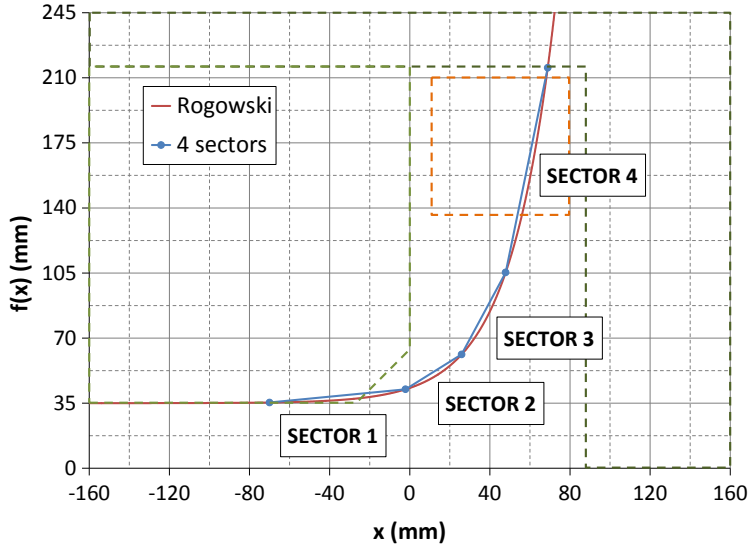
Figure 4.6: Rogowski profile approximated with four straight sectors: the dotted light green line represents the pole, the dark green represents the pole base and return yoke, the dotted orange line represents the coil of the nominal geometry. The profile has to be moved inward to accommodate the coil while avoiding an increase of the magnet size.

sectors approximation is represented in figure 4.6 compared to the theoretical profile; in this graph $x = 0$ represents the magnet middle plane while $y = 0$ corresponds to the side of the initial pole (45 degrees chamfer). Each sector coordinates are calculated such that the sector distance from the theoretical curve is limited by a defined maximum. In addition the coordinates of all sector are constrained such that the first sectors starts one gap (70 mm) inward from the edge of the original pole while the last sector ends at the bottom of the pole (180 mm high in this case).

The four sectors Rogowski that we just defined can not be directly applied as constructed to the nominal geometry since the the coil would not fit as illustrated in figure 4.6. In order to avoid increasing the size of the magnet, the simplest solution is to move the same profile inward. This solution does not change the performance of the Rogowski but it does reduce the pole effective width; this issue is going to be discussed further at the

end of this section.

In the longitudinal direction, along the geometrical trajectories, we employ the same Rogowski without elongating the pole for the reason we are going to explain at the end of this section; this is done simply by matching the end point of the fourth sector to the edge of the base of the initial pole. The geometry with the four sector Rogowski profile is represented in figure 4.7 where the pole width is increased to 800 mm.
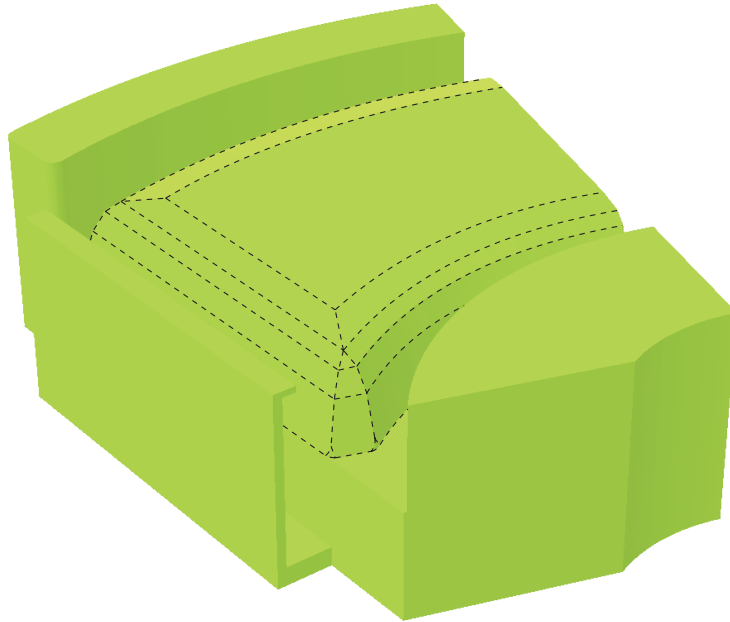
Figure 4.7: Geometry with four sectors Rogowski profile (dashed lines).

In order to evaluate the effectiveness we compare both the nominal case and the Rogowski geometry at the two extreme excitation levels necessary to bend the maximum and minimum rigidity (see section 2.2). At the lowest excitation the produced field is around 0.087 T; this value is adequate to bend a particle of mass 10 [19].

For these two cases we plot the longitudinal field profile along the geometric trajectories relative to the reference one; we are going to identify this

---

[19]This is a slightly stricter requirement with respect to the one specified in section 2.2, but it is due to the approximation of the current scaling input in OPERA.

quantity as longitudinal field flatness defined by the following:

$$LFF = \frac{B_z(s)}{B_{z,1200}(s)} - 1 \qquad (4.2)$$

where we already defined s as the path length along a beam trajectory; notice that for the reference trajectory the longitudinal field flatness is zero. The relative field is plotted as a function of the angle, rather than s[20], where zero degree corresponds to the center of the magnet.

Figure 4.8 represents the longitudinal field flatness of the nominal geometry for maximum (solid line) and minimum (dashed line) rigidity; a close view of the same around the longitudinal edges of the dipole is shown in figure 4.9. The longitudinal field flatness for the geometry with the four sectors Rgowski profile for the two extreme rigidities is represented instead in figure 4.10 and again in close view in figure 4.11.
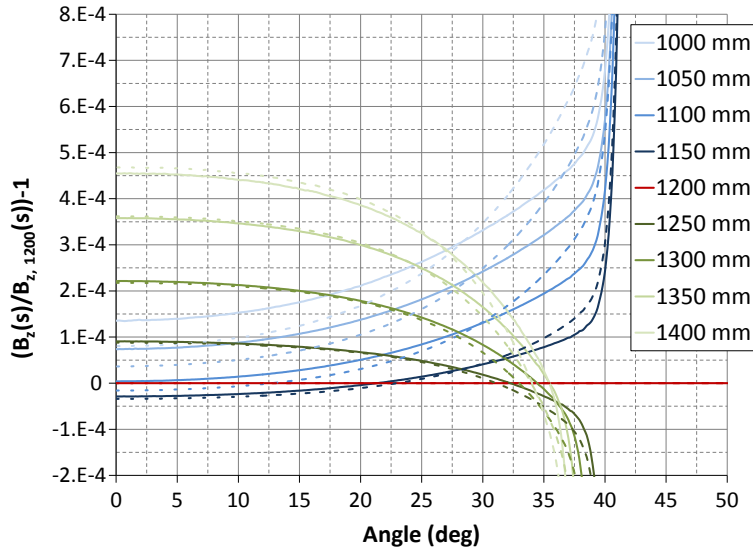
Figure 4.8: Longitudinal field flatness of the nominal geometry for maximum (solid line) and minimum (dashed line) rigidity. A close view is represented in the following figure 4.9.

---

[20]As far as the geometric trajectories inside the dipole $s = \rho \cdot$ angle
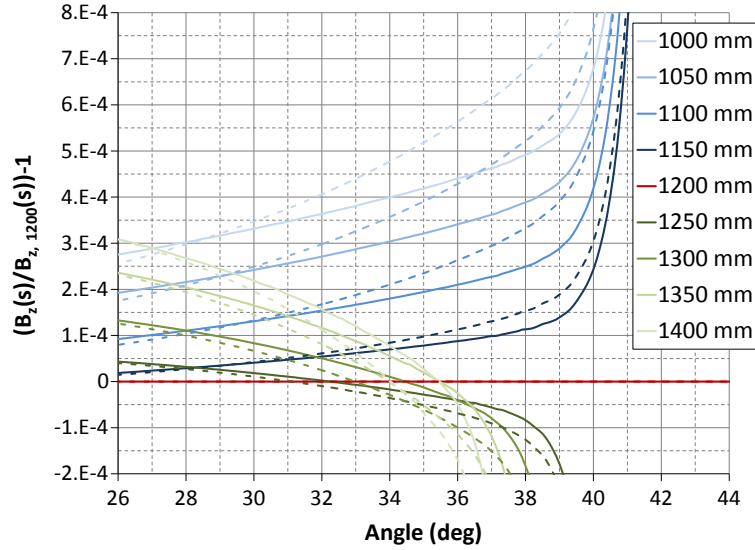
Figure 4.9: Close view of the longitudinal field flatness of the nominal geometry for maximum (solid line) and minimum (dashed line) rigidity around the longitudinal edge of the dipole.
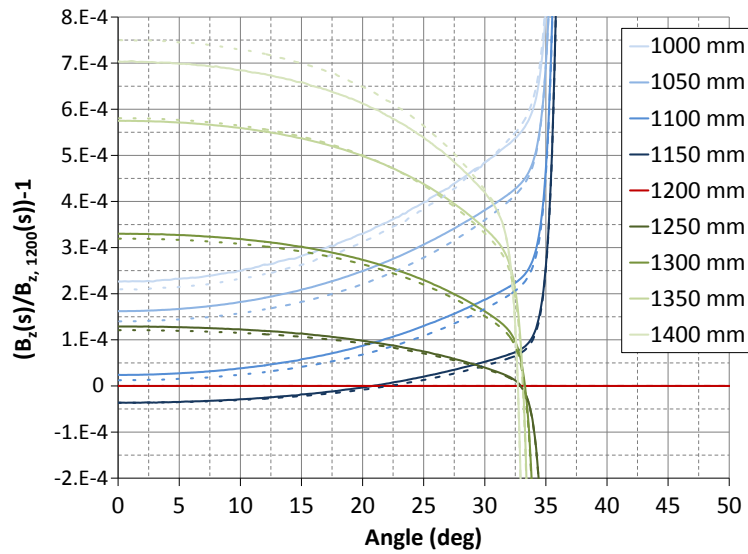
Figure 4.10: Longitudinal field flatness of the four sectors Rogowski geometry (HRS-120-19C8) for maximum (solid line) and minimum (dashed line) rigidity. A close view is represented in the following figure 4.11.
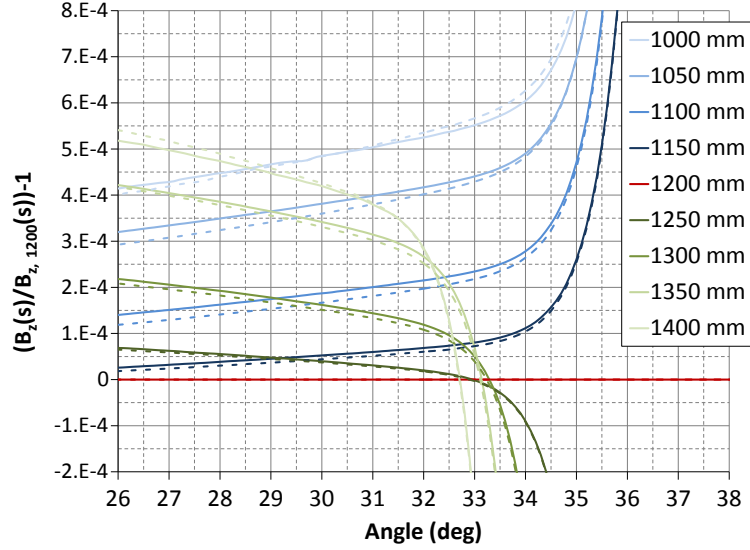
Figure 4.11: Close view of the longitudinal field flatness of the four sectors Rogowski geometry (HRS-120-19C8) for maximum (solid line) and minimum (dashed line) rigidity around the longitudinal edge of the dipole.

Based on the results, the simple chamfer of the nominal geometry is not enough to guarantee field reproducibility in the low 10^{-5} range; for example at 37.5 degrees the 1250 mm geometric trajectory presents a relative change of $4 \cdot 10^{-5}$ while for the 1300 mm the change is around $1 \cdot 10^{-4}$. By comparison the Rogowski geometry with four sectors has a reproducibility of the edge field that is within $2 \cdot 10^{-5}$; this means that the optics behavior of the separator is fairly linear between the two extreme cases of current excitation.

The different behaviors of the magnet edge for the nominal geometry can also be seen qualitatively in the saturation of the steel as represented in figure 4.12 (top); in the same picture the Rogowski case (bottom) shows a more uniform field distribution on the edges.

The Rogowski profile has a more pronounced edge field effect with respect to the simple 45 degrees chamfer as seen in figure 4.10. In the transverse dimension this implies that for the same mechanical pole width we have a smaller effective width in the Rogowski case and therefore a larger pole is in

80

Surface contour: B (T)
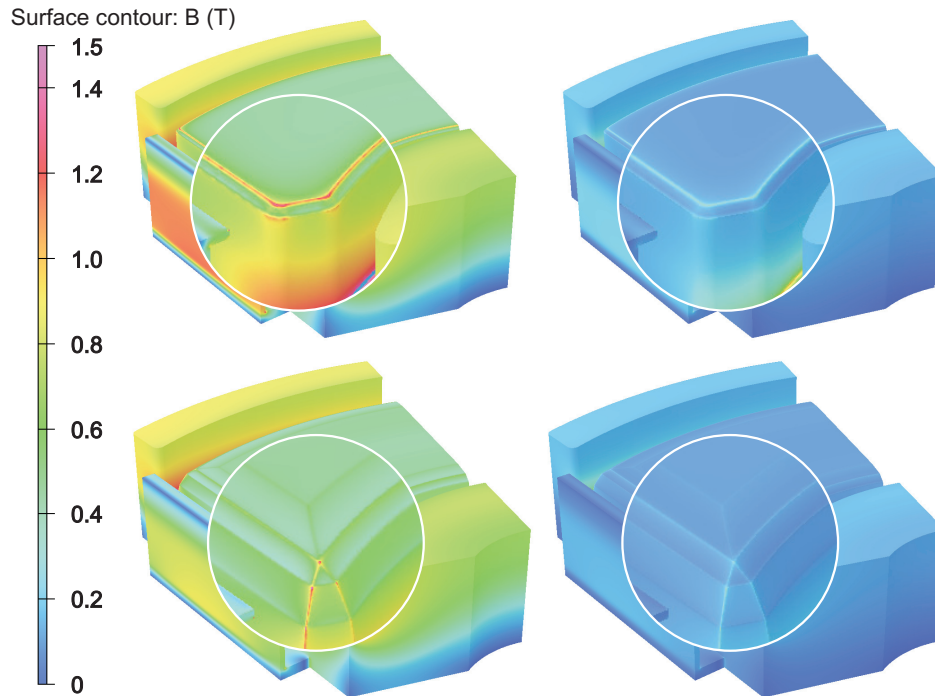
Figure 4.12: Magnetic flux density for the nominal (top) and four sectors Rogowski (bottom) geometries at current excitation relative to the maximum (left) and minimum (right) beam rigidity.

general required. At the same time though this edge effect tends to improve the field flatness for our mode of operation.

The same is true in the longitudinal case where the effective field edge moves toward the inside because of the more rapid fall off of the field. Since we started with an effective field outward with respect to the hard edge case (see figure 4.4), we applied the four sectors Rogowski profile without elongating the pole in order to achieve such a goal. In fact applying the original Rogowski (in the four sectors configuration) leads to the opposite situation where the effective field edge is inward with respect to the hard edge case. The obvious solution in order to match the hard edge case would be to elongate the pole. We propose instead an alternative that implements a scaled Rogowski to maintain optical property at different excitations and

at the same time to control the location of the effective field edges without elongating the pole. Details of the implemented profile are given in section 5.1.

4.3 Purcell-like filter

A Purcell filter[21] is a region within the magnet with relative permeability equal to one (air for example) that improves the field uniformity in the pole gap. The simplest Purcell filter is a uniform separation between the pole and the pole base, as we will show in our first attempt, but other more elaborate configurations [45] can be implemented trying to manipulate the field flatness. Using as base the nominal geometry (no Rogowski profile) we have developed different original configurations starting from a conventional Purcell filter.

The conventional Purcell filter as applied to the nominal geometry is represented in figure 4.13. The pole is completely separated from the pole base with a uniform air gap.

The result of the calculation in terms of field flatness, plotted in figure 4.14, shows that this configuration of the filter cancels the low excita-
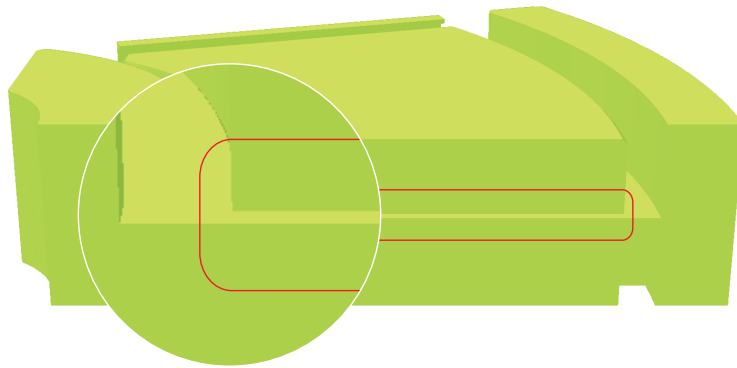
Figure 4.13: Rendering of the nominal geometry with the full Purcell filter (HRS-120-20C17): the air gap between the pole and pole base is highlighted by the red loop.

---

[21]Patent US2962636 A by inventor Edward M. Purcell - November 29, 1960.
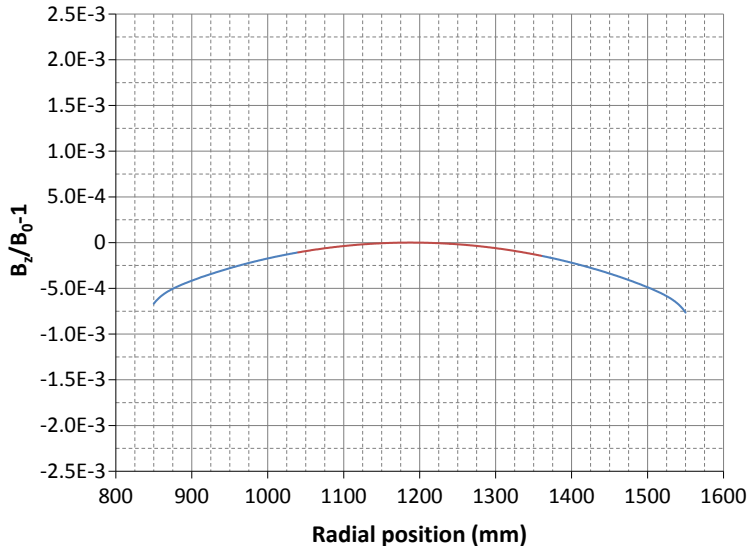
Figure 4.14: Field flatness of the geometry with the full Purcell filter.

tion effect seen in section 3.1 without saturation of the pole. This solution though requires a wider pole to improve the field flatness. The results shown in figure 4.14 are obtained with a 900 mm pole width; despite such a large pole the flatness is still $1.5 \cdot 10^{-4}$, one order of magnitude too high.

In an attempt to increase the field for the inner and outer trajectories, we add 38 mm wide legs on both sides of the bottom of the pole. The legs rest on the pole base making magnetic contact. The idea is to guide the magnetic flux preferentially on the side edges by reducing the local reluctance (no air gap). This first proposal is represented in figure 4.15: partial Purcell filter.

The result is such that these legs increase the inner and outer fields too much as plotted in figure 4.16, prompting the need to reduce the leg width.

On the other hand, the steel of these legs already saturates to a value over 2.2 T since, as expected, the magnetic flux goes preferentially through them. A reduction in width is just going to increase the saturation level.

The next configuration takes the opposite approach; instead of resetting the nominal geometry field flatness starting from the full Purcell filter, we attempt to control it by adding a local small Purcell filter. The idea in this

Figure 4.15: Rendering of the nominal geometry with the partial Purcell filter (HRS-120-20C2): the partial air gap between the pole and pole base is highlighted by the red loop.
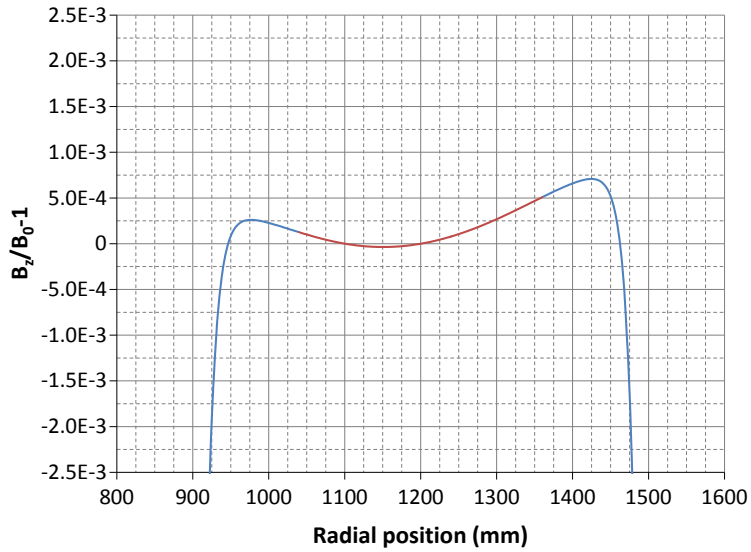
Figure 4.16: Field flatness of the geometry with the partial Purcell filter.

case is to reduce the field for the inner and outer trajectories by increasing the reluctance on the side edges of the pole. The second proposed configuration is shown in figure 4.17: outboard Purcell filter. The pole has two
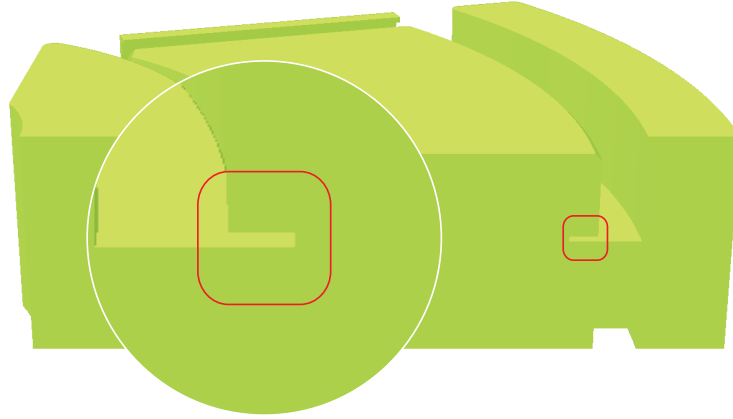
Figure 4.17: Rendering of the nominal geometry with the outboard Purcell filter (HRS-120-20C7): the air slots at the bottom of the pole are highlighted by the red loops.

rectangular slots carved on the bottom sides of the pole.

This configuration is successful in bringing the field flatness in the 10^{-5} range as shown in figure 4.18 but the field starts dropping within the good field region.
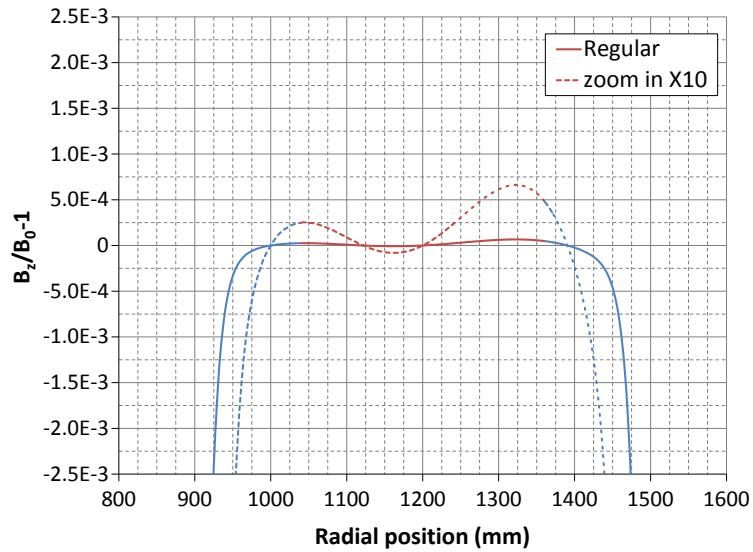
Figure 4.18: Field flatness of the geometry with the outboard Purcell filter; the dashed curve is $\times 10$ magnified.

The narrower base of the pole (due to the outboard filter) translates into a reduced effective pole width at the gap level. As a reference the field flatness crosses zero at $\rho = 1000\,\text{mm}$ and $\rho = 1390\,\text{mm}$ compared with in the previous configuration where this occurs at $\rho = 945\,\text{mm}$ and $\rho = 1460\,\text{mm}$ for the same pole width. Making the pole wider is not going to improve the flatness since the field at the center would decrease as described in section 3.3 (see figure 3.15).

Starting from this last configuration we want to try to restore the effective pole width and reduce the field at the edges of the good field region. The two rectangular slots are moved inside the pole generating two air windows (similar to what is outlined in citation [45]). The third proposed configuration is shown in figure 4.19: windows Purcell filter.

The position and dimensions are optimized to control the strength of different fields at different geometric trajectories. The result of this configuration is represented in figure 4.20. The effective pole width slightly increased as expected with the field flatness crossing zero at $\rho = 985\,\text{mm}$ and $\rho = 1405\,\text{mm}$ but the field did not improve. Moreover the section of steel on the outer side of the windows are at $1.5\,\text{T}$, close to saturation. Even
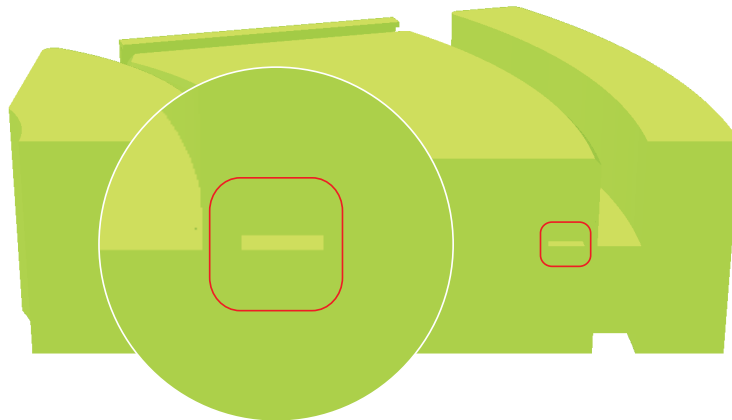
Figure 4.19: Rendering of the nominal geometry with the windows Purcell filter (HRS-120-20C15): the air windows in the pole are highlighted by the red loop.
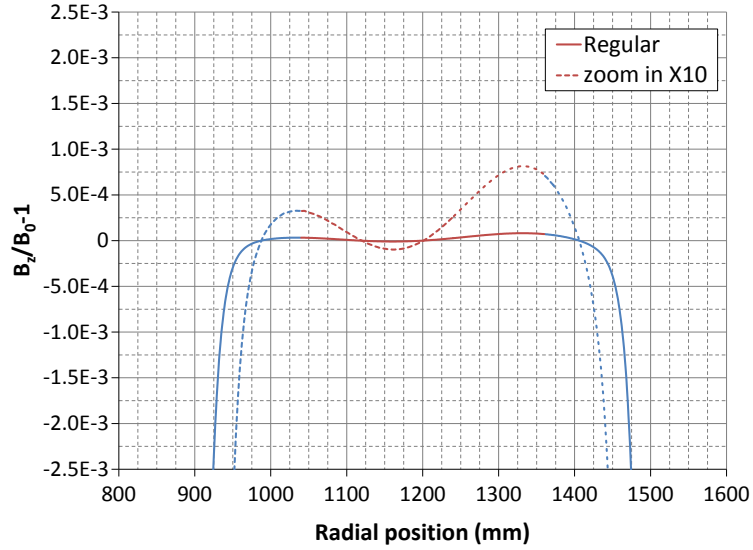
Figure 4.20: Field flatness of the geometry with the outboard Purcell filter; the dashed curve is ×10 magnified.

though it is possible to control the fields to some extent, this configuration is not suited to meet the field flatness requirements.

The fourth configuration reconsiders the fully detached filter in order
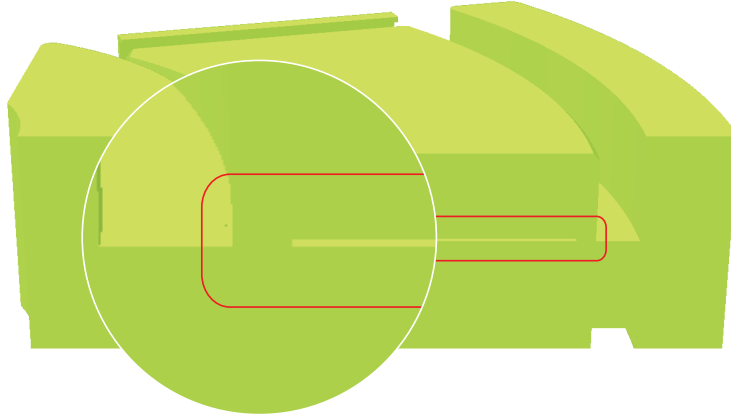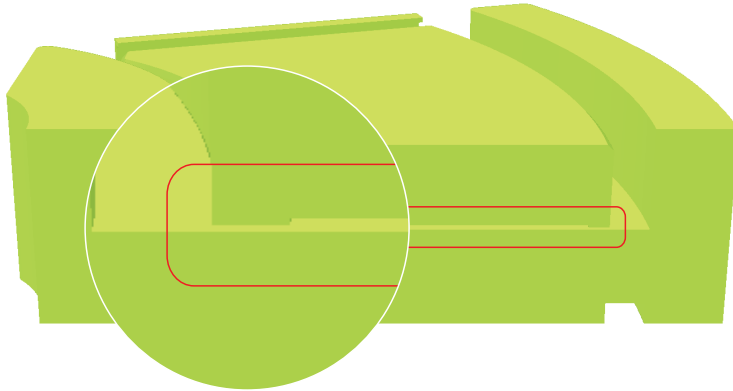

Figure 4.21: Rendering of the nominal geometry with the detached partial Purcell filter (HRS-120-20C20): the air gap between the pole and pole base is highlighted by the red loop.

to avoid saturation (as in the last two cases) while increasing the inner and outer fields using the second configuration approach. The result is the geometry shown in figure 4.21: detached partial Purcell filter.

The geometry of the pole is like the partial Purcell but with the pole now detached from the pole base. This last configuration has an 800 mm wide pole, narrower with respect to the full Purcell. The legs create a smaller reluctance by reducing the air gap from the pole base but they don't saturate since there is no magnetic contact and therefore no high flux. The leg dimension can be individually set in order to optimize independently the inner and outer trajectories. The field flatness for the detached partial Purcell filter is plotted in figure 4.22; this configuration has the capability of meeting field flatness requirement (better than $2.5 \cdot 10^{-5}$).
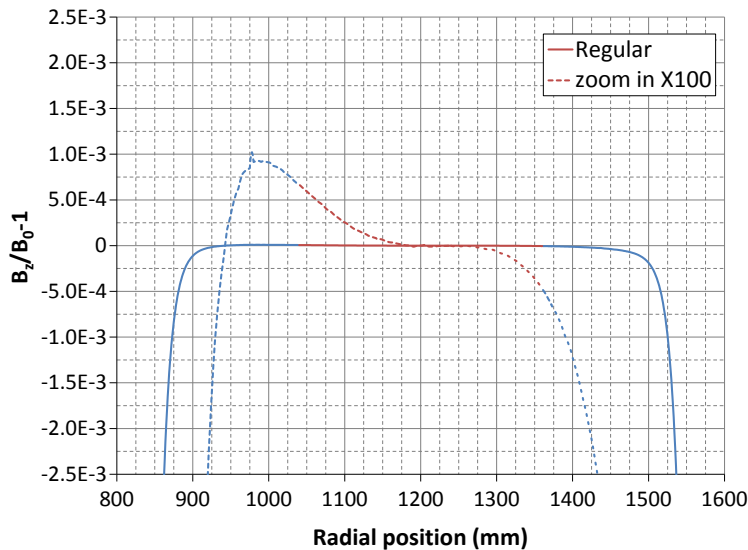
Figure 4.22: Field flatness of the geometry with the detached partial Purcell filter; the dashed curve is $\times 100$ magnified.

4.4   Field clamp

It is important to control the magnetic field fall off at the entry and exit edges of the pole. In section 4.2 we learned how to control the edge field at

different levels of excitation, but we need also to control the reproducibility of the field independently from the environment external to the magnet. In other terms, we need to assure that the magnetic field leaving the pole, fringe field, closes along a predictable path. Longitudinally, along the geometric trajectories, this is accomplished by the use of steel structures outside the current carrying coil; these structures, located at the entrance and exit of the magnet, top and bottom with respect to the middle plane, are called field clamps. Transversely such structures are the return yoke that guarantee a closed path for the magnetic flux.

Each pair of field clamps (top and bottom) can be seen as a longitudinal return yoke with an aperture that allows the beam to go through; this means that the field inside this aperture has the opposite direction of the field inside the magnet gap, as can be seen in figure 4.26. Figure 4.23 shows the bottom entrance field clamp (not optimized) for the nominal geometry.

The the design of the field clamps is optimized based on the following criteria:
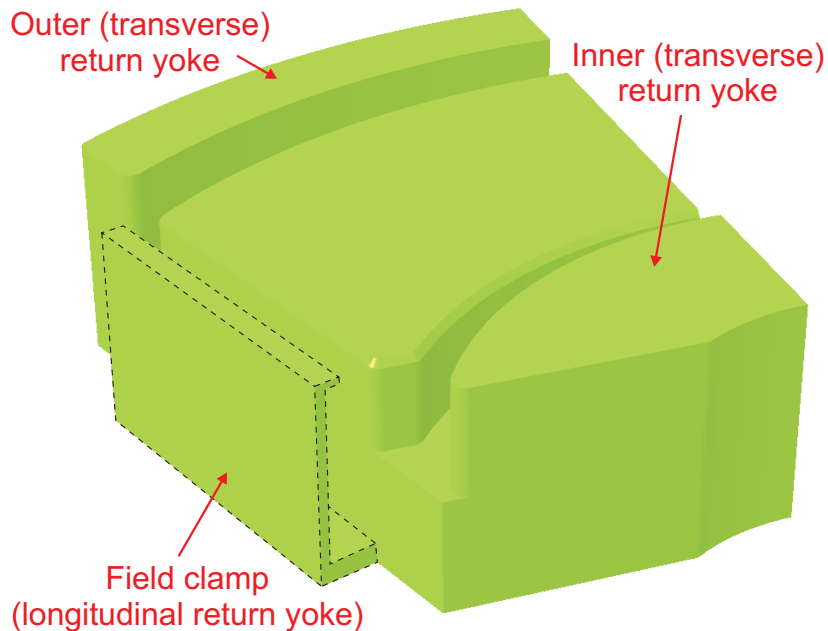
Figure 4.23: Nominal geometry bottom entrance field clamp (dashed line).

- The fringe field tail (circa zero field) distance from the magnet should be minimized: this is to avoid that the field profile is going to be affected by other beam line or surrounding steel elements.

- The field profile should minimize the first derivative of the field (sharp change in the profile): high first derivative contributes to high order aberration in the beam dynamics.

- Saturation of the field clamp should be avoided (magnetic flux to be less than 1.5 T): this is in order to guarantee that the field clamp maintains the same behavior at different excitation levels.

Different configurations have been developed starting from the standard one used in the nominal geometry. In order to evaluate a configuration, the vertical field component B_z along the reference geometrical trajectory ($\rho = 1200\,\text{mm}$) is plotted as a function of the distance from the entrance (or exit) of the theoretical hard edge case as seen in figure 4.24; the outer
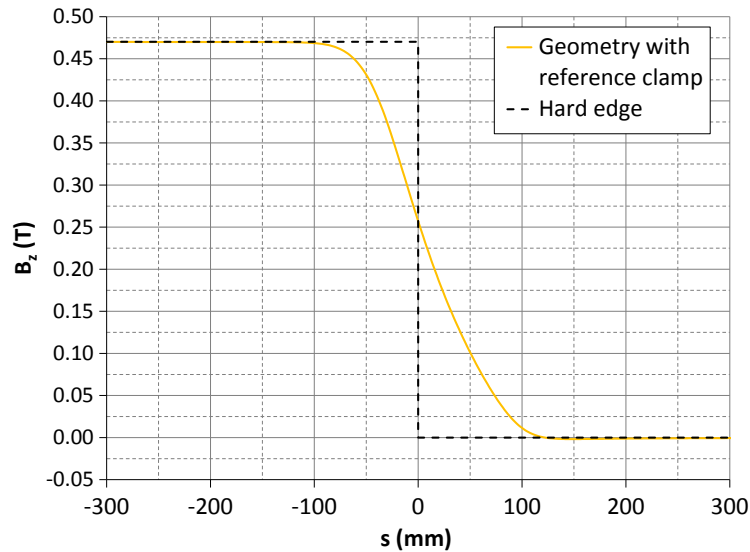
Figure 4.24: Magnetic field of the geometry with reference clamp versus the theoretical hard edge case plotted as a function of s (path length along a beam trajectory). The outer mechanical edge of the clamp is at $s = 106\,\text{mm}$.

(with respect to the magnet center) mechanical edge of the field clamp sits at 120 mm.

The field fall off resulting from the different configurations is plotted in figure 4.26, while the configurations are summarized here:

1. No clamp: this case is included in the calculations for reference. In this case the field falls off with the minimum variation of the first derivative but it extends the most beyond the edge of the magnet. At 400 mm from the edge where other beam line components will reside, the field is still 18 G.

2. 70/86 mm: these two numbers refer to the clamp aperture (70 mm, same as the pole gap) and distance from the pole edge (86 mm). In this case the clamp has a simple L shape, as in figure 4.25; we are going to identify this as reference clamp. The fall off relative to this configuration has a significant overshoot on the negative side and a sharp change in the field profile. We already mentioned that the field inside the clamp aperture is opposite to the field in the gap, so it is expected that the former counteracts the latter, but in this case the field produced by the clamp is too strong.
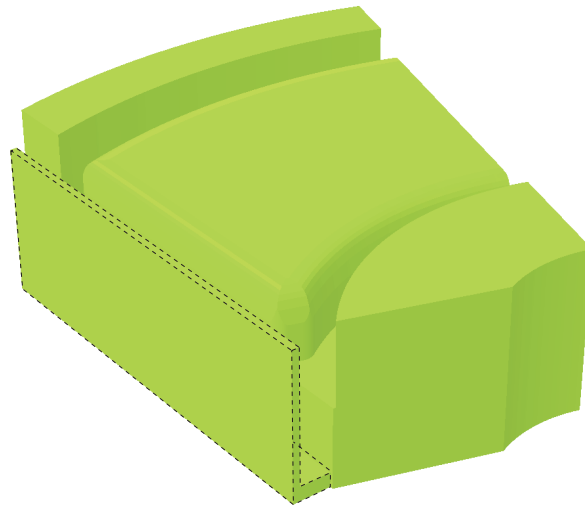
Figure 4.25: Simple L shape reference clamp.
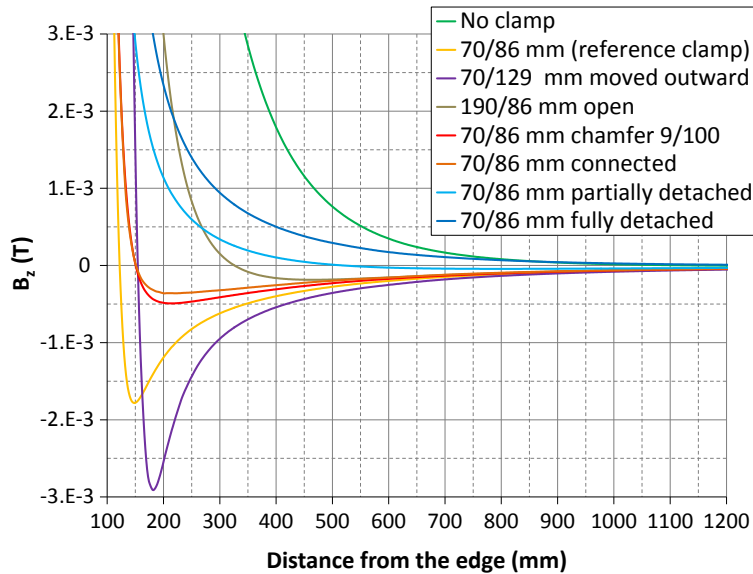
Figure 4.26: Magnification of the fringe field profiles of the different field clamp configurations.

3. $\underline{70/129\,\text{mm moved outward}}$: more to the fact that field clamp is acting as a return yoke with opposite field, we consider a configuration where the clamp distance is increased (129 mm) while maintaining the same aperture; since we didn't change the geometry, the clamp has the same strength but applied in a weaker (farther away) region. The result is a stronger overshoot with respect to the previous configuration.

4. $\underline{190/86\,\text{mm open}}$: in order to weaken the clamp we increase the aperture to 190 mm while preserving the distance (86 mm). The result this time is as expected with a smoother fall off, but the fringe field fringe field is shifted outward.

5. $\underline{70/86\,\text{mm chamfer 9/100}}$: a better approach to reduce the strength of the field clamp is applying a chamfer on the edge. This effectively reduces the efficiency of the field clamp while maintaining the field fall off close to the clamp.

6. $\underline{70/86\,\text{mm connected}}$: an additional reduction of the field strength can

be obtained by connecting the clamp pair (top and bottom) in order to create a low reluctance path for the magnetic flux. The result is a weaker field through the field clamp aperture.

7. 70/86 mm partially detached: a further reduction can be achieved by weakening, from a magnetic point of view, the entire clamp. We insert an opening (filter like) at the base of the clamp where it is connected to the pole base. This configuration generates a smooth fringe field while maintaining it close to the magnet.

8. 70/86 mm fully detached: as a last check we investigated the option of a clamp non magnetically connected to the dipole. This results in the fringe field moving away from the magnet.

The final design for the straight geometry is represented in figure 4.27 and it corresponds to the seventh configuration. The clamp has an aperture equal to the pole gap and a minimum distance from the edge that allows for the coil accommodation. The edge has a chamfer and the lower and upper clamp are connected. Finally the clamp has filter-like windows where it attaches to the pole base of the magnet.
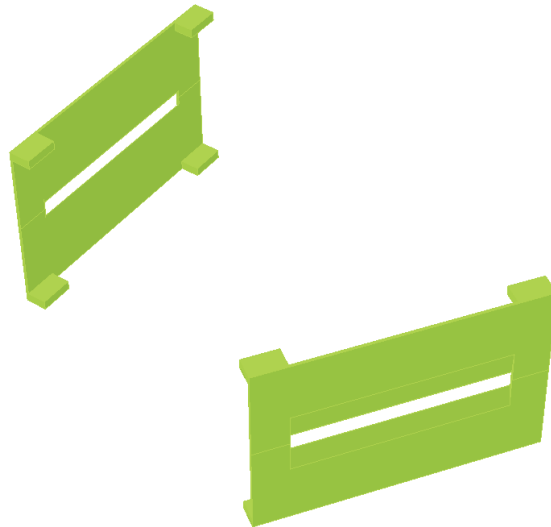
Figure 4.27: Optimized field clamp for the straight edge geometry.

Chapter 5

Final Design

The findings presented in the previous three chapters converge to an optimized solution of the straight edge magnetic dipole model. This serves as the basis to design the final geometry for the case with curved entrance and exit edges. A curved edge, as we are going to see in section 5.3, is the way to implement a second order correction in the beam dynamics [1].

5.1   Optimized straight edge model

In this section we present the final design of the straight edge model. Figure 5.1 is a rendering of the optimized straight edge geometry (HRS-120-21C57).
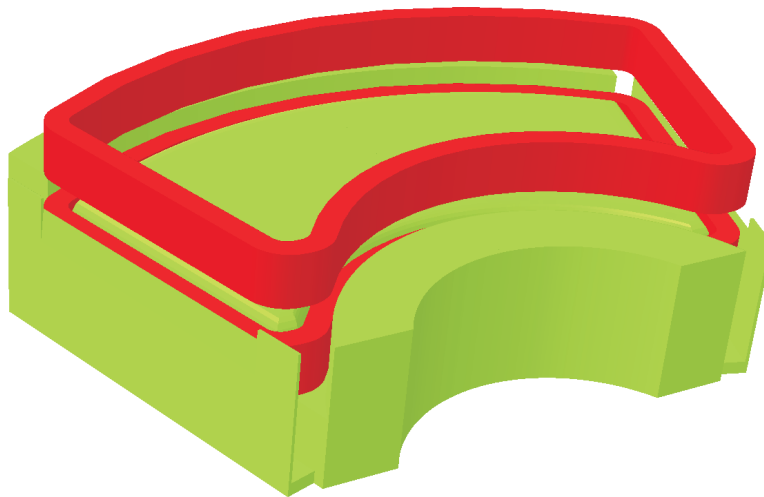
Figure 5.1: Optimized straight edge geometry.
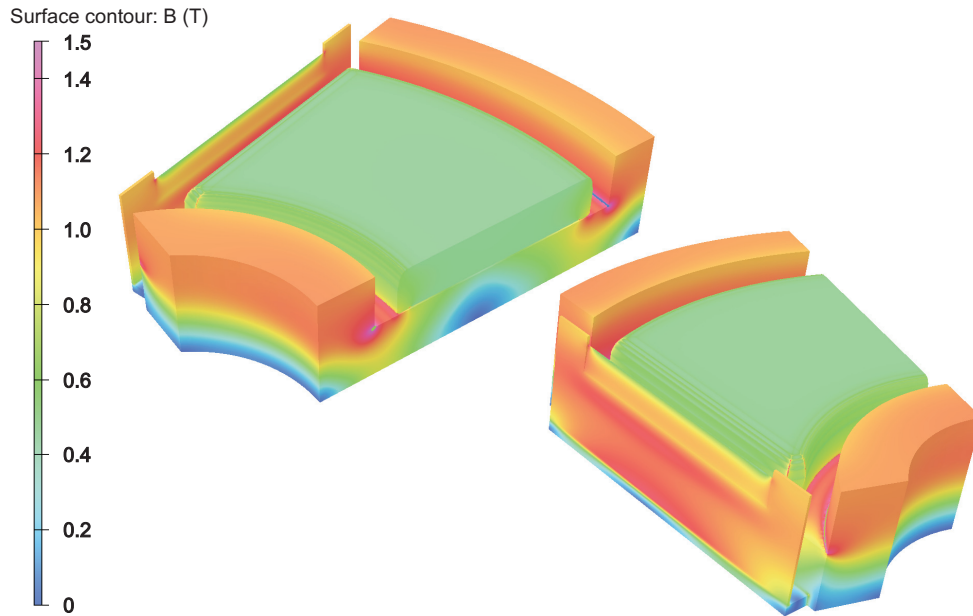
Figure 5.2: Magnetic flux density of the optimized straight edge geometry.

The coil section is changed from a square[22] to a rectangular cross section to reduce the overall width of the magnet. The steel magnetization is within the 1.5 T saturation limit as shown in figure 5.2.

A Rogowski-like profile for both the longitudinal and transverse edges of the pole is implemented.

Figure 5.3 represents a comparison between approximation of the Rogowski theoretical curve using 4, 6, 8 and 10 sectors, while figure 5.4 represents the maximum distance limit set to generate the sector Rogowski (see section 4.2) as a function of the number of sectors; the most gain in terms of approaching the theoretical curve, is going from four to six sectors. The six sectors choice is the best compromise between approximation to the theoretical curve and minimization of the number of sectors for machining and cost purposes.

---

[22]$69 \times 69 \, \text{mm}^2$, see table 4.1.
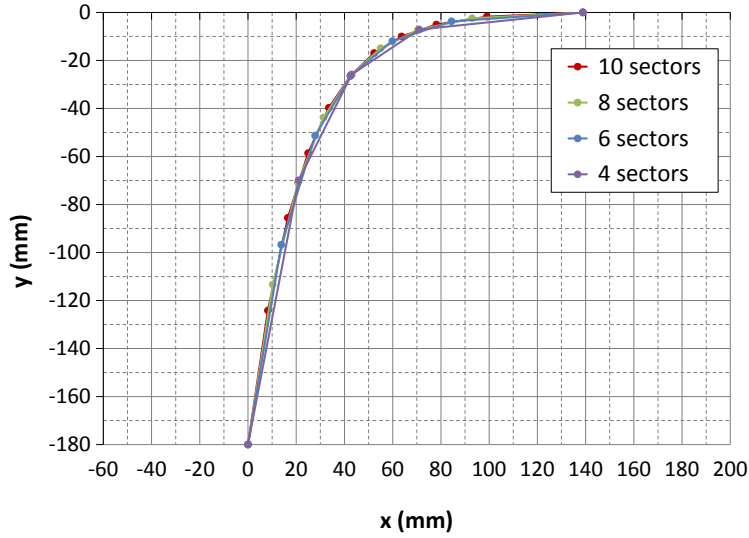
Figure 5.3: Sector Rogowski comparison: the most gain in terms of approaching the theoretical curve, is going from four to six sectors as seen in figre 5.4.
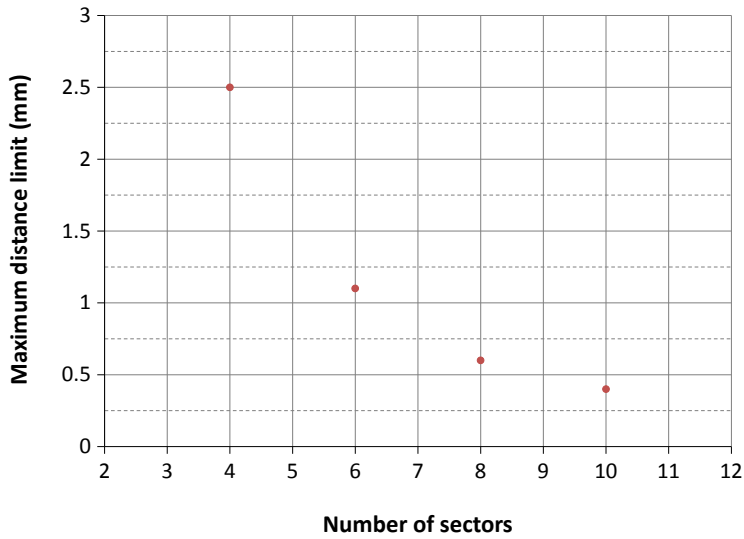
Figure 5.4: Maximum distance limit set to generate the sector Rogowski
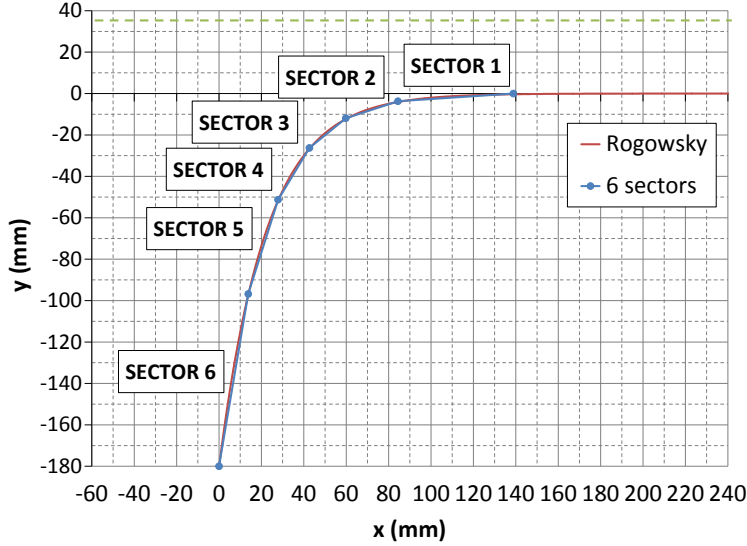
Figure 5.5: Six sectors Rogowski profile; a scaled version is implemented in the optimized straight geometry

The implemented profile is a scaled version of the theoretical Rogowski profile (as anticipated at the end of section 4.2) for a 70 mm gap being approximated by a six sector segmented line as represented in figure 5.5 (the curve is rotated for convenience); the sector distance from the theoretical curve (see section 4.2) is limited to circa 1 mm.

The scaled version of the Rogowski means the coordinate values of the sector end points (see figure 5.5) are scaled: the longitudinal (along the geometric trajectories) and transverse (radially) scaling factors are respective 61% and 40%. The scaling of the Rogowski allows to control respectively the effective field edge and the field flatness. A rendering of the pole is shown in figure 5.6.

The model has an optimized detached partial Purcell filter that allows to achieve the field flatness, represented in figure 5.7, well within the requirement of $2.5 \cdot 10^{-5}$ (notice $\times 100$ dashed curve in figure 5.7).

The effective field edge profile and the integral flatness of the optimized straight edge case are represented respectively in figure 5.8 and figure 5.9.
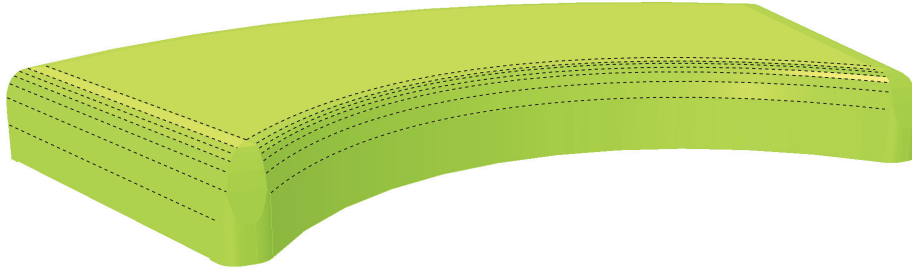
Figure 5.6: Pole of the optimized straight edge model with a six sector Rogowski scaled 61% longitudinally and 40% transversely.

These two graphs are in fact two interpretations of the same set of data: the field integrals along the geometric trajectories. In figure 5.8 the integrals are converted in effective length to be compared with the length of the theoretical hard edge case; this gives a direct information about the position of the effective field edge. In figure 5.9 the integrals are ultimately (see equation 2.12) compared against the reference trajectory one; this gives a direct information about the flatness of the integrals.

The effective field edge is in the correct location thanks to the optimization of the sector Rogowski scaling factor (61%) for the longitudinal entrance and exit edges. The effective edge presents though a slight curvature with radius of circa 80 m; this is due to the fall off of the field and it can be corrected by curving the edge outward. The effective edge presents also a small angle of 0.2 mrad. Both the curvature and the angle are not corrected since this is not the final geometry.

The transverse field fall off is also controlled by optimizing the transverse scaling factor (40%). The optimization is achieved by preventing the field flatness from dropping within the good field region (see figure 5.7).

The field integral result is a significant improvement with respect to the nominal geometry (see figure 4.5) but it still is outside the requirement (green box on figure 5.9). Since the trend of the integral flatness is consistent with the effective edge curvature, we could speculate that adjusting the latter will also fix the former.
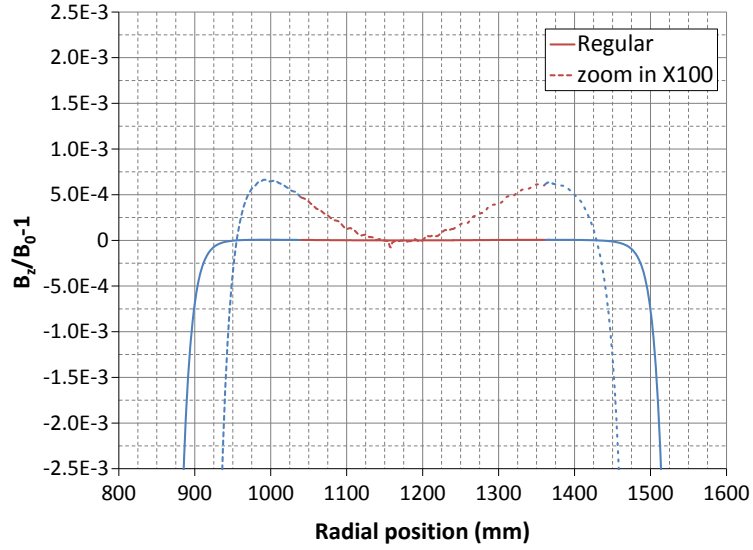
Figure 5.7: Field flatness of the optimized straight edge design.
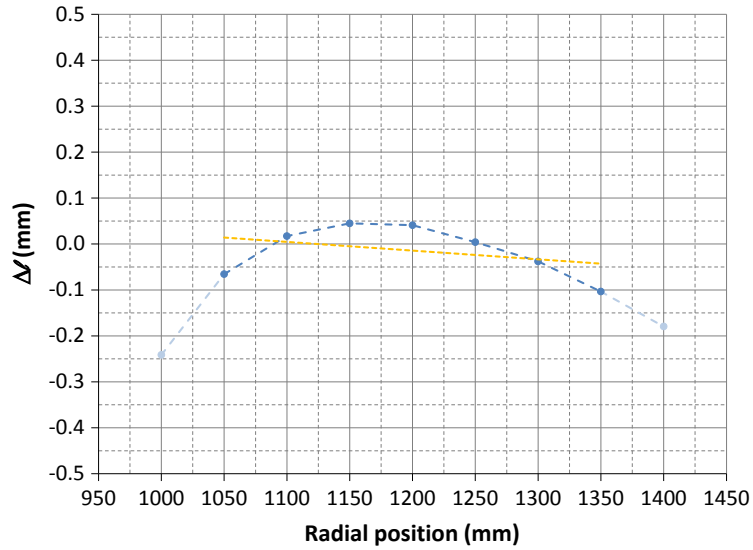
Figure 5.8: Optimized straight edge geometry effective field edge location with respect to the relative hard edge case: the linear interpolation (yellow dashed line) between 1050 mm and 1350 mm gives indications about position and angle.

Figure 5.9: Optimized straight edge geometry integral flatness with respect to the relative hard edge case: the yellow dashed line is a linear interpolation between 1050 mm and 1350 mm. The green box $(2.5 \cdot 10^{-5}$ high) represents the flatness requirement in the good field region.

5.2 OPERA-3D® field for COSY-∞

In order to have the most accurate beam dynamics model of the HRS system, it is important to transfer the two dimensional rectangular grid of the magnetic field map of the middle plane from OPERA-3D® to COSY-∞ (see section 2.3). It is possible to read such a grid into COSY-∞ from which the code computes the magnetic field everywhere else using the differential algebraic technique [41]; the issue is that COSY-∞ requires that the initial conditions, OPERA® field on each single point of the grid, are exact solutions (within the machine precision) of Maxwell's equations otherwise the outcome is not reliable. This is true only if the points happen to coincide with a node of the tetrahedral mesh produced by OPERA® while in general the field between nodes is interpolated.

Figure 5.10 shows a detailed view of the standard OPERA® mesh in the

Figure 5.10: Detailed view of the air gap region (yellow dashed line) standard mesh produced by OPERA®. Various patches of mesh can be distinguished.

air gap region; various patches of mesh indicate that there is not a particular order in the distribution of the nodes for this complex geometry (a perfectly rectangular box would be meshed in an orderly fashion).

We verified that the use of maps generated by a standard mesh fails to produce physical results in COSY-∞. So it becomes mandatory to force the nodes on the desired COSY-∞ grid, but there is not such a function in OPERA®.

If we manage to force the nodes on a desired rectangular grid (as we will shortly see), then in principle we only need a coarse mesh in between nodes as far as COSY-∞ is concerned; on the other hand a fine mesh is still necessary to calculate the integrals accurately (in the 10^{-6} range) along the geometric trajectories, that don't follow exactly a rectangular mesh and therefore include field values from OPERA® in between nodes. We have in fact run a curved grid that follows the geometric trajectories in order to

compare the integrals against the rectangular grid (for COSY-∞) and no grid cases while using the same fine mesh. The integrals from the two grid cases are within $1 \cdot 10^{-6}$, while integrals between any grid case and no grid are within $8 \cdot 10^{-6}$. The use of a grid provide a much ordered mesh that yields better result without increasing the computation time.

It was proposed to create a honeycomb-like structure superimposed on the air gap volume with the wall (of the honeycomb) intersections being the grid points, but this actually causes OPERA® to fail to create a mesh in the first place because of too many constraints posed by the structure walls.

We developed an original technique in order to achieve a COSY-∞ compatible rectangular mesh. We proposed a "bed of nails" approach where each nail is positioned on the coordinates of the grid; the nails are simply OPERA® wire-edges that have no volume. The nails layout imposed no particular constraints on the mesher, because of the absence of walls between nails, other than forcing it to put a node at each end of every nail.

The created "bed of nails" is superimposed on the air gap volume, as shown in figure 5.11 (A-B), which base is the middle plane of the magnet where we want to extract the COSY-∞ grid. The nails are then subtracted from the air volume leaving it with volume-less holes, see figure 5.11 (C-D).

The mesh obtained applying the "bed of nails" technique is shown in figure 5.12. Compared with the standard mesh (figure 5.10) the nodes are ordered accordingly to the desired grid and the mesh is overall more regular. The end of each and every nail coincides with a node (red arrows in figure 5.12), but of course not every node coincides with the end of a nail.

The use of the "bed of nails" allows for the successful transfer of the two dimensional map from OPERA® to COSY-∞. As stated earlier, the technique has also the benefit of achieving one order of magnitude more accurate solution without further refining the mesh size, that would increase the demand on the computing system. This has been established by comparing a solution, for the same geometry, with no nails to two other solutions using the nails in two different grids. Using the nails technique is equivalent to increasing the number of mesh points, but with the advantage of not increasing the computational time.
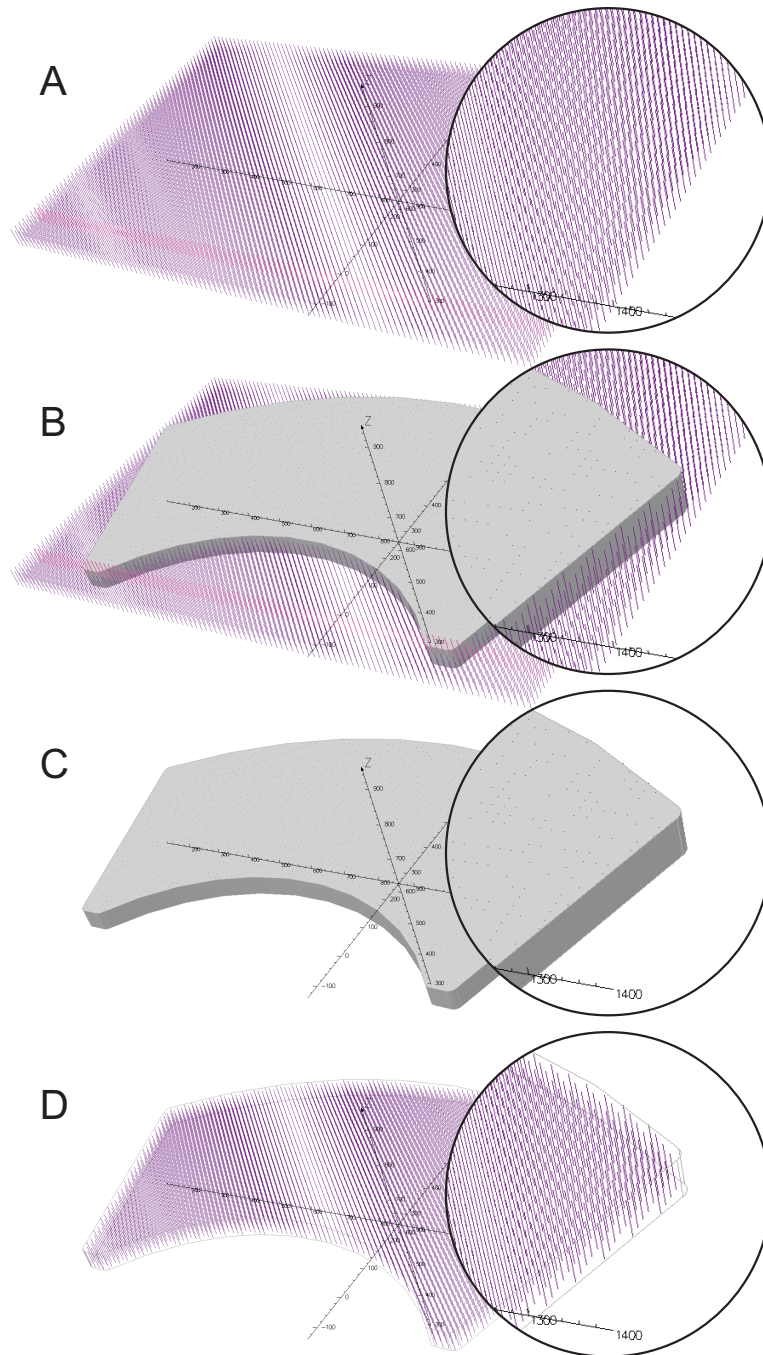
Figure 5.11: Bed of nails (A) superimposed on the air gap volume (B) then subtracted from the air gap (C); the remaining structure has volume-less holes (D). The nails are OPERA® wire-edges that have no volume.
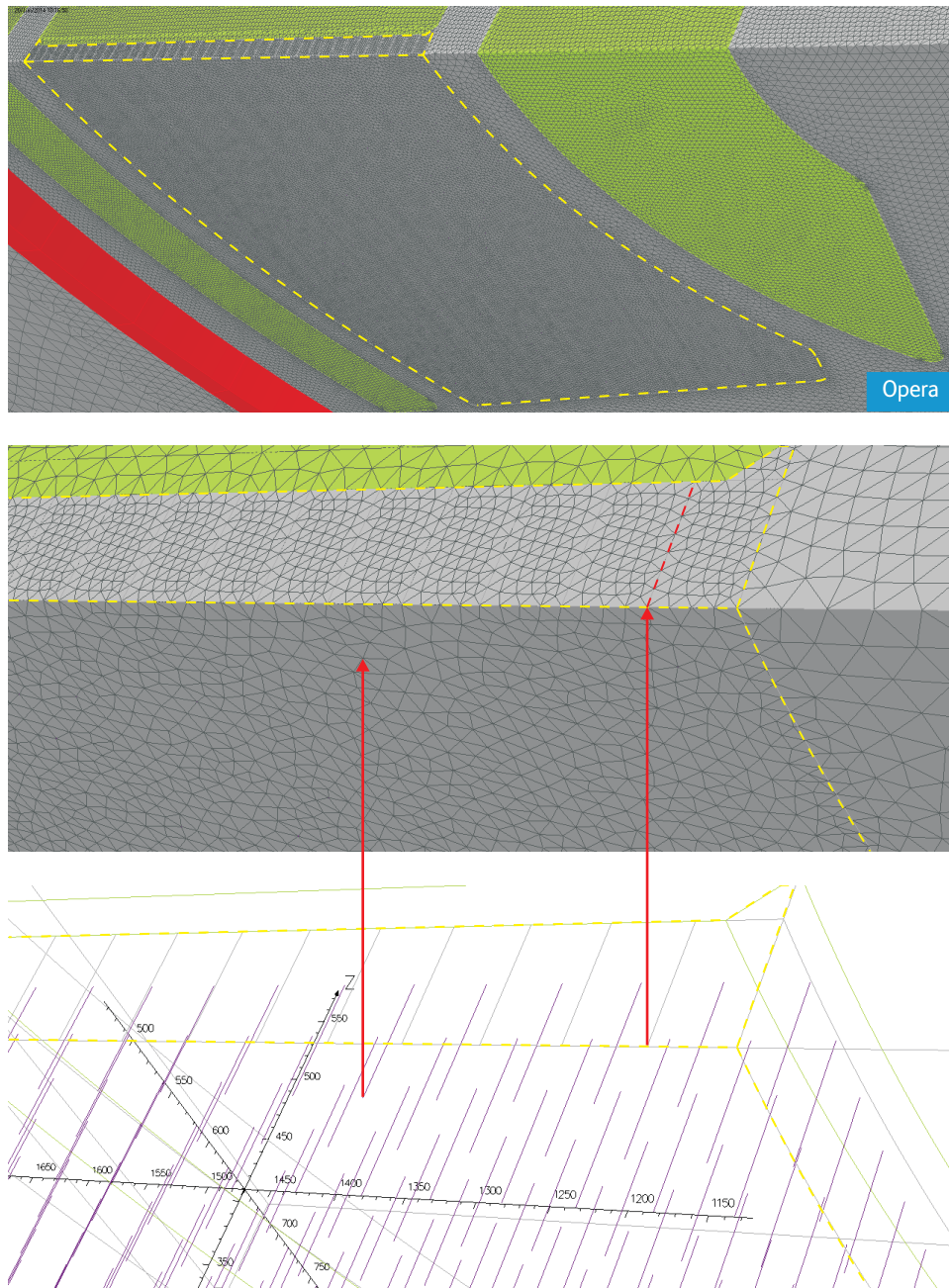
Figure 5.12: Air gap volume (yellow dashed line) meshed with the "bed of nails" technique (top). Magnified section of the air gap (central and bottom): evidence (red arrows) that the end of a given nail (red dashed line) coincides with a node.

5.3 Final curved edge model

The final geometry (HRS-120-23C62) is obtained from the optimized straight edge model by applying a curvature to both the pole entrance and exit edges and the field clamp. The coil follows all the curvature of the pole. The final result is shown in figure 5.13.

The curvature is necessary to correct the second order aberration; this aberration has a characteristic "C" shape in the transverse phase space at the exit of the dipole, as represented in figure 5.14; this means that particles with extreme angles with respect to the reference trajectory are bent more. In order to limit the bending of such particles, the pole length is gradually reduced as it moves towards the sides of the pole in such a way that the the field integral for particles traveling along extreme trajectories (higher angles with respect to the reference trajectory) is reduced. This is accomplished geometrically by curving the edges of the pole.

The steel magnetic field distribution of the final design is shown in figure 5.15 when the magnet is run in full excitation mode producing a vertical magnetic field component $B_0 = 0.458$ T. In this full excitation mode, the field in most of the steel is less than 1.2 T and it peaks in the field clamp at
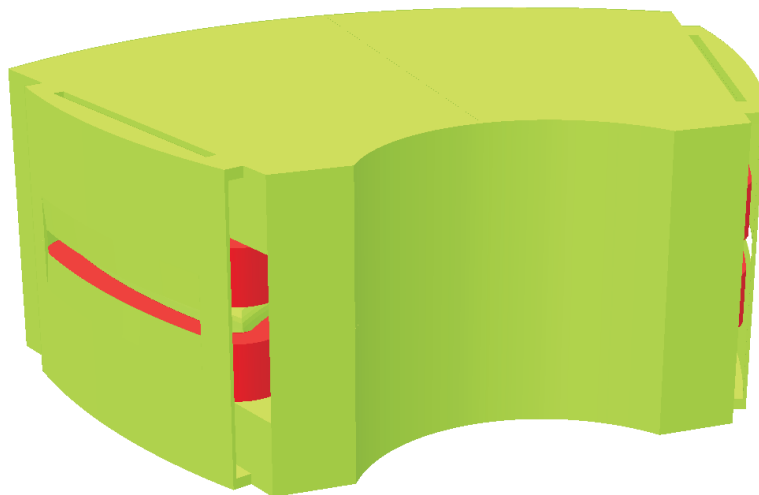
Figure 5.13: Final geometry.

Figure 5.14: Characteristic "C" shape of the second order aberration.

1.4 T, below the saturation level of 1.5 T (see figure 2.9) as per requirement. Figure 5.15 shows also the balance between the inner and outer return yokes obtained with the second method (see section 3.4).

The main parameters of the final design are listed in table 5.1. The edge angle and curvature are relative to the hard edge magnet case. It is interesting to compare the 2.3 m required radius of curvature of the edges, with the natural 80 m curvature in the straight edge model; it is clear now that we can define the latter as a slight curvature that has no significant effect on the beam.

The final geometry employs a scaled six sector Rogowski with two different scaling factors in the horizontal plane (parallel to the pole face) for the longitudinal and transverse directions, similar to the optimized straight edge geometry. In the vertical plane (perpendicular to the pole face) though, we maintain[23] the same longitudinal scaling factor also for the transverse direction in order to facilitate the machining process by simplifying the geometry

---

[23]Suggested by Dr. Thomas Planche.

Surface contour: B (T)
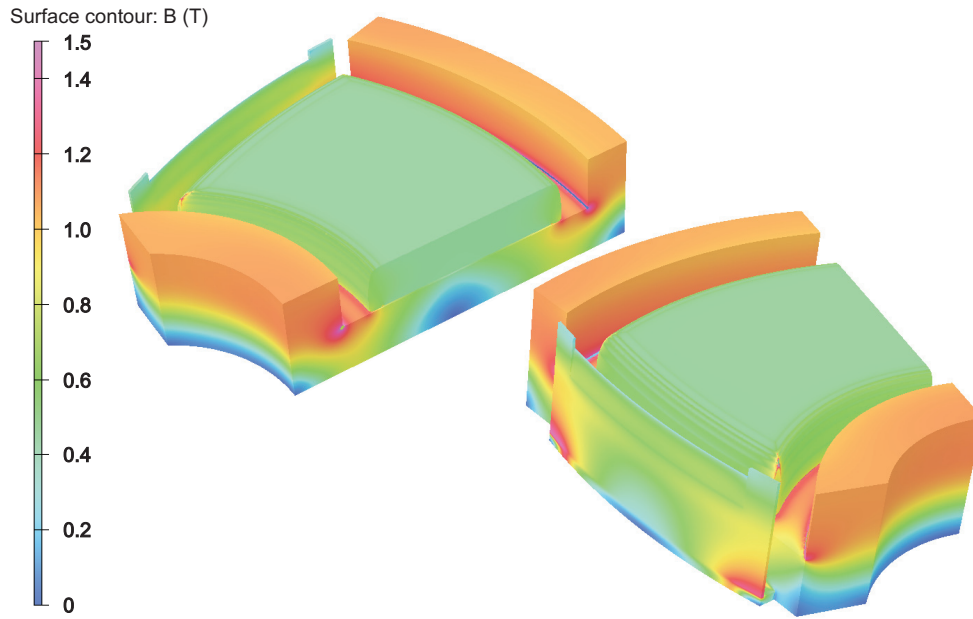
Figure 5.15: Magnetic flux density of the final design in full excitation mode.

of the corners (avoiding unnecessary small steps) where the longitudinal and transverse directions meet, as represented in figure 5.16. This means that the transverse (less critical) profile is no longer a Rogowski; simulations

Table 5.1: Final geometry main parameters.

Geometric parameter	Dimension
Bending radius	1200 mm
Bending angle	90 degrees
Entrance and exit hard edge angle	26.5 degrees
Pole gap	70 mm
Pole height	185 mm
Pole base height	205 mm
Pole width	760 mm
Hard edge curvature	2238 mm
Coil	$158 \times 80 \, \mathrm{mm}^2$
Coil to steel vertical separation	8.5 mm
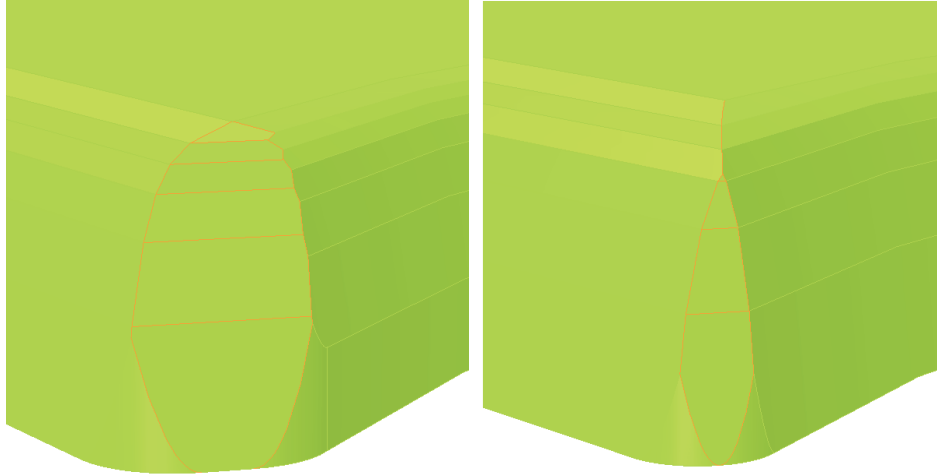
Figure 5.16: Detail of the pole corner for the optimized straight edge (left) and final curved geometry (right): the curved geometry maintain the same scaling factor in the vertical plane (different in the horizontal) producing a simplified geometry of the corner (see orange line for reference).

show that this hybrid profile is still effective in avoiding saturation, as seen in figure 5.15.

The field clamps are optimized together with the pole edges in order to achieve the effective field edge corresponding to the hard edge magnet with curved pole. The final fringe field is shown in figure 5.17 plotted amongst profiles from other clamp geometries for comparison. The final fringe field profile minimizes the first derivative of the magnetic field (see section 4.4) as shown in figure 5.18.

The field flatness of the final geometry is shown in figure 5.19. The final value of $8 \cdot 10^{-6}$ within the good field region is three times lower than the requirement of $2.5 \cdot 10^{-5}$; it is also a factor of two better with respect to other magnetic dipoles designed for similar high resolution separators [46].

The integrals calculated from the final OPERA$^{®}$ model are listed in table 5.2 together with the hard edge ones.
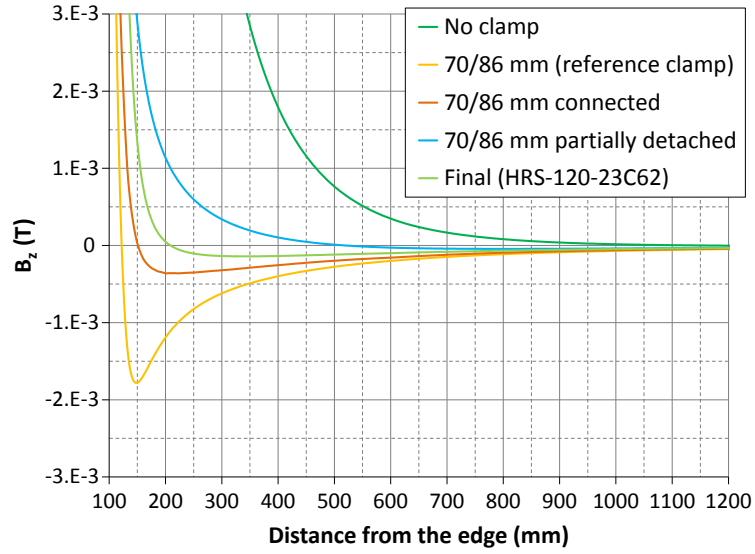
Figure 5.17: Fringe field of the final geometry.
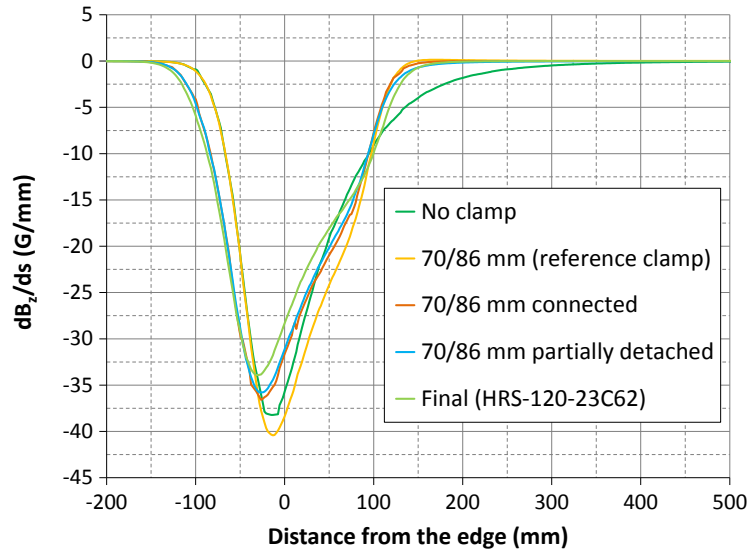
Figure 5.18: First derivative of the fringe field of the final geometry.
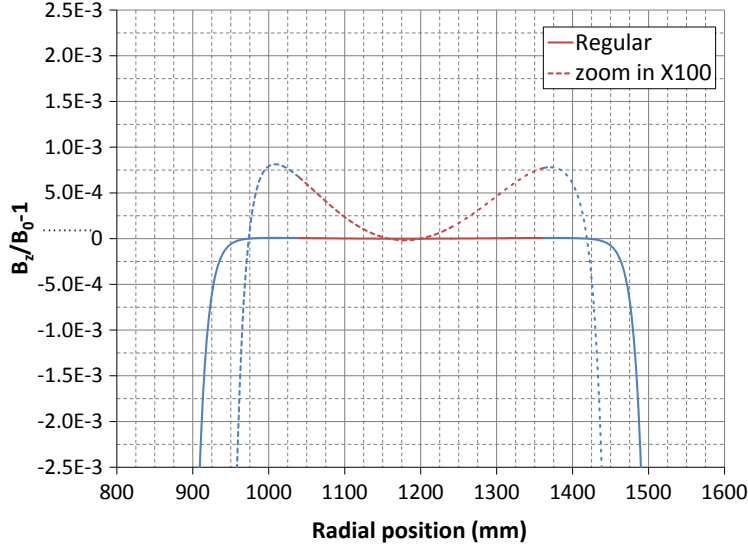
Figure 5.19: Final geometry field flatness for the full excitation mode.

Table 5.2: Final geometry calculated integrals.

Geometric trajectory ρ (mm)	Hard-edge (T·mm)	OPERA® (T·mm)	$IR_\rho - 1$	IF_ρ
1000	802.195	802.147	-6.0·10^{-5}	-6.2·10^{-5}
1050	819.383	819.382	-1.5·10^{-6}	-3.6·10^{-6}
1100	835.414	835.417	4.4·10^{-6}	2.2·10^{-6}
1150	850.275	850.282	8.7·10^{-6}	6.5·10^{-6}
1200 (reference)	863.955	863.957	2.2·10^{-6}	0
1250	876.433	876.448	5.2·10^{-6}	3.1·10^{-6}
1300	887.727	887.731	4.4·10^{-6}	2.2·10^{-6}
1350	897.796	897.798	1.8·10^{-6}	-4.0·10^{-7}
1400	906.637	906.636	-1.4·10^{-6}	-3.6·10^{-6}

The effective edge profile is represented in figure 5.20; as for the other ge-
ometries, the graph represents the distance of the effective edge from the rel-
ative curved hard edge case. Figure 5.20 linear interpolation (yellow dashed
line) shows that the effective edge matches the hard-edge case in terms of
curvature and position. The integral flatness is shown in figure 5.21.

110

Figure 5.20: Final geometry effective field edge location with respect to the relative hard edge case for the full excitation mode: the linear interpolation (yellow dashed line) between 1050 mm and 1350 mm gives indications about position and angle.
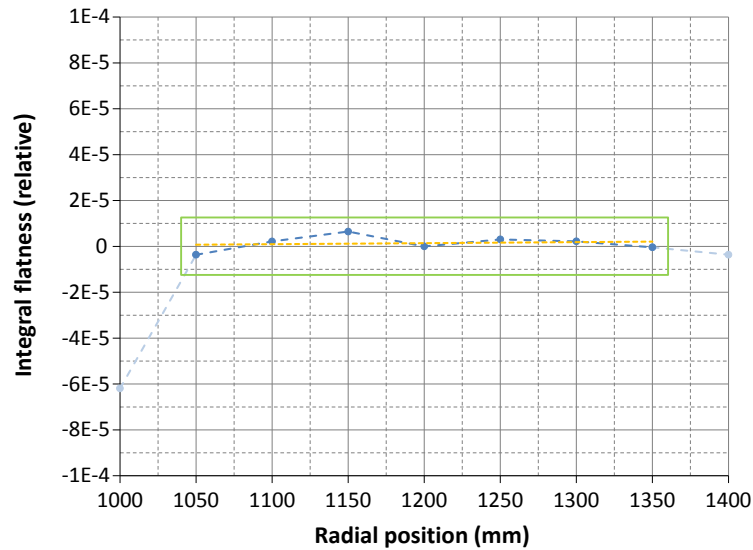
Figure 5.21: Final geometry integral flatness with respect to the relative hard edge case for the full excitation mode.

111

All the values in the good field region (± 160 mm around the reference trajectory) are within the requirement of $2.5 \cdot 10^{-5}$ (green box in figure 5.21).

The final model is also run at low excitation to produce a vertical magnetic field component $B_0 = 0.098$ T; this is close to the nominal value to bend mass 11 at 60 kV (see section 2.2). It should be noted that for such low masses a resolving power of 20000 is not necessary (see figure 1.13). Figure 5.22 is a rendering of the magnetic field distribution for the low excitation case (HRS-120-23C65).

The field flatness for the low excitation mode is represented in figure 5.23, while the effective field edge profile and integral flatness for the same mode are represented respectively in figure 5.24 and figure 5.25.

The effective edge shifted about 50 μm and present an angle with respect to the hard edge case of circa 0.1 mrad. The shift is acceptable since the effective edge is still within the requirement. The small angle mismatch, circa $2 \cdot 10^{-4}$ of the design angle, translates into a slightly different vertical focusing of the dipole; this can be corrected if necessary with a dedicated
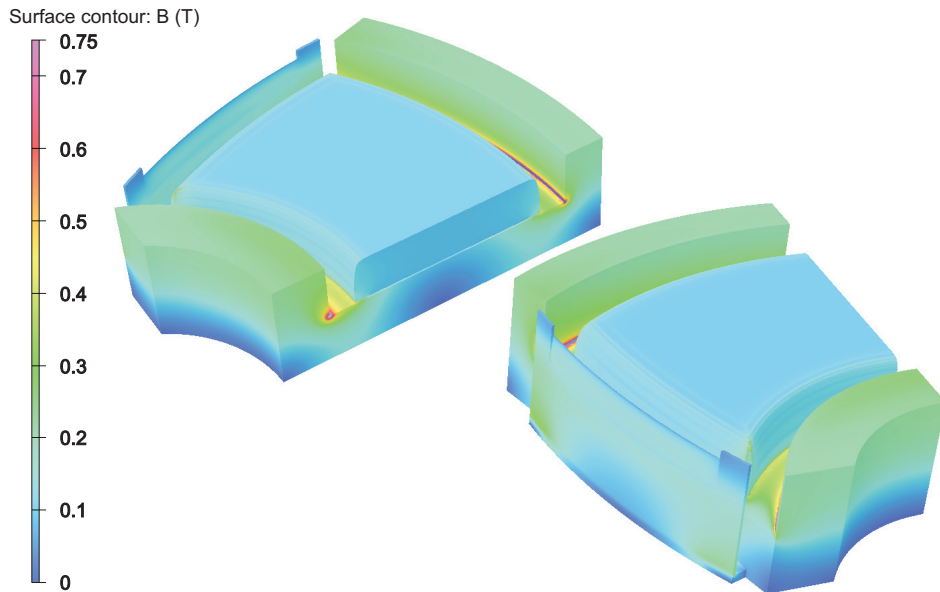
Figure 5.22: Magnetic flux density of the final design in low excitation mode; notice the change of scale with respect to the full excitation mode.

quadrupole in front of the magnet foreseen in the beam dynamics layout [1].
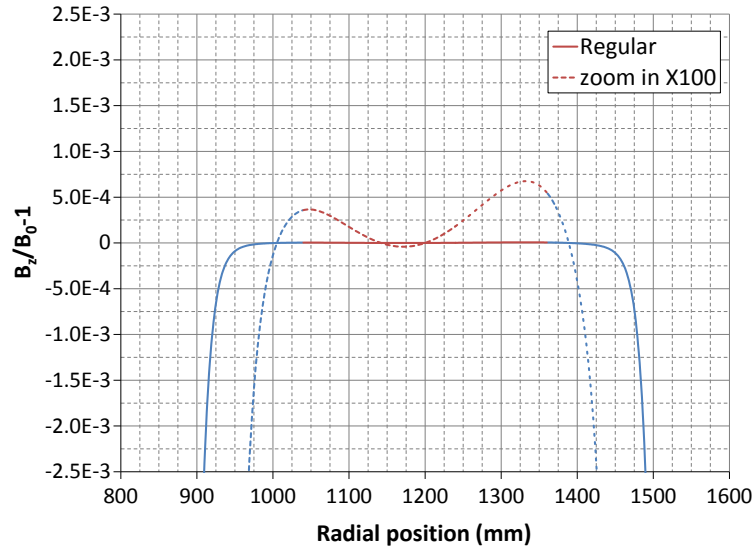
Figure 5.23: Final geometry field flatness for the low excitation mode.
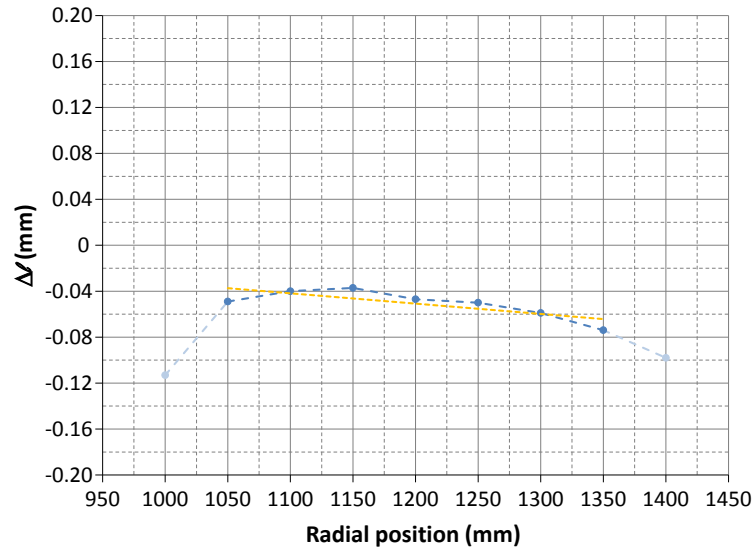
Figure 5.24: Final geometry effective field edge location with respect to the relative hard edge case for the low excitation mode.

Figure 5.25: Final geometry integral flatness with respect to the relative hard edge case for the low excitation mode.

The integral flatness is still mostly within the requirement but for the most outer trajectory. The overall flatness is compatible with a 14000 resolving power that, as mentioned, is not required in this low mass range. Most likely the integral flatness in the low excitation case will still be enough to have the HRS system to perform at a higher resolving power thanks to the high order multipole corrector [1].

5.4 Engineering considerations

In this section we are going to briefly discuss all the engineering features required to assemble, transport and operate the magnet. These are detailed engineering aspects of the real magnet that may impact its performance and therefore we need to confirm their viability in OPERA®. As a matter of fact many of the implemented features require a re-optimization of some of the magnet parameters. We list them in table 5.3; we don't provide a detailed description of each feature since they are not part of the design optimization

Table 5.3: Engineering features applied to the final geometry.

Propose Engineering feature	OPERA simulation	Result
Pole mount	HRS-120-23C62eng	acceptable
Yoke mount and hoist rings	HRS-120-23C62eng2	acceptable
Chamfer of the inner yoke	HRS-120-23C62eng3	acceptable
Buckley coil proposal	HRS-120-23C62eng4	acceptable but not adopted
Reduced field clamp	HRS-120-23C62eng5	acceptable
Field clamp mount	HRS-120-23C62eng6	acceptable
Field clamp squared	HRS-120-23C62eng7	not acceptable
Propose single-rib field clamp	HRS-120-23C62eng9	acceptable
Pole holes $\oslash = 12\,\text{mm}$	HRS-120-23C62eng12	acceptable
Field clamp connections	HRS-120-23C62eng13	acceptable
5 mm blended field clamp knife edge	HRS-120-23C62eng14	acceptable
Thermowells	HRS-120-23C62eng15	acceptable
Final coil 159×76	HRS-120-23C62eng16	acceptable
Move coil transition from outer to inner coil channel	HRS-120-23C62eng21	acceptable

(but rather input from the magnet engineer and draftsman) and because the purpose is just to show that every aspect of the magnet has been taken into account.

The features are applied starting from the final design; each feature is simulated cumulatively, following the same order given in table 5.3, triggering the required parameter re-optimization at each step.

The results of each simulation are compared to the final design with respect to field flatness, effective field position and integral field flatness. The result reported in table 5.3 is in terms of acceptability. All the features are simulated as air (voids in the steel); in one case air has been substituted with stainless steel ($\mu_r = 2$, worst case scenario) in order to simulate a bolt, showing no difference in the final result.

A rendering of the final geometry with the engineering features (HRS-120-23C62eng21) is represented in figure 5.26. The field flatness, effective

field edge location and integral flatness of the final engineered geometry are shown respectively in figure 5.27, figure 5.28 and figure 5.29.
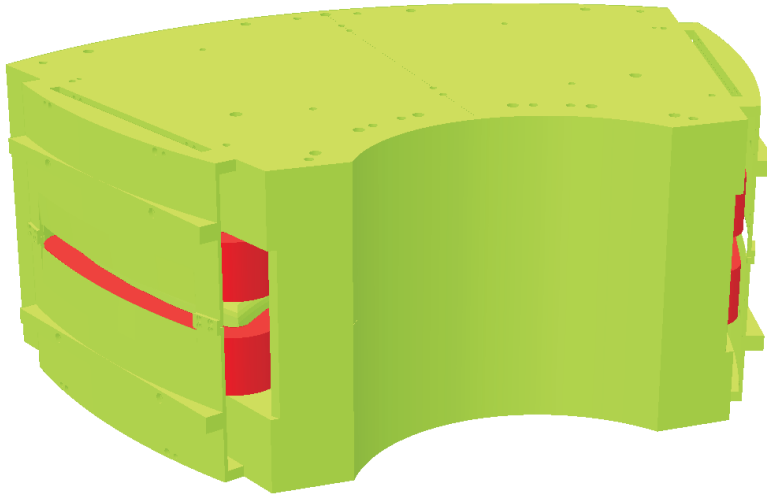
Figure 5.26: Final design with engineering features (HRS-120-23C62eng21).

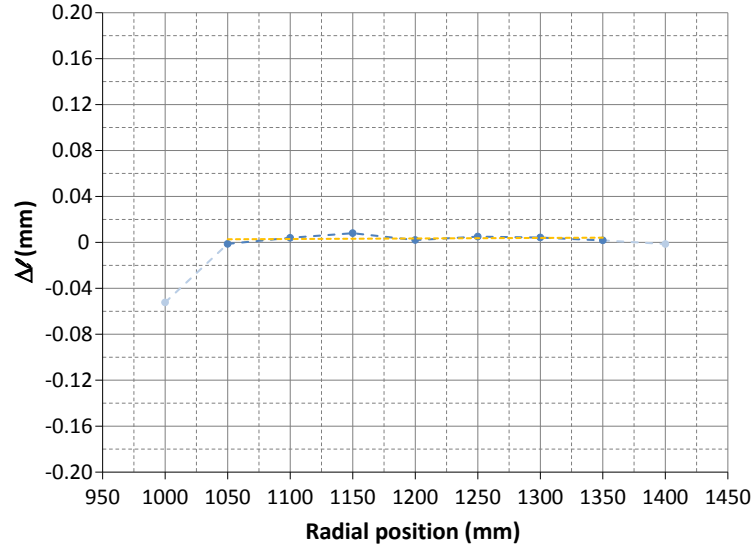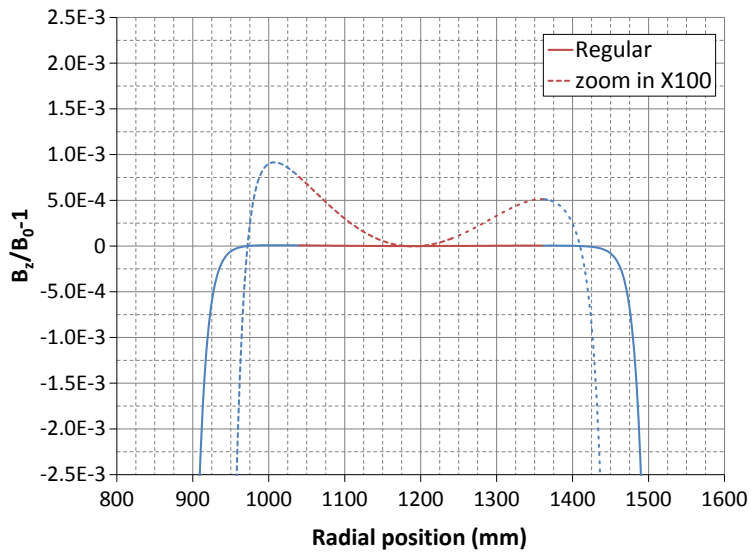Figure 5.27: Final engineered geometry field flatness with respect to the hard edge case.
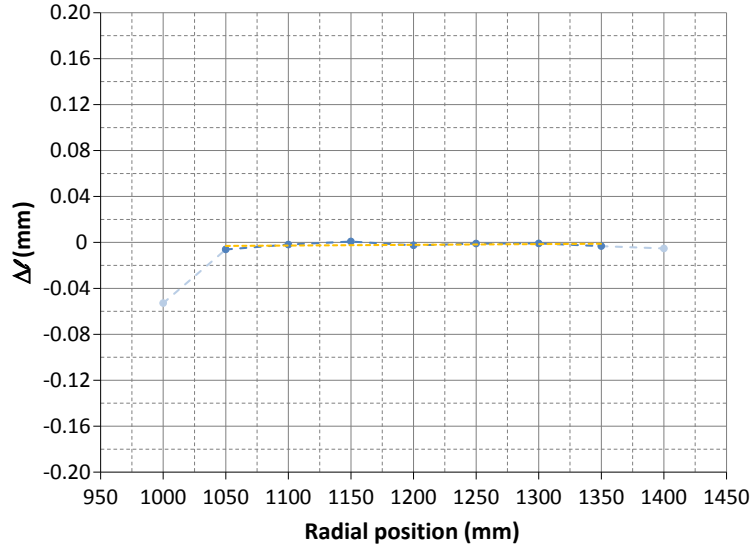
Figure 5.28: Final engineered geometry effective field edge location with respect to the relative hard edge case for the full excitation mode.
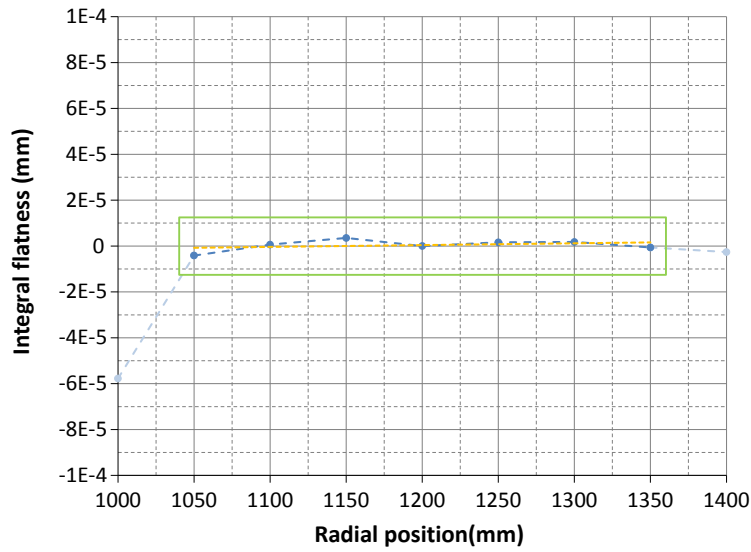
Figure 5.29: Final engineered geometry integral flatness with respect to the relative hard edge case for the full excitation mode.

Finally a photograph of the first HRS manufactured[24] magnetic dipole is shown in figure 5.30.

Figure 5.30: First HRS manufactured magnetic dipole (with field clamp edges protected by white Styrofoam). Photograph courtesy of Buckley Systems.

---

[24]by Buckley Systems - http://www.buckleysystems.com/

Chapter 6

Conclusion

The working hypothesis, and ultimately the magnet design, needs to be validated by testing the optical performance of the dipole field within the HRS system.

This magnetic field[25] is used to run a beam dynamics calculation for beams transported from the entrance to the exit (selection) slit of the HRS. This calculation is compared against the one that uses an ideal uniform field for a dipole.

Figure 6.1 shows the distribution of two beams, green and red, in the horizontal phase space at the selection slit for the two cases: ideal (top) versus realistic (bottom). The two transported beams have the same $3\,\mu$m horizontal emittance and they have a mass difference of one in twenty thousand. The green beam is centered around the selection slit ($x = 0$) with a $0.1\,$mm aperture; this beam is selected and transported to the experimental station. The red will be stopped by the $0.1\,$mm selection slit.

The comparison shows that the realistic field performs as well as the ideal field. This result confirms that minimizing the integral field variation of a separator dipole, with respect to the system resolution, is equivalent to minimizing aberrations. The result also validates the final design of the HRS magnet.

The design of the HRS system and the magnet in particular has been presented to an international review committee as standard practice for all TRIUMF projects. Based on the feedback from the committee experts, the HRS project is now proceeding to the manufacturing and installation stage.

The two dipoles have been manufactured to the required precision. A two dimensional field mapping of the dipoles has been performed and it

---

[25]Calculated and exported from OPERA®.

shows the expected field quality.
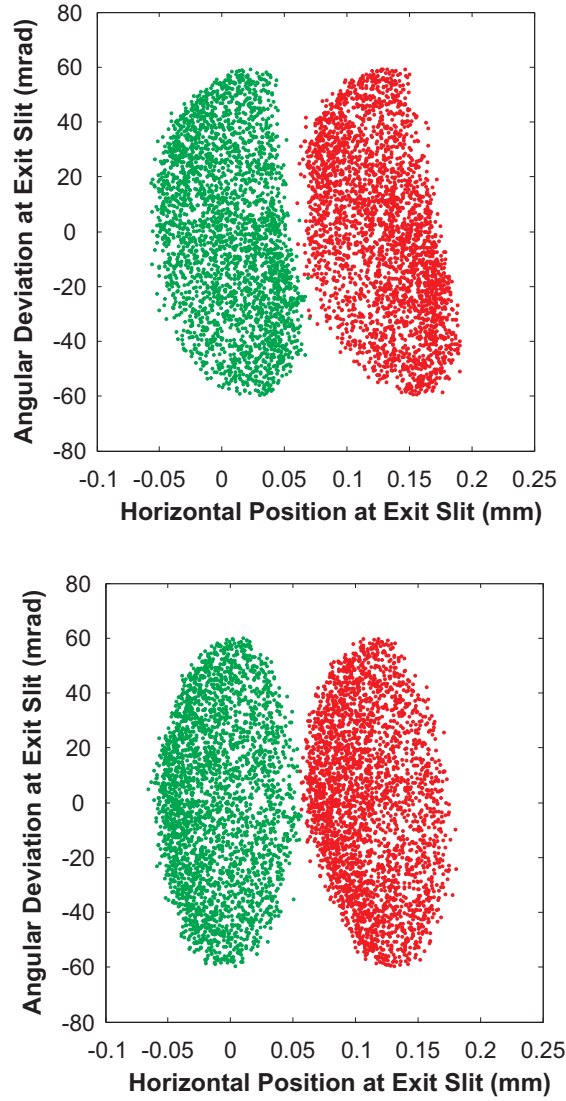
Figure 6.1: Transverse horizontal phase space at the selection (exit) slit calculated in COSY-∞ with ideal dipole field (top) and OPERA$^{\circledR}$ imported field (bottom).

6.1 HRS system developments

A further investigation of the field quality of the manufactured HRS dipoles is planned at TRIUMF. Such investigation foresees an integral field mapping rather than a local (points on a Cartesian grid) mapping as performed by the manufacturer. The integral field mapping will measure the field variation within a loop around the geometric trajectories; the measurement is a direct application of Faraday's law of induction for which a magnetic flux variation through an electric circuit (the loop) generates an electromotive force in the circuit itself. The field variation for different geometric trajectories (loops) is going to be compared against the ones extracted from the OPERA$^{®}$ model. It is expected that these integral measurements are sensitive to the field variation the magnet is designed for, giving indication of the quality of the magnetic field.

One characteristic of the HRS system that makes it unique is a complete set of diagnostics devices to characterize the beam. Lack of diagnostic has been identified as an issue for the CARIBU high resolution mass separator (mentioned in section 1.4), in particular diagnostic devices capable of reconstructing the transverse phase space, emittance rigs, at the selection slit. Our system has an emittance rig both at the image and object (selection) slit locations.

Even though both the beam dynamics and the magnets are designed to minimize aberrations, it is expected that some level of high order corrections is necessary to compensate for manufacturing and installation tolerances. In order to compensate for such high order aberrations, a device called a multipole has been designed and its mode of operation is under development. The multipole consists of a set of electrodes that can be adjusted individually to a certain voltage to create an electrostatic corrective field in the transverse direction. The multipole, located in between the two dipoles (see figure 2.6), is designed based on the operational experience of the CARIBU system. Our design differs though from the latter in the geometric layout of the electrodes that follows a rectangular rather than a circular pattern. The rectangular shape better suits the beam envelope and it requires a lower voltage to be

121

applied to the electrodes. This design allows for a better control of the corrective field.

6.2 Future upgrades

As seen in chapter 2, the performance of the HRS depends greatly on the quality of the beam. Our system is designed for a transverse horizontal emittance of $3\,\mu$m; for bigger value, the emittance can be either cut (meaning beam losses) or reduced using a device called RFQ cooler. Such device is a gas filled RFQ in which the beam loses transverse moment by stochastic interactions with the gas atoms. The transverse momentum loss results in an emittance reduction. Even though an RFQ cooler is not in the present project budget, the beam lines surrounding the HRS system are designed to accommodate this future upgrade.

6.3 Conclusion

In this work we managed to successfully demonstrate that minimizing the field integral variation with respect to the system resolution within the good field region is equivalent to reducing the magnetic field contribution to the system aberration (working hypothesis); this means that the system corrections required to compensate for magnetic field imperfection are minimized. We also ultimately produced the design of the magnetic dipole for the High Resolution Separator (HRS) of the new ARIEL facility at TRIUMF.

An important issue that we encountered and developed during the work is the relation between field flatness and pole gap (see section 3.1). The perception that a smaller gap (for a fixed width) produces a better flatness is not correct. In the large width to gap ratio limit, a smaller gap results in worse flatness; this is a result of the fact that the permeability is finite.

We also invented a new technique to force the OPERA mesh nodes on a predetermined grid (see section 5.2). This is not only fundamental to transfer the correct values of the magnetic field to the COSY-∞ beam dynamics

code, but it also improves the mesh quality producing a more accurate solution for the same computational time.

Once the HRS system is commissioned, ARIEL will be an ISOL facility capable of producing and selecting heavy masses RIB beams with high resolution. The HRS system will finally enable the pursue of experiments like ^{132}Sn.

Combined with the ISAC capability of delivering high energy, ARIEL will make TRIUMF highly competitive with other ISOL facilities like Isotope Separation On Line DEvice (ISOLDE) at Conseil Europeen pour la Recherche Nucleaire (CERN) or CARIBU at ANL.

Furthermore the unique capability of delivering three simultaneous radioactive beams will position TRIUMF in a leading role for decades to come.

Bibliography

[1] J. Maloney, R. Baartman, and M. Marchetto, "New design studies for TRIUMF's ARIEL high resolution separator," *Nuclear Instruments and Methods in Physics Research Section B: Beam Interactions with Materials and Atoms*, vol. 376, pp. 135 – 139, 2016. Proceedings of the {XVIIth} International Conference on Electromagnetic Isotope Separators and Related Topics (EMIS2015), Grand Rapids, MI, U.S.A., 11-15 May 2015.

[2] M. Marchetto, "Progress and plans for high mass beam delivery at TRIUMF," *Heavy Ion Accelerator Technology Conference, Chicago, Illinois, USA*, 2012.

[3] M. Marchetto, F. Ames, P. Bender, B. Davids, N. Galinski, A. Garnsworthy, G. Hackman, O. Kirsebom, R. Laxdal, D. Miller, *et al.*, "In flight ion separation using a linac chain," *Linear Accelerator Conference, Tel-Aviv, Israel*, pp. 1059–1063, 2012.

[4] M. Marchetto, A. Bylinskii, R. Laxdal, *et al.*, "Beam dynamics studies on the ISAC-II superconducting linac," *Linear Accelerator Conference, Knoxville, Tennessee, USA*, p. 312, 2006.

[5] M. Marchetto, M. Comunian, A. Palmieri, A. Pisent, and E. Fagotti, "Study of a high-current 176 MHz RFQ as a deuteron injector for the SPES project," *European Particle Accelerator Conference, Lucerne, Switzerland*, pp. 251–253, 2004.

[6] B. N. Taylor and A. Thompson, "The international system of units (SI)," 2008.

Bibliography

[7] M. Lieuvin, "Design issues of radioactive ion beam facilities," *EPAC96, Sitges, SPAIN*, 1996.

[8] D. J. Morrissey, "Status of the FRIB project with a new fragment separator," *Journal of Physics: Conference Series*, vol. 267, no. 1, p. 012001, 2011.

[9] D. J. Morrissey and B. M. Sherrill, "Radioactive nuclear beam facilities based on projectile fragmentation," *Philosophical Transactions of the Royal Society of London A: Mathematical, Physical and Engineering Sciences*, vol. 356, no. 1744, pp. 1985–2006, 1998.

[10] T. P. Wangler, *RF Linear accelerators.* John Wiley & Sons, 2008.

[11] M. Conte and W. W. MacKay, *An introduction to the physics of particle accelerators.* world scientific, 2008.

[12] H. Geissel, P. Armbruster, K. Behr, A. Brünle, K. Burkard, M. Chen, H. Folger, B. Franczak, H. Keller, O. Klepper, *et al.*, "The GSI projectile fragment separator (FRS): a versatile magnetic system for relativistic heavy ions," *Nuclear Instruments and Methods in Physics Research Section B: Beam Interactions with Materials and Atoms*, vol. 70, no. 1-4, pp. 286–297, 1992.

[13] D. J. Morrissey, B. M. Sherrill, M. Steiner, A. Stolz, and I. Wiedenhoever, "Commissioning the A1900 projectile fragment separator," *Nuclear Instruments and Methods in Physics Research Section B: Beam Interactions with Materials and Atoms*, vol. 204, pp. 90–96, 2003.

[14] A. Artukh, Y. M. Sereda, S. Klygin, G. Kononenko, Y. G. Teterev, A. Vorontzov, G. Kaminski, B. Erdemchimeg, V. Ostashko, Y. N. Pavlenko, *et al.*, "The COMBAS fragment separator," *Instruments and Experimental Techniques*, vol. 54, no. 5, pp. 668–681, 2011.

[15] P. G. Bricault, F. Ames, M. Dombsky, P. Kunz, and J. Lassen, "Rare isotope beams at isactarget & ion source systems," *Hyperfine Interactions*, vol. 225, pp. 25–49, 2014.

Bibliography

[16] M. Dombsky and P. Kunz, "Isac targets," *Hyperfine Interactions*, vol. 225, pp. 17–23, 2014.

[17] R. Kirchner, "Review of ISOL targetion-source systems," *Nuclear Instruments and Methods in Physics Research Section B: Beam Interactions with Materials and Atoms*, vol. 204, pp. 179 – 190, 2003. 14th International Conference on Electromagnetic Isotope Separators and Techniques Related to their Applications.

[18] R. Kirchner, "Progress in ion source development for on-line separators," *Nuclear Instruments and Methods in Physics Research*, vol. 186, no. 1, pp. 275 – 293, 1981.

[19] R. Kirchner and E. Roeckl, "Investigation of gaseous discharge ion sources for isotope separation on-line," *Nuclear Instruments and Methods*, vol. 133, no. 2, pp. 187–204, 1976.

[20] R. Geller, "Highly charged ECR ion sources: Summary and comments (invited)," *Review of Scientific Instruments*, vol. 61, no. 1, 1990.

[21] J. Lassen, P. Bricault, M. Dombsky, J. Lavoie, C. Geppert, and K. Wendt, "Resonant ionization laser ion source project at TRIUMF," *Hyperfine Interactions*, vol. 162, no. 1-4, pp. 69–75, 2005.

[22] J. Dilling and R. Krücken, "The experimental facilities at ISAC," *Hyperfine Interactions*, vol. 225, no. 1-3, pp. 111–114, 2014.

[23] R. Baartman, F. Bach, Y. Bylinsky, J. Cessford, G. Dutto, D. Gray, A. Hurst, K. Jayamanna, M. Mouat, Y. Rao, *et al.*, "Reliable production of multiple high intensity beams with the 500 mev TRIUMF cyclotron," *Cyclotrons and Their Application, Lanzhou, China*, p. 280.

[24] I. Bylinskii and M. Craddock, "The TRIUMF 500 mev cyclotron: the driver accelerator," *Hyperfine Interactions*, vol. 225, no. 1-3, pp. 9–16, 2014.

[25] P. Kunz, C. Andreoiu, P. Bricault, M. Dombsky, J. Lassen, A. Teigelh-fer, H. Heggen, and F. Wong, "Nuclear and in-source laser spectroscopy with the isac yield station," *Review of Scientific Instruments*, vol. 85, no. 5, 2014.

[26] G. Dutto, R. A. Baartman, P. G. Bricault, I. Bylinskii, A. Hurst, R. E. Laxdal, Y.-N. Rao, L. Root, P. Schmor, G. Stinson, *et al.*, "Simul-taneous extraction of two stable beams for ISAC," *European Particle Accelerator Conference, Genova, ITALY*, p. 3505, 2008.

[27] I. Bylinskii, R. Baartman, G. Dutto, K. Fong, A. Hurst, M. Laverty, C. Mark, F. Mammarella, M. McDonald, A. Mitra, *et al.*, "TRIUMF 500 mev cyclotron refurbishment," *Cyclotrons and Their Application, Giardini Naxos, ITALY*, p. 143, 2007.

[28] P. Bricault, R. Baartman, M. Dombsky, A. Hurst, C. Mark, G. Stan-ford, and P. Schmor, "TRIUMF-ISAC target station and mass separa-tor commissioning," *Nuclear Physics A*, vol. 701, no. 14, pp. 49 – 53, 2002. 5th International Conference on Radioactive Nuclear Beams.

[29] P. G. Bricault and H. Weick, "Use of the chalk river mass separator for ISAC," *TRIUMF Internal Design Note, TRI-DN-97-16*, 1997.

[30] F. Ames, R. Baartman, P. Bricault, K. Jayamanna, M. McDonald, M. Olivo, P. Schmor, D. H. L. Yuan, and T. Lamy, "Charge state breeding of radioactive ions with an electron cyclotron resonance ion source at triumf," *Review of Scientific Instruments*, vol. 77, no. 3, 2006.

[31] F. Ames, R. Baartman, P. Bricault, and K. Jayamanna, "Charge state breeding of radioactive isotopes for isac," *Hyperfine interactions*, vol. 225, no. 1-3, pp. 63–67, 2014.

[32] R. Laxdal and M. Marchetto, "The isac post-accelerator," *Hyperfine Interactions*, vol. 225, no. 1-3, pp. 79–97, 2014.

[33] R. Poirier, R. Baartman, P. Bricault, K. Fong, S. Koscielniak, R. Lax-dal, A. Mitra, L. Root, G. Stanford, and D. Pearce, "CW performance

of the TRIUMF 8 meter long RFQ for exotic ions," *Linear Accelerator Conference, Monterey, California, USA*, p. 1023, 2000.

[34] I. Kapchinskii and V. Teplyakov, "A linear ion accelerator with spatially uniform hard focusing," *Prib. Tekh. Eksp.*, vol. 1970, no. SLAC-TRANS-0099, pp. 19–22, 1969.

[35] S. R. Koscielniak, R. Laxdal, R. Lee, and L. Root, "Beam dynamics studies on the ISAC RFQ at TRIUMF," *Particle Accelerator Conference, Vancouver, British Columbia, CANADA*, vol. 1, pp. 1102–1104, 1997.

[36] R. Laxdal, G. Dutto, K. Fong, G. Mackenzie, M. Pasini, R. Poirier, and R. Ruegg, "Beam commissioning and first operation of the ISAC DTL at TRIUMF," *Particle Accelerator Conference, Chicago, Illinois, USA*, vol. 5, pp. 3942–3944, 2001.

[37] R. Laxdal, "Commissioning and early experiments with ISAC-II," *Particle Accelerator Conference, Albuquerque, New Mexico, USA*, pp. 2593–2597, 2007.

[38] C. N. Davids and D. Peterson, "A compact high-resolution isobar separator for the CARIBU project," *Nuclear Instruments and Methods in Physics Research Section B: Beam Interactions with Materials and Atoms*, vol. 266, no. 1920, pp. 4449 – 4453, 2008. Proceedings of the {XVth} International Conference on Electromagnetic Isotope Separators and Techniques Related to their Applications.

[39] M. Dworschak, G. Audi, K. Blaum, P. Delahaye, S. George, U. Hager, F. Herfurth, A. Herlert, A. Kellerbauer, H.-J. Kluge, *et al.*, "Restoration of the n= 82 shell gap from direct mass measurements of sn 132, 134," *Physical review letters*, vol. 100, no. 7, p. 072501, 2008.

[40] K. Jones, A. Adekola, D. Bardayan, J. Blackmon, K. Chae, K. Chipps, J. Cizewski, L. Erikson, C. Harlin, R. Hatarik, *et al.*, "The magic nature of 132sn explored through the single-particle states of 133sn," *Nature*, vol. 465, pp. 454–457, 2010.

Bibliography

[41] K. Makino and M. Berz, "COSY INFINITY version 9," *Nuclear Instruments and Methods in Physics Research Section A: Accelerators, Spectrometers, Detectors and Associated Equipment*, vol. 558, no. 1, pp. 346 – 350, 2006. Proceedings of the 8th International Computational Accelerator Physics ConferenceICAP 20048th International Computational Accelerator Physics Conference.

[42] J. T. Tanabe, "Iron dominated electromagnets: Design, fabrication, assembly and measurements," *IRON DOMINATED ELECTROMAGNETS: DESIGN, FABRICATION, ASSEMBLY AND MEASUREMENTS. Edited by TANABE JACK T. Published by World Scientific Press, 2005. ISBN# 9789812567642*, 2005.

[43] J. F. Ostiguy, "Longitudinal profile and effective length of a conventional dipole magnet," *Particle Accelerator Conference, Washington, D.C., USA*, pp. 2901–2903 vol.4, 1993.

[44] W. Rogowski, "Die elektrische festigkeit am rande des plattenkondensators," *Archiv für Elektrotechnik*, vol. 12, no. 1, pp. 1–15, 1923.

[45] P. Sarma, A. D. Gupta, C. Nandi, S. Chattopadhyay, and G. Pal, "Unconventional purcell filter in superferric magnets in the facility for antiproton and ion research," *Nuclear Instruments and Methods in Physics Research Section A: Accelerators, Spectrometers, Detectors and Associated Equipment*, vol. 729, pp. 718 – 724, 2013.

[46] T. Kurtukian-Nieto, R. Baartman, B. Blank, T. Chiron, C. Davids, F. Delalee, M. Duval, S. E. Abbeir, A. Fournier, D. Lunney, F. Mot, L. Serani, M.-H. Stodel, F. Varenne, and H. Weick, "SPIRAL2/DESIR high resolution mass separator," *Nuclear Instruments and Methods in Physics Research Section B: Beam Interactions with Materials and Atoms*, vol. 317, Part B, pp. 284 – 289, 2013. {XVIth} International Conference on ElectroMagnetic Isotope Separators and Techniques Related to their Applications, December 27, 2012 at Matsue, Japan.

Part I

Appendices

Appendix A

Hill's Equation

The transverse motion of the particles in a periodic beam transport channel (beam line) is governed by Hill's equation[26]:

$$\frac{d^2x(s)}{ds^2} + k(s)\,x(s) = 0 \qquad (A.1)$$

where for a periodic transport system $k(s)$ is a periodic function of the variable s that is the path length along the reference trajectory. The $k(s)$ function describes the focusing strength along the transport channel.

The general solution of equation A.1 is:

$$x(s) = \sqrt{\varepsilon_0\,\widetilde{\beta}(s)}\,\cos(\phi(s) + \phi_0) \qquad (A.2)$$

From equation A.2 we calculate the first derivative $\frac{d}{ds}$ (indicated with $'$):

$$x'(s) = \frac{1}{2}\frac{\varepsilon_0}{\sqrt{\varepsilon_0\,\widetilde{\beta}(s)}}\,\widetilde{\beta}'(s)\,cos(\phi(s)+\phi_0) - \sqrt{\varepsilon_0\,\widetilde{\beta}(s)}\,sin(\phi(s)+\phi_0)\,\phi'(s) \quad (A.3)$$

Equation A.3 can be written as:

$$x'(s) = -\widetilde{\alpha}(s)\sqrt{\frac{\varepsilon_0}{\widetilde{\beta}(s)}}\,cos(\phi(s) + \phi_0) - \sqrt{\frac{\varepsilon_0}{\widetilde{\beta}(s)}}\,sin(\phi(s) + \phi_0) \qquad (A.4)$$

---

[26]see chapter 7 of [10], or chapter 5 of [11]

with:

$$\widetilde{\alpha}(s) = -\frac{1}{2}\widetilde{\beta}'(s) \tag{A.5}$$

and

$$\phi'(s) = \frac{1}{\widetilde{\beta}(s)} \tag{A.6}$$

From equation A.2 and A.4 we derive the following second order terms:

$$x^2(s) = \varepsilon_0 \, \widetilde{\beta}(s) \, cos^2\mu(s) \tag{A.7}$$

where $\mu(s) = \phi(s) + \phi_0$.

$$x'^2(s) = \frac{\widetilde{\alpha}^2(s)\,\varepsilon_0}{\widetilde{\beta}(s)}\, cos^2\mu(s) + \frac{\varepsilon_0}{\widetilde{\beta}(s)}\, sin^2\mu(s) + \frac{2\,\widetilde{\alpha}\,\varepsilon_0}{\widetilde{\beta}(s)}\, cos\mu(s)\, sin\mu(s) \tag{A.8}$$

and

$$x(s)\,x'(s) = -\widetilde{\alpha}(s)\,\varepsilon_0\, cos^2\mu(s) - \varepsilon_0\, cos\mu(s)\, sin\mu(s) \tag{A.9}$$

Equation A.8 can be rearranged as follow:

$$
\begin{aligned}
x'^2(s) &= \frac{\widetilde{\alpha}^2(s)\,\varepsilon_0}{\widetilde{\beta}(s)}\, cos^2\mu(s) + \frac{\varepsilon_0}{\widetilde{\beta}(s)} - \frac{\varepsilon_0}{\widetilde{\beta}(s)}\, cos^2\mu(s) + \frac{2\,\widetilde{\alpha}\,\varepsilon_0}{\widetilde{\beta}(s)}\, cos\mu(s)\, sin\mu(s) = \\
&= \frac{2\,\widetilde{\alpha}^2(s)\,\varepsilon_0}{\widetilde{\beta}(s)}\, cos^2\mu(s) - \frac{\widetilde{\alpha}^2(s)\,\varepsilon_0}{\widetilde{\beta}(s)}\, cos^2\mu(s) + \frac{\varepsilon_0}{\widetilde{\beta}(s)} - \frac{\varepsilon_0}{\widetilde{\beta}(s)}\, cos^2\mu(s) + \\
&+ \frac{2\,\widetilde{\alpha}\,\varepsilon_0}{\widetilde{\beta}(s)}\, cos\mu(s)\, sin\mu(s) = \\
&= \frac{2\,\widetilde{\alpha}(s)}{\widetilde{\beta}(s)}\, (\widetilde{\alpha}(s)\,\varepsilon_0\, cos^2\mu(s) + \varepsilon_0\, cos\mu(s)\, sin\mu(s)) + \\
&- \frac{\varepsilon_0}{\widetilde{\beta}(s)}\, cos^2\mu(s)\, (\widetilde{\alpha}^2(s) + 1) + \frac{\varepsilon_0}{\widetilde{\beta}(s)} =
\end{aligned}
$$

$$
\begin{aligned}
&= -\frac{2\,\widetilde{\alpha}(s)}{\widetilde{\beta}(s)}\,x(s)\,x'(s) - \frac{\varepsilon_0\,\widetilde{\beta}(s)}{\widetilde{\beta}(s)}\,cos^2\mu(s)\,\frac{\widetilde{\alpha}^2(s)+1}{\widetilde{\beta}(s)} + \frac{\varepsilon_0}{\widetilde{\beta}(s)} = \\
&= -\frac{2\,\widetilde{\alpha}(s)}{\widetilde{\beta}(s)}\,x(s)\,x'(s) - \frac{x^2(s)}{\widetilde{\beta}(s)}\widetilde{\gamma}(s) + \frac{\varepsilon_0}{\widetilde{\beta}(s)} \quad\quad\quad\quad\quad (\text{A.10})
\end{aligned}
$$

where:

$$
\widetilde{\gamma}(s) = \frac{\widetilde{\alpha}^2(s)+1}{\widetilde{\beta}(s)} \quad\quad\quad\quad\quad (\text{A.11})
$$

From equation A.10 we then have:

$$
\widetilde{\gamma}(s)\,x^2(s) + 2\,\widetilde{\alpha}(s)\,x(s)\,x'(s) + \widetilde{\beta}(s)\,x'^2(s) = \varepsilon_0 \quad\quad\quad (\text{A.12})
$$

Since $\widetilde{\gamma}(s)\,\widetilde{\beta}(s) - \widetilde{\alpha}^2(s) = 1$, equation A.12 represents an ellipse in the Cartesian plane centered in the origin with area $\pi\varepsilon_0$ (see figure A.1).
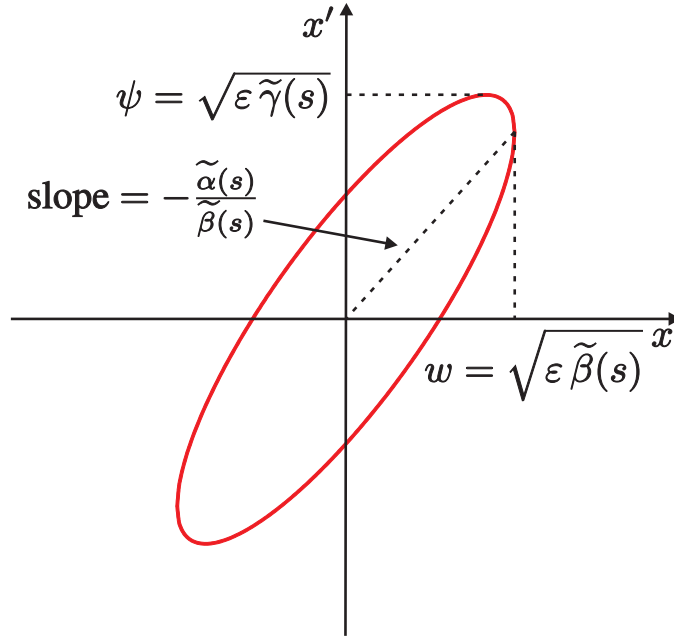

Figure A.1: Graphic representation of equation A.12 in the Cartesian plane.

Appendix A. Hill's Equation

The function $\widetilde{\alpha}(s)$, $\widetilde{\beta}(s)$ and $\widetilde{\gamma}(s)$ are called the Courant-Snyder parameters, while ε_0 and ϕ_0 are constants determined by the initial conditions. When $\widetilde{\alpha}(0)$, $\widetilde{\beta}(0)$ and $\widetilde{\gamma}(0)$ coincide with the input values of a transport channel (match condition for the particle), then the Courant-Snyder parameters have the same periodicity as the function $k(s)$.

For a given ε_0, the position of a particle in phase space at a location s lies on an ellipse described by equation A.12. When $\widetilde{\alpha}(s)$, $\widetilde{\beta}(s)$ and $\widetilde{\gamma}(s)$ have the same periodicity as $k(s)$, a particle lies on an identical ellipse at every period but in general on a different position of coordinates $(x(s), x'(s))$. The angular difference between two different positions on identical ellipses separated by one period is $\phi(s)$ and it is called the phase advance.

Appendix B

Gaussian Beam Distribution

Let's consider a particle beam that have a bivariate[27] Gaussian distribution in (x,x') with standard deviation respectively σ_1 and σ_2, the probability density function of such distribution is:

$$p(x,x') = \frac{1}{2\,\pi\,\sigma_1\,\sigma_2\sqrt{1-\rho_{x,x'}^2}}e^{-\frac{(x-\mu_1)^2}{2\,(1-\rho_{x,x'}^2)\,\sigma_1^2}+\frac{2\,\rho_{x,x'}\,(x-\mu_1)\,(x'-\mu_2)}{2\,(1-\rho_{x,x'}^2)\,\sigma_1\,\sigma_2}-\frac{(x'-\mu_2)^2}{2\,(1-\rho_{x,x'}^2)\,\sigma_2^2}}$$

(B.1)

where

$$\rho_{x,x'} = corr(x,x')$$

(B.2)

If we assumed that the distribution is represented by an upright ellipse centered in the origin, then the distribution is uncorrelated, $\rho_{x,x'} = 0$, and $\mu_1 = \mu_2 = 0$. Equation B.2 can then be simplified in:

$$p(x,x') = \frac{1}{2\,\pi\,\sigma_1\,\sigma_2}e^{-\frac{x^2}{2\,\sigma_1^2}-\frac{x'^2}{2\,\sigma_2^2}}$$

(B.3)

If we take:

$$\sigma_1 = \sqrt{\varepsilon\,\widetilde{\beta}(s)}$$

(B.4)

and

$$\sigma_2 = \sqrt{\varepsilon\,\widetilde{\gamma}(s)}$$

(B.5)

---

[27]http://mathworld.wolfram.com/BivariateNormalDistribution.html

than we have the distribution of a 1σ emittance as represented by the blue ellipse in figure B.1 with no correlation between x and x'.
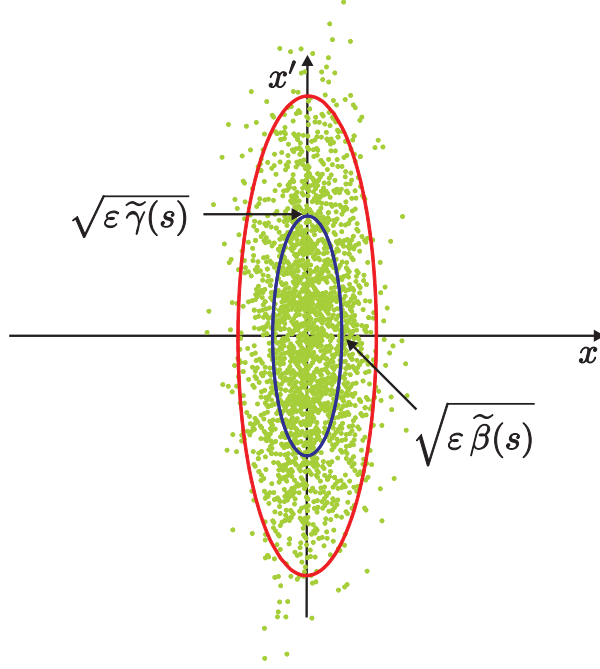

Figure B.1: Upright emittances: 1σ (blue) and 4σ (red).

From equation B.3 we can calculate the relative number of particle within 1σ emittance as follow:

$$P(x, x') = \frac{1}{2\,\pi\,\sigma_1\,\sigma_2} \int\limits_{-\sigma_1}^{+\sigma_1} \int\limits_{-\sigma_2}^{+\sigma_2} e^{-\frac{\sigma_2^2\,x^2 + \sigma_1^2\,x'^2}{2\,\sigma_1^2\,\sigma_2^2}} \; dx\,dx' \tag{B.6}$$

Changing variables:

$$x = \sigma_1\,a \tag{B.7}$$

and

$$x' = \sigma_2\,b \tag{B.8}$$

136

Equation B.6 become with $dx = \sigma_1\, da$ and $dx' = \sigma_2\, db$:

$$
\begin{aligned}
P(a,b) &= \frac{1}{2\,\pi\,\sigma_1\,\sigma_2} \int\limits_{-1}^{+1}\int\limits_{-1}^{+1} e^{-\frac{\sigma_2^2\,\sigma_1^2\,a^2 + \sigma_1^2\,\sigma_1^2\,b^2}{2\,\sigma_1^2\,\sigma_2^2}} \, \sigma_1\,\sigma_1\, da\, db = \\
&= \frac{1}{2\,\pi} \int\limits_{-1}^{+1}\int\limits_{-1}^{+1} e^{-\frac{a^2+b^2}{2}} \, da\, db
\end{aligned}
\tag{B.9}
$$

Moving to cylindrical coordinates:

$$
a = r\,cos(\theta)
\tag{B.10}
$$

and

$$
b = r\,sin(\theta)
\tag{B.11}
$$

Equation B.6 become with $da\, db = r\, dr\, d\theta$:

$$
\begin{aligned}
P(r,\theta) &= \frac{1}{2\,\pi} \int\limits_{0}^{2\,\pi}\int\limits_{0}^{+1} e^{-\frac{r^2\,cos^2(\theta) + r^2\,sin^2(\theta)}{2}} \, r\, dr\, d\theta = \\
&= \frac{1}{2\,\pi} \int\limits_{0}^{2\,\pi}\int\limits_{0}^{+1} r\, e^{-\frac{r^2}{2}} \, dr\, d\theta = \\
&= \left[\frac{1}{2\,\pi} \int\limits_{0}^{+1} r\, e^{-\frac{r^2}{2}} \, dr \right]_{0}^{2\pi} = \\
&= \left[-e^{\frac{-r^2}{2}} \right]_{0}^{1} = \left[1 - e^{-\frac{1}{2}} \right] = 0.39
\end{aligned}
\tag{B.12}
$$

So if a beam has a Gaussian distribution in both x and x', then 39% of the beam is contained within the 1σ emittance. If we consider 2σ in both

axes, then equation B.12 yields that 86% of the beam is contained within the 4σ emittance (see red ellipse in figure B.1).